UNIVERSITA' DEGLI STUDI DI PADOVA

Dipartimento di Ingegneria Industriale DII

Dipartimento di Tecnica e Gestione dei Sistemi Industriali - DTG

Corso di Laurea Magistrale in Ingegneria Meccanica

Structural behavior of electrical post-insulators for the MITICA experiment: numerical models and experimental tests

Relatore: Prof. Chitarin Giuseppe

Correlatore: Dr. Sylvestre Denizeau

Spolaore Bruno Carl Angelo 2053117

Anno Accademico *2022/2023*

CONSORZIO RFX

Ricerca Formazione Innovazione

Table of Contents

Abstract

The objective of this thesis is the experimental validation of particular structural components of the MITICA Beam Source prototype, made of Polyetheretherketone (PEEK), an engineering thermoplastic with high mechanical and electrical insulation properties. The components are named "post-insulators" due to their double-function of mechanical support and of electrical insulator and are subjected to high mechanical strengths since they sustain the whole weight of the cantilevered structure of the MITICA Mock-Up Beam Source, as properly described later.

The thesis has been carried out at “Consorzio RFX” during the months between March and December 2023 under the supervision of Prof. Giuseppe Chitarin and Dr. Sylvestre Denizeau.

In a first phase, the stress distribution and deformation of the PEEK post-insulators is simulated using two FEM models, so as to evaluate the behavior during operation and to support the interpretation of the results to be obtained during subsequent tests. A first model used accurate geometry, including also screws, helicoils and bolts connections used to fasten the PEEK insulator to the stainless-steel flanges. The second model was a simplified version of the same post-insulators model, where connections by screws, helicoils and bolts were replaced with bonded contact type connection.

Experimental tests were then carried out on 4 post-insulator samples, using a specific set-up, so as to measure the force-deformation characteristic of the insulators, while subjected to a pre-determined tensile force and bending moment combination.

The results indicated that, the stiffness calculated by either numerical simulation procedure was overestimated with respect to the experimental data. Such discrepancy has consequences in terms of total deformations, equivalent stress and natural frequencies of the MITICA Mock-Up Beam Source. The differences have been quantified by calibrating the numerical models of the tensile test with the experimental results.

Lastly, an explanation of this discrepancy is given by making an accurate sub model of the M14 screw, helicoil and PEEK bulk material. This model shows how the replacing real-case screw-helicoil connections with standard bonded connections causes an increased stiffness of the model compared to the real-case scenario.

Riassunto esteso in lingua italiana

La seguente tesi magistrale ha come scopo la verifica sperimentale di un componente strutturale particolare che appartiene al prototipo “MITICA Mock-Up”. Questo componente è fabbricato in PEEK, un materiale termoplastico ad elevate proprietà meccaniche, e viene denominato “isolatore” poiché possiede, oltre a un ruolo meccanico-strutturale, il compito di fornire adeguato isolamento elettrico. La sua verifica è stata eseguita tramite l’utilizzo di una macchina a trazione e di un’apposita attrezzatura che, combinati, permettono di riprodurre i carichi di trazione, taglio e momento flettente previsti sul componente. La verifica sperimentale si è svolta su 4 isolatori di forma cilindrica, di circa 13 cm di diametro e 28 cm di altezza.

Il “MITICA Mock-Up” è stato progettato per permettere la validazione sperimentale dell'innovativo sistema di isolamento elettrico del “MITICA Beam Source”. Per chiarezza, MITICA è l’esperimento che ha come obiettivo la progettazione dell’iniettore di particelle neutre da ioni negativi, uno dei sistemi di riscaldamento del plasma che verrà adoperato al reattore a fusione sperimentale da confinamento magnetico denominato “ITER”, attualmente in costruzione nel sud della Francia.

Il riscaldamento del plasma da parte dell’iniettore di particelle neutre da ioni negativi consiste nel trasferimento dell’energia cinetica posseduta dalle particelle neutre, dirette verso l’interno del reattore, al plasma che è intrappolato da una gabbia di intensi campi magnetici per prevenirne il contatto diretto con le pareti interne del reattore. In condizioni estreme di densità, temperatura e tempo di confinamento si favorisce la generazione di reazioni a termofusione nucleare. Quindi la conversione di energia cinetica delle particelle neutre in energia termica del plasma presente all’interno del reattore aiuta il raggiungimento delle condizioni necessarie per l’avvio di una reazione a fusione nucleare.

Per consentire un riscaldamento significativo, si cerca il raggiungimento di elevate energie cinetiche di particelle neutre del fascio dell’iniettore (NBI – Neutral Beam Injector). Per ottenerle, si generano atomi carichi elettricamente che vengono poi accelerati tramite una differenza di potenziale di 1 MV che vengono poi neutralizzati prima di essere diretti all’interno del reattore. La neutralizzazione è necessaria poiché altrimenti non sarebbe possibile attraversare la gabbia di intensi campi magnetici che intrappola il plasma. Nel progetto originale, l’acceleratore è costituito da 5 stadi a 200 kV di differenza l’uno dall’altro, separati da 12 isolatori di Alumina (materiale ceramico) per stadio (tranne l’ultimo che ne ha 8) e il tutto è racchiuso in una camera a vuoto per consentire l’isolamento elettrico della struttura.

Di fatto però, il nuovo sistema di isolamento elettrico ha bisogno di verifica sperimentale in quanto in altri progetti simili l’isolamento elettrico è previsto tramite l’uso di gas SF_6 ad alta pressione. Però, siccome tale gas interagisce con i neutroni prodotti all’interno del reattore, nel caso di MITICA si è preferito l’uso di isolatori tra le griglie di accelerazione e del vuoto attorno al resto della struttura. Ingente lavoro di ricerca e sviluppo è stato fatto per gli isolatori in Alumina in modo da poter garantire il soddisfacimento di requisiti meccanici ed elettrici del componente allo stesso tempo. Tuttavia, rimane necessaria la validazione sperimentale dell’isolamento elettrico a vuoto.

Per questo motivo è stato progettato e sviluppato il “MITICA Mock-Up” e siccome l’interesse di questo prototipo riguarda esclusivamente la verifica del’isolamento a vuoto, la geometria e i materiali del prototipo sono stati modificati per contenere costi e complessità di realizzazione prestando attenzione a non influenzare significativamente l’esito dei futuri test elettrici. Di fatto, la geometria è stata semplificata tenendo conto solo degli elementi critici per l’isolamento elettrico e i materiali sono stati modificati, adoperandone di più economici rispetto al progetto originale di “MITICA Beam Source”.

Nel caso dell’isolatore, al posto del materiale ceramico Alumina, è stato adoperato il PEEK, un materiale termoplastico ad alte prestazioni meccaniche e di isolamento elettrico. Questo componente è soggetto a grossi carichi a causa del peso proprio, di circa 4 tonnellate, della struttura a sbalzo del “MITICA Mock-Up”. Per questo è stato necessario verificare l’integrità dei componenti maggiormente sollecitati della struttura: gli isolatori.

Tramite la simulazione numerica del “MITICA Mock-Up” è stato possibile definire i requisiti di sforzi di tensione, taglio e momenti minimi che ciascun isolatore deve poter sostenere in condizioni nominali di esercizio. I carichi dell’isolatore maggiormente sollecitato tra quelli del “MITICA Mock-Up” sono riprodotti sull’isolatore in PEEK applicando un fattore di sicurezza 2 nel carico minimo che deve essere sostenuto. Le condizioni più severe delle prove di trazione garantiscono con buon margine di sicurezza per garantire la loro integrità.

Il set-up sperimentale utilizzato per l'isolatore in PEEK è lo stesso impiegato per l'isolatore in Alumina, anche se le condizioni di carico diventano dominanti in taglio piuttosto che in trazione. Questa differenza di carico comporta che vi è il rischio di rottura dell’isolatore in PEEK durante la prova a trazione prima che si raggiunga i valori obiettivo di taglio e/o momento del componente. Infatti, oltre ai carichi previsti di taglio e momento, agisce in contemporanea una forza di trazione alcune volte superiore rispetto al valore obiettivo, rappresentando una condizione di carico ancora più severa di quella prevista. Nel caso l’isolatore dovesse rompersi prima di raggiungere tali valori obiettivo, sarebbe stata necessaria la progettazione di un nuovo set-up sperimentale.

Ciò nonostante, tutti e 4 gli isolatori in PEEK hanno superato con ampio margine i requisiti meccanici imposti. Il valore obiettivo di 48 kN della macchina a trazione è stato superato, raggiungendo almeno un valore di 75.5 kN con un fattore di sicurezza 2, oltre a un ulteriore fattore di margine di rottura di 2.08. Inoltre, è stato poi anche definito il valore di carico della macchina a trazione oltre il quale il comportamento del componente in PEEK non può più essere definito elastico. Tale valore è stato determinato tenendo conto un errore del 2% ed è pari a 24.7 kN.

Invece, l’aspetto numerico della tesi riguarda principalmente la riproduzione numerica della prova a trazione tramite due modelli numerici ANSYS. Il primo utilizza una geometria che tiene conto di viti ed helicoil M14 tra isolatore e flange, nonché di viti e bulloni M10 tra flange e staffe di collegamento alla macchina di trazione. Per tutti questi componenti la filettatura è stata trascurata, adoperando invece una connessione di tipo “bonded” tra le superfici che ne impedisce lo scorrimento. Il secondo, invece, adopera una geometria semplificata che non

tiene conto di elementi connettivi quali viti, helicoil e bulloni e che denota un serio vantaggio in termini di peso computazionale a causa del ridotto numero di elementi.

Tuttavia, il confronto tra i risultati sperimentali e quelli numerici in termini di forza-spostamento fa emergere la maggiore rigidità dei modelli numerici rispetto ai risultati sperimentali e tale discrepanza potrebbe generare un errore non conservativo in termini di deformazione e frequenza naturale dominante del MITICA Mock-Up". Infatti, per carichi più elevati si registrano deformazioni minori la cui omissione potrebbe non garantire il soddisfacimento dei requisiti di massima deformazione dell'intera struttura. Inoltre, una rigidità inferiore della struttura influenza direttamente le sue frequenze naturali, diminuendone tendenzialmente il valore e rischiando di avvicinare significativamente le frequenze naturali di "MITICA Mock-Up" alle frequenze tipiche dell'attività sismica presente a Padova, aumentando l'efficacia di trasmissione dei energia a causa del fenomeno della "risonanza" e rappresentando quindi un rischio per la sua integrità.

Pertanto, per valutare le conseguenze della minore rigidità strutturale dell'isolatore in PEEK, è stato definito un materiale PEEK equivalente che meglio segue i valori sperimentali ottenuti. Tale materiale è stato poi utilizzato anche nell'analisi statica lineare e modale dell'intera struttura di "MITICA Mock-Up", senza però comportare differenze significative in termini di deformazione (0.5 mm) e frequenze naturali (0.9 Hz) rispetto ai valori determinati precedentemente. Dunque, è stato possibile procedere con l'installazione del prototipo che è attualmente già assemblato al Consorzio RFX di Padova, pronto per i test elettrici.

Inoltre, è stato indagato tramite analisi statica lineare e tramite "Explicit Dynamics" la modalità di rottura del componente in PEEK. Dall'ispezione visuale degli isolatori fratturati sembrerebbe che la frattura si sia originata dal filetto più stressato degli helicoil più sollecitati dell'isolatore. Questa supposizione ha ritrovato conferme nel modello tridimensionale della vite e dell'helicoil e nel medesimo modello bidimensionale in cui è possibile confermare anche la direzione di propagazione della rottura.

Parallelamente, invece, si ha indagato sulla causa che ha generato la discrepanza di rigidità tra i dati numerici e quelli sperimentali. È stato sviluppato un sotto modello accurato di connessione tra vite ed helicoil M14. Tale sotto modello mette a confronto i risultati numerici che si otterrebbero modellando anche le filettature della vite ed del helicoil a contatto tra di loro (coefficiente di attrito 0.2) con i risultati in cui le filettature vengono rimpiazzate con superfici lisce e contatti di tipo "bonded" (nessuno scorrimento). Il confronto fa emergere che il modello con filettature è meno rigido del 31.2% rispetto al modello senza filettature. Questo risultato spiegherebbe come mai ci sia una discrepanza di circa un terzo in termini di rigidità tra i risultati di forza-spostamento numerici e sperimentali.

Tuttavia, la modellazione che tiene conto delle filettature è dispendiosa a livello computazionale e non conviene utilizzarlo nel modello numerico del "MITICA Mock-Up". Per questo motivo si è cercato un modo per meglio calibrare il modello senza filettatura con i risultati sperimentali. Così stato definito un ulteriore materiale equivalente (AISI 304 L fittizio) da utilizzare per il componente helicoil, interposto tra la vite e l'isolatore. Questo materiale è stato adoperato nella simulazione numerica realistica che riproduce la prova a trazione dell'isolatore in PEEK nella speranza di ritrovare risultati più simili a quelli sperimentali. Con questo metodo è stata ottenuta

una diminuzione di rigidità del modello numerico del 4.2%, di gran lunga inferiore rispetto a quello atteso di circa il 31.2%. Pertanto, vi è ancora margine di miglioramento per poter meglio includere la discrepanza di rigidità osservata tra il sotto modello vite-helicoil M14 con filettature e lo stesso sotto modello senza filettature all'interno di modelli numerici più complessi.

Infine, la seguente tesi ha posto la base per due sviluppi futuri principali. Innanzitutto, l'applicazione del sotto modello sulla connessione tra vite ed helicoil M14 può essere estesa anche al materiale ceramico (Alumina), di interesse per il progetto "MITICA Beam Source". In aggiunta, è stato cercato un modo per ottenere una modellazione semplice ed efficace del componente "helicoil", ampiamente utilizzato in diversi settori ingegneristici, ma la cui modellazione numerica è un tema scarsamente trattato in letteratura.

1. Introduction to nuclear fusion

1.1. Sustainable development

This chapter is the first of a two-part introduction. This specific section aims to provide an overview of the state-of-the-art of the energy sector and some of its future development, strictly related to the concept of “Sustainable Development”.

In the last decade, the public concern about the climate-changing effects of energy consumption has substantially increased and governments worldwide are struggling to implement policies to achieve the decarbonisation of the whole energy sector by 2050. [1–4] According to an IPSOS survey of April 2020, climate change is perceived by the population in the long term as a crisis of the same level as COVID-19. [5] As a matter of fact, energy-consuming services necessary for everyday life, such as transportation, lighting, heating and cooling, need to be strictly related to the concept of “Sustainable Development”. It is defined as the type of development that “fulfils present needs without undermining the capability of future generations to fulfil their own needs”. [6] It is subdivided into three pillars of equal importance: [6,7]

- *Economic sustainability*, such as financial growth and stability, rate of inflation in a market economy, cost savings, long range planning;
- *Social sustainability*, of which social equity and stability, rate of employment, level of education, democracy, quality of life are some examples;
- *Environmental sustainability*, related to resource management, to the threshold values for clean water, soil, air and their update due to increased level of knowledge or resource management.

In other words, the evolution of the energy sector of a country is directly related to these three pillars. In fact, the quality of life in different regions of the world can be directly correlated with the per capita use of energy. [8] As soon as high-power density machines became available, the amount of average energy available for a single person increased. Consequently, the world population grew, raising the average demand of yearly energy required as show in Figure 1-1.

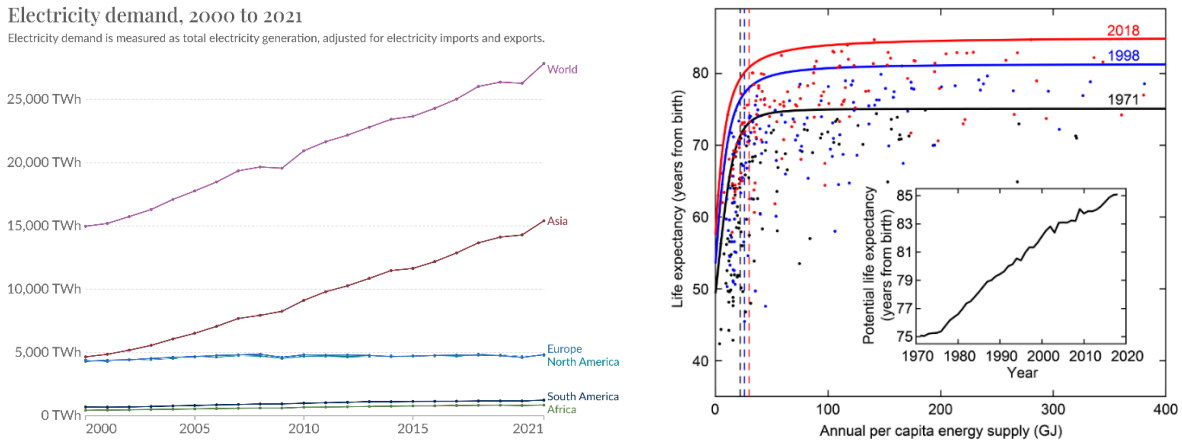

Figure 1-1: yearly worldwide electricity demand (left) [9] and longer life expectancy with increasing trend of annual energy supply (right) [10].

Therefore, energy services are fundamental to social and economic sustainability, however, energy resources and technologies that are used today, notably the ones present with the highest shares (Figure 1-2), jeopardise environmental sustainability. [11]

The concentration of Carbon Dioxide CO_2 has increased greatly in the last decades, leading to evident climate change effects, uncontrolled global warming and unprecedented weather events. In May 2023, the CO_2 concentration reached a new peak value of 424 ppm. [12,13] The carbon dioxide concentration was at about 400 ppm only in 2015 and at about 370 ppm in the early 2000s as show in Figure 1-2.

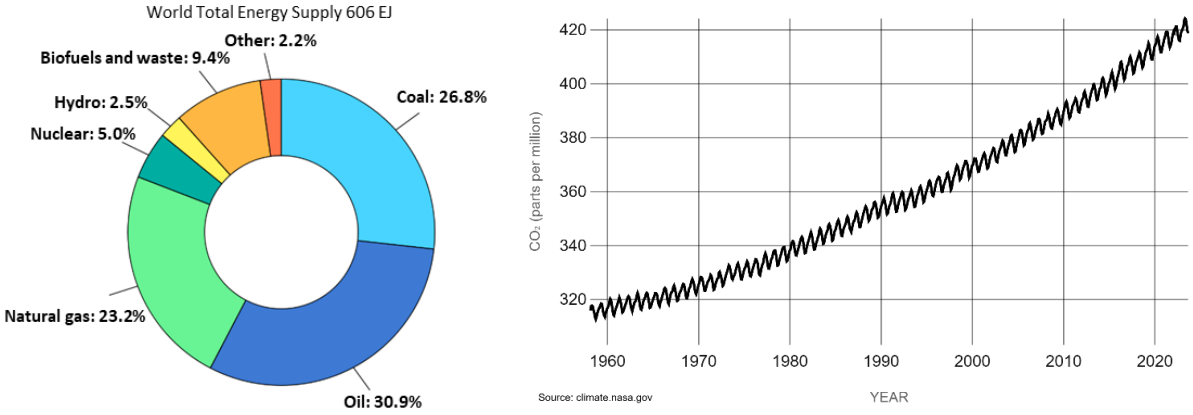

Figure 1-2: Global share of total energy supply by source of 2019 (left) [14] and worldwide CO2 concentration in ppm from 1960 up to 2022 (right) [13].

In the short term, there are many other energy sources that can tackle the “Sustainable Development” crisis: solar photovoltaic, wind energy, nuclear fission and biofuel technologies. However all these forms of energy lack at least one of the following: favourable energy density, steady energy output (weather dependency), minimal amount of dangerous wastes or sufficient public acceptance. [8]

In the long term, nuclear fusion is one of the most effective tools to solve the issue of “Sustainable development”, since it allows the carbon-free generation of electricity based on the controlled thermonuclear fusion reactions of hydrogen isotopes. “When a reality, fusion will be a source of low carbon energy and can contribute to decarbonization and diversification of energy generation in the long term to meet the mitigation of greenhouse gas emissions and limit increases of global mean surface temperature even as electricity needs worldwide continue to grow”. [2]

However, this technology, besides being still at research stage, shows several limitations:

- it is based on complex systems requiring innovative not-yet-available technologies and materials;
- it still produces a small amount of radioactive waste, because the reactor material is activated by neutron fluxes during operation;

- the most accessible fusion reaction requires Tritium, a radioactive element of poor abundance due to its half-life of roughly 12.6 years,
- the reactor structure is activated by neutron fluxes during the life cycle of the reactors;
- it requires a highly trained workforce.

However, despite of all these challenging aspects, nuclear fusion technology also shows great potential and a valuable set of advantages: [8]

- the fuel, Deuterium, is plentiful and easily accessible to all countries on earth with no risk of conflicts as it has been happening with fossil fuels;
- the reactor is inherently safe: the consequences of an accident are much less severe than those of a nuclear fission power plant since the fusion reactions are not spontaneous and are not part of a chain reaction;
- the radioactive waste produced is categorised as “Low Level Waste” (LLW), which can be recycled or prepared for near surface disposal according to the “IEAE Standards Classification of Radioactive Waste”. [15]
- the energy produced by 1 g of Deuterium-Tritium fuel is four times the one produced by 1 g of Uranium^{235} and 10^7 times the one produced by 1 g of coal [11,16] (see
- Table 1);
- the high complexity is tackled by international collaboration and huge experience in neutron moderation and neutron damaged materials obtained thanks to fission reactors and research.

The great potential of nuclear fusion based powerplants and the interest for fusion technology is reflected also by the recent significant increase of fusion activities and investments in the private sector: 43 private companies worldwide have a value of $6,2 billion (~5,9 billion Euros).[2]

Type of Fuel	Energy released [J/g]	Energy Type
Coil	2.93×10^4	Chemical
Oil	4.62×10^4	Chemical
Natural gas	5.36×10^4	Chemical
Gasoline	4.64×10^4	Chemical
Diesel	4.56×10^4	Chemical
Uranium U235	8.21×10^10	Nuclear
Deuterium-Tritium	3.37×10^11	Nuclear

Table 1: energy produced by 1 g of product of different energy sources.

1.2. Nuclear fusion reactions

Despite both being nuclear reactions, nuclear fission and fusion are fundamentally two different phenomena. Fission stands for the separation of a heavy unstable nucleus into two smaller nuclei, whereas fusion stands for the fusion of two lighter nuclei into one heavier and more stable nucleus. More precisely, under favourable conditions, two nuclei close enough to each other can spontaneously turn into a heavier and more stable one. In this state they then require less binding energy to stay cohesive than the initial elements of the reaction. This excess of binding energy is then released as kinetic energy. The quantity of energy released "E" is derived from the conversion of mass "m" into energy according to Einstein's relation:

$$E = m \cdot c^2$$

Where "c" represents the speed of light in vacuum. In fact, in these types of reactions, the weight of the product is always less than the sum of the reactants' masses since the total binding energy is less in the product configuration. Nevertheless, since the total relativistic energy is conserved, no energy is created or destroyed, but simply transformed into another form. Thus, the energy of a reaction "Q" is defined as:

$$Q = \Delta m \cdot c^2$$

with "Δm" the mass difference between the nuclei that collide together and the product particles of the reaction.

$$\Delta m = m_{reactants} - m_{products} \qquad m_{reactants} > m_{products}$$

As previously mentioned, the most easily accessible controlled thermonuclear fusion reaction is the fusion of Deuterium D or ${}^{2}_{1}H$ and Tritium T or ${}^{3}_{1}H$:

$${}^{2}_{1}H + {}^{3}_{1}H \rightarrow {}^{4}_{2}He + n + 17{,}6MeV$$

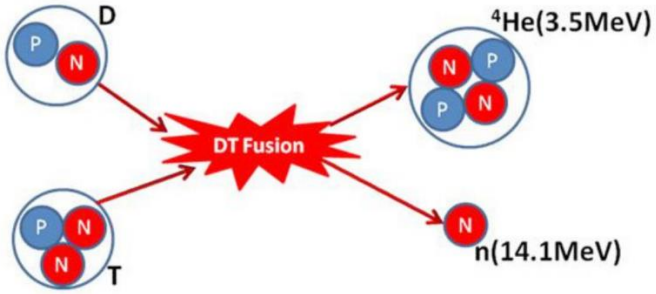

Figure 1-3: Schematic of a D-T fusion reaction [8].

The general notation ${}^{A}_{Z}X$ with "A", being the atomic mass number (number of neutrons and protons present in nucleus) and "Z", being the atomic number (number of protons present in the nucleus).

Furthermore, the energy produced during the reaction is shared inversely to the mass of the particles involved. Thus, Helium4 ${}_{2}^{4}He$, also called “alpha” particle, having 2 protons and 2 neutrons, gets only 20% (3,5 MeV) of the energy produced during the reaction. Instead, the neutron particle obtains the remaining 80% of the energy (13,1 MeV).

$$P_{fus} = 5 \cdot P_{\alpha} \qquad\qquad P_{\alpha} = \frac{P_n}{4}$$

As it also holds true for the other nuclear fission reactors, the neutron particle is the key element that is used to transfer its kinetic energy to the coolant to then produce steam, which is then used to feed a turbine-alternator system for the generation of electricity.

There are also other possible fusion reactions using different type of elements, such as Deuterium-Deuterium or Deuterium-Helium3 among others. However, these reactions would require very high kinetic energy and at temperatures expected for fusion reactions of the order of 10-20 keV (above $100 \cdot 10^6$ K), the most probable reaction to be achieved is the Deuterium-Tritium one [8] as shown in Figure 1-4, in which “fusion cross-section” is intended as a measure of successful collision between a particle at rest and an incident particle, then leading to a fusion reaction.

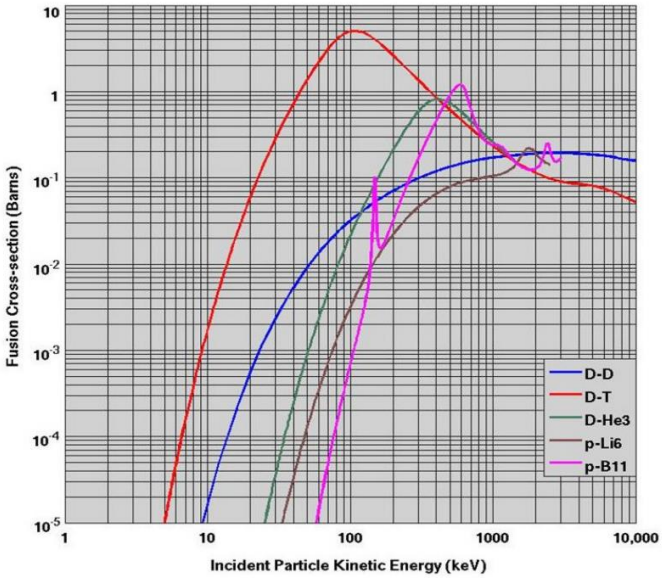

Figure 1-4: fusion cross section of various fusion reactions as a function of the kinetic energy of an incident particle on a stationary target particle [8,17,18].

The complexity of generating and sustaining fusion reactions at a rate sufficient for energy production makes it a difficult endeavour. It simultaneously requires three fundamental conditions for the fuel: [19]

1- it must be heated up to high enough temperatures;
2- it must be compressed to reach sufficient density;
3- it must be confined for a sufficient amount of time.

First of all, heating the fuel at temperatures of the order of $150 \cdot 10^6$ K, causes the fuel to be in the so called fourth state of matter, plasma: a gas made of ions and free electrons in proportion such that electromagnetic interactions govern the gases behavior and still showing macroscopic neutrality. Secondly, the fuel must be compressed to increase the particles' collision rate and energy, increasing in turn the fusion reaction rate. Thirdly, the greater the amount of time in which the previous two conditions are guaranteed, the higher the number and the probability for fusion reactions to occur.

In other words, a combination of temperature T, density n, and confinement time τ_E constitutes the prerequisite for obtaining nuclear fusion reactions. According to the Lawson criterion, in a range between 8 – 25 keV, a minimum value of the so called "triple product" is identified with 15% accuracy:

$$T \cdot n \cdot \tau_E \cong 3{,}12 \cdot 10^{21} \quad [m^{-3} s\ keV]$$

The fulfilment of the Lawson criterion is the main goal of D-T fusion experiments and is mostly related to the achievement of high confinement times τ_E. [20] Several types of experimental devices have been designed to reach this goal in the last 50 years. Nevertheless, there is one that has been studied for a longer amount of time, given that it is considered one of the most promising type of machines: the "Tokamak".

1.3. Tokamaks and ITER

The name “Tokamak” comes from a Russian acronym, its literal translation similar to “Toroidal chamber with magnet coils”. It uses strong magnetic fields to contain and stabilize a superheated plasma made of hydrogen isotopes. Name-giving is its toroidal shape with a complex system of magnetic coils responsible for the plasma confinement, preventing it from encountering the chamber walls and allowing plasma to reach the extreme temperatures and pressures. This type of device makes use of the concept of magnetic confinement fusion. A typical example of Tokamak machine is shown in Figure 1-7.

Several types of Tokamak machines have been built around the world, while others are under construction or development as shown by the yellow dots of Figure 1-5. A few examples are ISSTOK in Portugal, JET in England, ASDEX in Germany, TVC in Switzerland, WEST in France, ADITYA in India, JT-60SA in Japan, Alcator C-Mod in the USA etc.

Furthermore, for the sake of completeness, it should be noted that other types of machines are also available and/or under research, using magnetic confinement fusion differently or utilising alternative concepts.

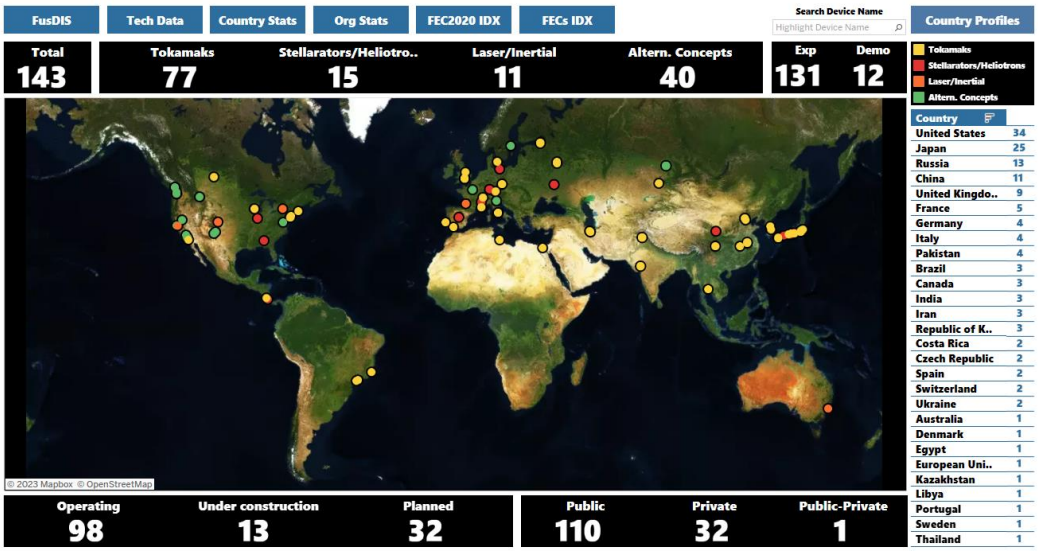

Figure 1-5: IAEA map distribution of fusion devices worldwide [21].

Nevertheless, among all Tokamaks, the “International Thermonuclear Experimental Reactor” ITER, located in Cadarache (FR), takes a prominent role within the nuclear fusion industry. ITER ("The Way" in Latin) is the most ambitious energy projects in the world today, in which 35 nations are collaborating to build the world's largest Tokamak. Thousands of engineers and scientists have contributed to the design of ITER since the idea for an international joint experiment in fusion was first launched in 1985. The ITER Members are China, the European Union, India, Japan, Korea, Russia and the United States. They have been engaging in a decades-long collaboration to build and operate the ITER experimental device, and bring together fusion to a point where a demonstration fusion reactor can be designed. [22]

The ITER construction began in 2007 and nowadays it possible to see how the building for the Tokamak is completed. [23] The Tokamak complex and the ITER plant and auxiliary buildings for First Plasma are almost finished. Several machine components (cryostat, superconducting coils and vessel sectors) are already completed, while the machine assembly has started in 2020 as shown in Figure 1-6.

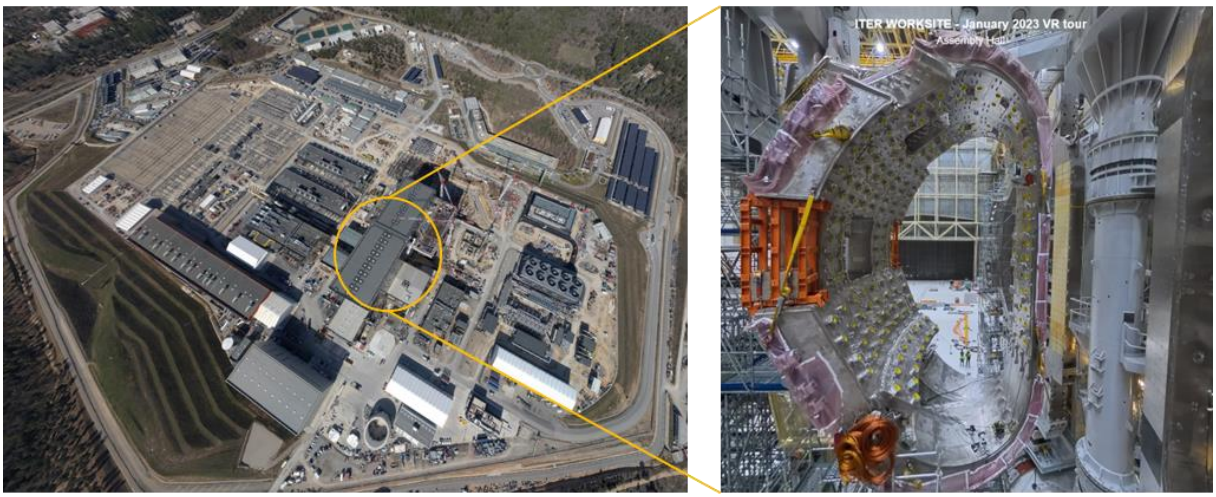

Figure 1-6: ITER construction site (left) and inside the assembly Hall (right) on 1st January 2023 [24].

The recent 29th Fusion Energy Conference (FEC) 2023 (organized by IAEA every 2 years) gave insight into the progress on manufacturing, construction, commissioning and an updated baseline of the ITER project. As stated by the director-general of the ITER Organization, Pietro Barabaschi, since the last FEC many first-of-its-kind components have been assembled, leading to first-of-its-kind difficulties, responsible for a delay in the construction phase. Other responsible factors were the Covid-19 pandemic, additional repairs to major component, adjustment to the French nuclear regulator requirements and the change of First Wall material from Beryllium to Tungsten. The updated baseline is to be presented by mid-2024 postponing the First Plasma campaign, followed by two D-T operational phases. [25]

In the section here below, the fundamental functioning of Tokamak machines is explained. Generally, the toroidal field coils together with the poloidal field coils and in-vessel & out-vessel correction coils, form a complex magnetic system which aims producing strong magnetic fields and currents that entrap the plasma. For better understanding, consider the toroidal coordinate system r, Φ, z as shown in Figure 1-1, where “r” stands for radial direction, Φ for the toroidal (also named “azimuthal”) direction and z for the vertical direction. The “r-z” planes are also called “poloidal”. The superposition of a strong toroidal field $B_{tor}(\Phi)$, due to the toroidal field (TF) coils, and a poloidal field, induced by a toroidal plasma current I_p , produces helically twisted field lines forming nested toroidal surfaces. [8]

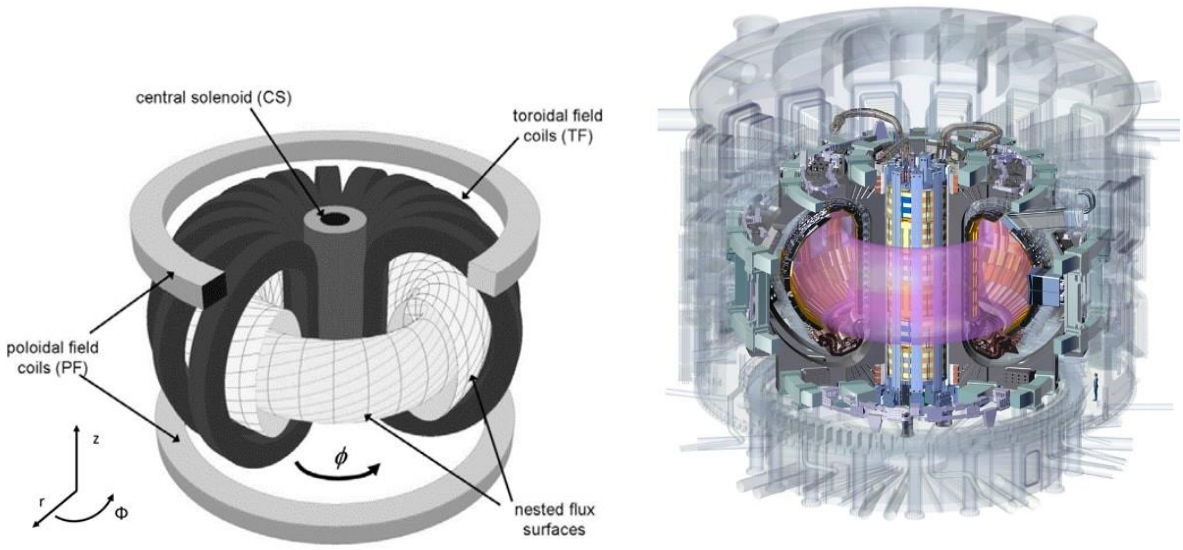

Figure 1-7: schematic representation of the magnetic field system of a Tokamak (left) [8] and partial section of ITER Tokamak with highlight of the Central Solenoid (right) [26].

In other words, the toroidal field coils generate the toroidal magnetic field (Φ direction), imposing a trajectory for the plasma ions to avoid collisions with the First Wall that surrounds it. However, due to the toroidal configuration and machine specifications, the plasma is subjected to vertical and horizontal drifts. To counterbalance them, two systems are put in place.

Firstly, considering a poloidal cross section which is perpendicular to the toroidal direction Φ, the loss of particles in radial direction can be greatly reduced by imposing a poloidal field. To generated it, the rise of a plasma current in the toroidal direction is necessary. Such current is obtained thanks to another inner poloidal field coil called Central Solenoid shown in Figure 1-7. This component, in case of the ITER machine, is considered to be its backbone. [20] It acts as a primary circuit of a transformer, inductively generating a current in the plasma, which instead acts as the secondary circuit of a transformer. Therefore, the generation of a “plasma current” in toroidal direction Φ induces a poloidal field. For ease of understanding, an analogy could be the magnetic field generated by a current flowing through wire. The current represents the plasma current I_p and the generated magnetic field could be considered as the “poloidal” magnetic field.

Secondly, the outer poloidal field coils are used to compensate centrifugal forces directed towards the radial outer direction of the machine. In fact, these coils generate a vertical field into the plasma which in turn, induces a radial inward drift since:

$$F_{lorentz} = q \cdot \vec{v} \times \vec{B}$$

In the end also the correction coils mentioned above allow for better entrapment of the plasma. They are used to better control the many types of instabilities that could arise during the operation of a Tokamak machine.

Additionally, since the energy involved in operating the Tokamak reactor is large, efficiency is key to achieve a positive net energy gain. The losses due to Joule effect must be suppressed by using superconducting materials brought to temperatures close to absolute zero. The TF and PF coils are made of Niobium-tin *Nb-Sn* or Niobium-Titanium *Nb-Ti* and brought to temperatures close to absolute zero, between 4 and 10 K, by a spiral cooling tube in the centre of the multifilament. [11,20]

Figure 1-8: example of ITER's toroidal field conductor.

There still hasn't been a net positive output of energy through a Tokamak machine. The ITER machine, still under construction, is designed to be the world's largest Tokamak with the primary goal to demonstrate the scientific and industrial feasibility of nuclear fusion as a clean and virtually limitless source of energy.

The demonstration of scientific feasibility aims to prove that the amount of fusion power generated in the plasma P_{fus} is much larger than the additional external heating power P_{ext}. A parameter used to quantify this aspect is the plasma power amplification factor:

$$Q = \frac{P_{fus}}{P_{ext}}$$

P_{fus} refers to all the energy obtained during the nuclear fusion reactions, shared in 20% by the alpha particles and 80% by the neutrons used to heat the coolant of the reactor.

P_{ext} refers to all the systems required to heat, confine and shape the plasma.

As a threshold value to pragmatically define the definition of Scientific Feasibility, the chosen criteria is at least 10 times the external heating power required:

$$Q \geq 10$$

In ITER, the target is a Deuterium-Tritium plasma with alpha particles fusion power twice the external heating, respectively $P_{fus} = 100\ MW$ and $P_{ext} = 50\ MW$. Since $P_n = 400\ MW$, $P_{fus} = 500\ MW$ is the total amount of fusion energy released, yielding:

$$Q_{ITER} = 10$$

Previous machines have not been able to reach such value of plasma power amplification factor due to power losses occurring during the process. The main power losses are the prevalent conduction losses and the minor radiation losses present in a confined plasma. Both of these processes cool down the plasma and need to be balanced by external heating power. However, experimental evidence from previous machines indicate that the conduction power losses increase linearly with the size of the machine. Conversely, the fusion power increases cubically with the size. Thus, a bigger machine makes it possible to achieve higher numbers of Q. [20,27,28]

As a direct consequence, the power losses caused by conduction and radiation phenomena manifest the importance of the external heating systems, discussed in the next section.

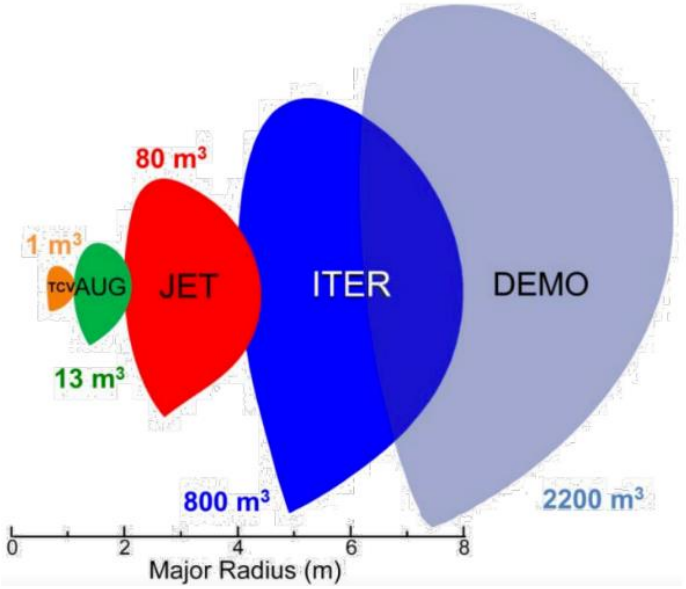

Figure 1-9: poloidal cross section of different Tokamaks.

1.4. Neutral Beam Injector

Three different kinds of sources of external heating are used to reach the target temperature in the ITER Tokamak: two sources of high-frequency electromagnetic wave named “Ion Cyclotron Resonant Heating” and “Electron Cyclotron Resonant Heating”, and “Neutral Beam Injectors” as shown in Figure 1-10. All these systems, besides heating the plasma, are also capable of current drive with different efficiencies.

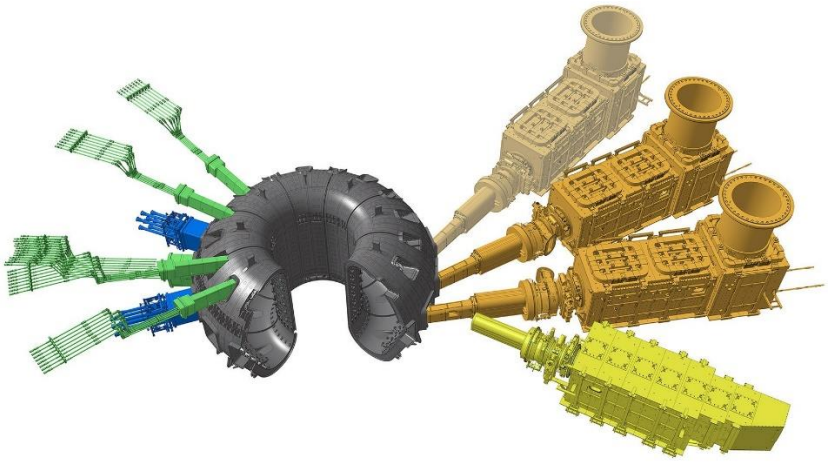

Figure 1-10:ITER vacuum vessel (grey) with 2 Ion Cyclotron Resonant Heating systems (blue), 4 Electron Cyclotron Resonant Heating systems (green) and 2 Neutral Beam Injectors (gold) [29].

Among the three, the Neutral Beam Injection (NBI) stands as a crucial tool. It plays a fundamental role in heating and current drive within the plasma, ensuring it reaches the necessary conditions for self-sustained nuclear fusion.

Nevertheless, before diving into the specifics of the Neutral Beam Injector, it is appropriate to have a brief overview of the other sources of plasma heating utilised in fusion research. The so-called “Electron Cyclotron Heating (ECH)” and “Ion Cyclotron Heating (ICH)” are two prominent techniques that use electromagnetic waves of different frequency to heat the plasma. Their functioning is similar to that of a microwave. In fact, the energy transfer occurs through the absorption of an electromagnetic wave into the plasma medium. The highest efficiency of transfer is achieved when the wave frequency is resonant with some of the fundamental oscillations of the medium. [29] By exciting the gyromagnetic resonance of the plasma’s ions or electrons, respectively in the ranges of 30-120 MHz and 100-200 GHz, precise heating of the plasma is accomplished.

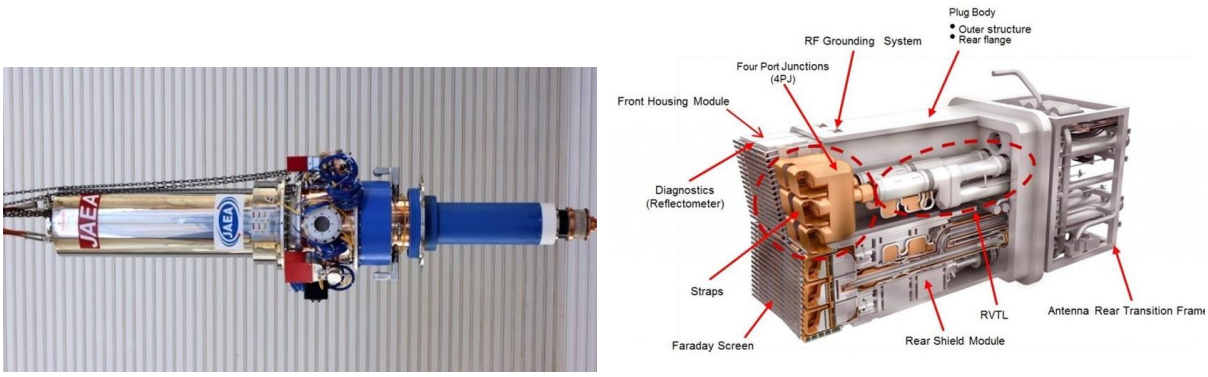

Figure 1-11: ITER gyrotron for beam generation of ECH (left) and ITER ICH antennas (right) [29].

While these methods have their merits, NBI distinguishes itself by directly injecting high-energy neutral particles into the plasma, transferring their kinetic energy to the fuel, consequently raising its temperature. The primary objective of the NBI is twofold: to heat the plasma within the Tokamak to the extreme temperatures required for nuclear fusion and to provide means of driving current within the plasma. These objectives are essential for achieving and maintaining the necessary conditions of a plasma's temperature and shape for a self-sustaining fusion reaction.

Furthermore, NBI can use positive or negative ion beam accelerator for the final neutral beam. However, in both methods share the use of the principles of particle acceleration and charge exchange.

The process for the generation of a neutral beam begins with the creation of a high-energy ion source, typically using hydrogen or deuterium. These ions are charged atoms, hence they can then be accelerated to a significant fraction of the speed of light using a large electric potential difference. Once the ions reach the desired kinetic energy, they are directed into a neutralizer, typically composed of gas, where they undergo charge exchange. This process is necessary because charged particles would not be able to pass through the intense magnetic barrier generated by the tokamak coils. Therefore, during this crucial step, the high-energy ions lose their electric charge and are converted into fast-moving neutral particles. However, since the neutralization process is not 100% efficient, the remaining charged particles must be deflected out of the main neutral beam source. For this reason, an ion dump is put in place with the objective of charged particles removal by means of an imposed electric field orthogonal to the axis of the ion beam direction.

Thus, the construction of a Neutral Beam Injector consists of several critical components, with four major parts most of them shielded by external magnetic fields induced by the tokamak magnetic system: [11,20]

- Ion Source: generation of negative and/or positive ions;
- Acceleration Grids: ion acceleration increasing the kinetic energy;
- Neutralizer: conversion of charged beam to neutral beam;

- Electrostatic Residual Ion Dump: removal of residual ions before entering the Plasma Chamber.

These sections require a significant input of energy to operate, primarily to generate and accelerate the ions. Balancing efficiency with energy consumption is a key challenge in NBI technology. In case of the NBI designed for the ITER Tokamak, the efficiency is around 30% since it delivers 16.5 MW of power to the plasma with an input of 56 MW of power. [11,30] Due to the need of powerful ion sources and acceleration grids with electric potential difference of 1 MV, NBI systems can be quite large and reach dimensions of the other of 20-30 m. Therefore, making compact and efficient designs is a priority for researchers.

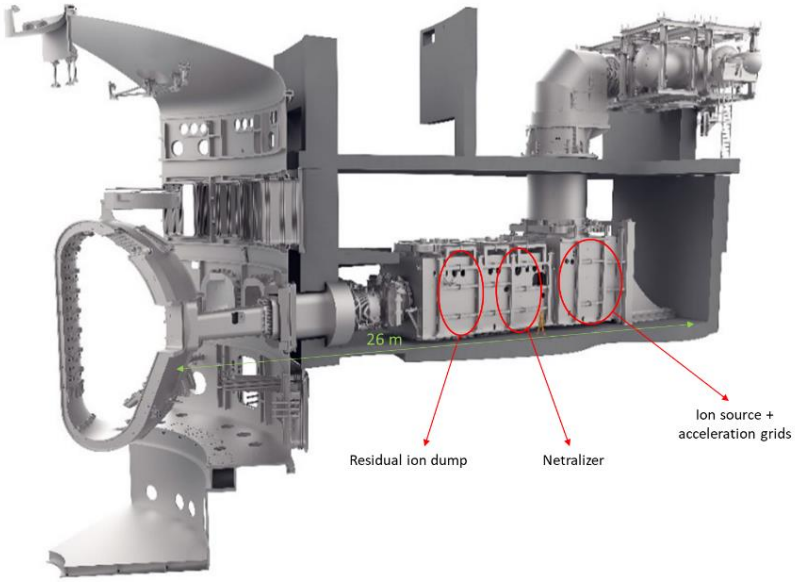

Figure 1-12: one of ITER NBI heating systems (plasma chamber is at left) [29].

A prototype of the Neutral Beam Injector designed for ITER has been built on site at “Consorzio RFX” in Italy, with the name of “MITICA” experiment, short for Megavolt ITER Injector and Concept Advancement. It is a flexible system developed to test and validate the NBI technology for ITER. It is the result of the collaboration within the framework of the ITER Organization and the European Domestic Agency for ITER (F4E), in collaboration with the Japanese and the Indian Domestic Agencies, and with other European and Japanese laboratories, such as IPP-Garching, QST-Naka and CEA-Cadarache. [31]

MITICA belongs to the category of NBIs which are based on a negative ion source since there is experimental evidence of higher values of neutralization efficiency shown for higher values of beam energies [11], leading to an overall higher efficiency of the external heating system.

2. Introduction to MITICA BS and post-insulators

2.1. MITICA acceleration grids

The thesis focuses on one of the four critical sections that constitute an NBI: the Acceleration Grids. For this reason, the current and the following sections dig into deeper detail of the Acceleration Grids and their constituents.

In case of MITICA, negatively charged particles are produced by the negative Ion Source and extractor, formed by the Plasma Chamber, Plasma Grid (PG) and Extraction Grid (EG). These components are held at -1MV and are responsible for the production and extraction of negative deuterium D^- ions at -1MV, making sure not to attract other negatively charged particles, such as free running electrons towards the acceleration grids. Otherwise, this would result into an overall worse efficiency of the accelerator and increased heat loads on the grids. [32]

Subsequently, these negative ions at -1MV are accelerated through a series of 5 electrodes, generating a total electric potential difference of 1 MV: [33]

1) Acceleration Grid 1 (AG1): -800 kV.
2) Acceleration Grid 2 (AG2): -600 kV.
3) Acceleration Grid 3 (AG3): -400 kV.
4) Acceleration Grid 4 (AG4): -200 kV.
5) Grounded Grid (GG) and Vacuum Vessel: ground potential.

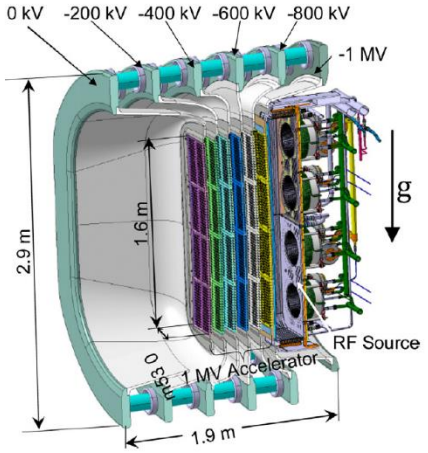

Figure 2-1: Vertical section view of the half MITICA Beam Source electrostatic accelerator.

This structure is shown in Figure 2-1. [34] Each of the electrodes consists of an acceleration frame and an Acceleration Grid, which form together a series of C-shaped elements (sometimes called “bathtub-like”). [35] Note that the -1MV represents the Ion Source attached to the Accelerator Grids.

Due to their different voltages, electrical insulation must be assured for all electrodes [33], obtained through:

- Alumina post-insulators between grids (cylindrical ceramic component in light blue in Figure 2-1);
- vacuum gaps (and low pressure hydrogen during operation) ranging from 88 mm for 200kV voltage, up to 600 mm for 1MV voltage.

The proposed insulation concept has never been tested before because other existing NBIs for fusion, such as the NBI for JT-60 (570 kV) and MTF (1 MV), make use of high-pressure gas (SF_6) in case of voltage in all gaps subjected to a voltage larger than 200kV. [33] However, SF_6 cannot be used in MITICA and in ITER NBI due to the degradation of SF_6 gas when subjected to neutron flux produced by fusion reactions. Hence, electrical and mechanical verifications are required to validate a conceptual design of this insulation system designed for MITICA Beam Source (BS).

At first, structural numerical simulations with an accurate 3D model were carried out to estimate the most stressed components of the whole assembly. The Ion Source and the five-stage accelerator form a cantilevered structure sustained from the grounded stage causing considerable stress to the post-insulator, which required an exclusive R&D work.

However, a more critical aspect concerns the vacuum gaps. Studies of probabilistic nature show that the most critical gap is the longer one of 600 mm, between the -1MV surface of the BS and the Vacuum Vessel at ground potential. For this reason, an additional electrostatic shield at -600kV around the BS (named “RF source” in Figure 2-1) has been designed and will be used only if experimental results show that it is necessary to ensure nominal operation of the NBI. [33] Consequently, the structural verification must also consider the weight of the additional protective shield at -600kV.

2.2. R&D of Alumina post-insulators

As previously mentioned and shown in figure Figure 2-2, the cantilevered configuration of the structure produces non-negligible stresses on the Alumina post-insulator, needing further attention in its design and development.

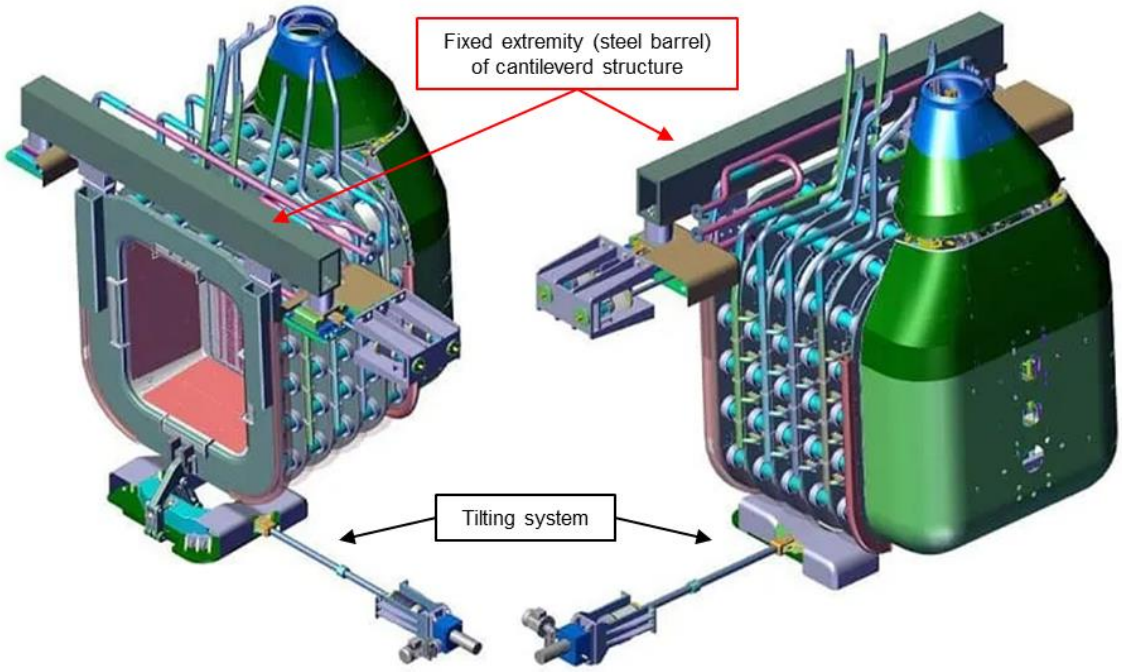

Figure 2-2: cantilevered structure of MITICA Beam Source.

A post-insulator is a component of cylindrical form which connects and supports the “bathtub-like” elements. It has both mechanical and electrical insulation requirements since it must withstand the weight of the cantilevered structure and ensure no breakdown occurs in between

the different acceleration grids, subjected to a 200 kV voltage. An example of Alumina post-insulator is shown in Figure 2-3.

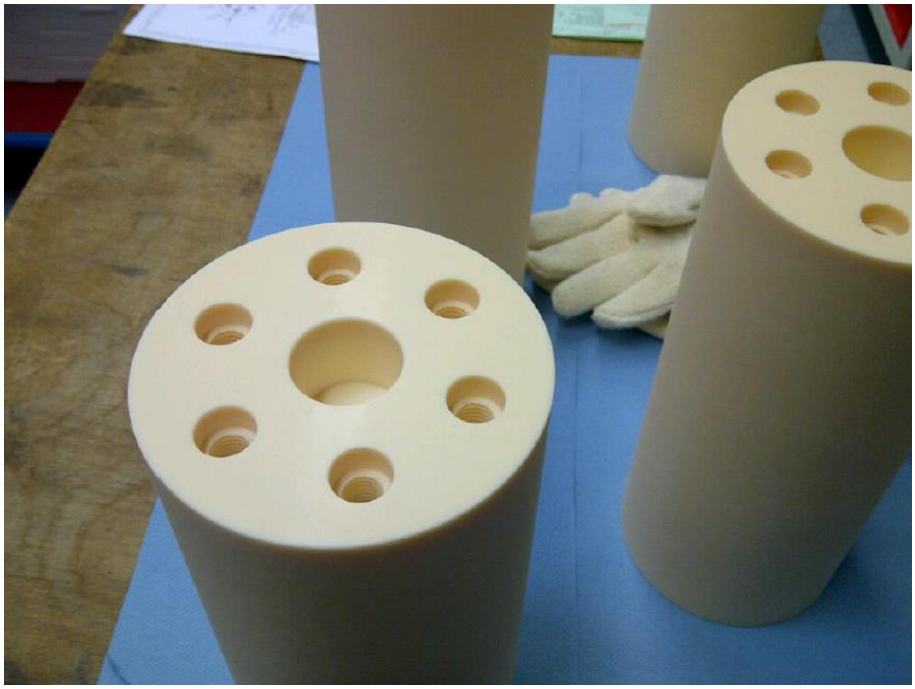

Figure 2-3: example of “type a” fabricated MITICA BS Alumina post-insulator [35].

Concerning the Alumina post-insulators, extensive R&D has been carried out in collaboration with Friatec [36] to define a ceramic post-insulator with the best material choice and withstanding voltage considering the structural and manufacturing issues. Several prototypes have been investigated to find out the geometry and material which best satisfy the high voltage holding and mechanical testing required for such component.

The final design of the Alumina post-insulator is a 130 mm diameter cylinder of 280 mm height, with a hollow cave of 35.3 mm and is made of high purity Alumina C799 as shown in Figure 2-4. For sake of clarity, the reference frame shown is the “testbed” reference frame.

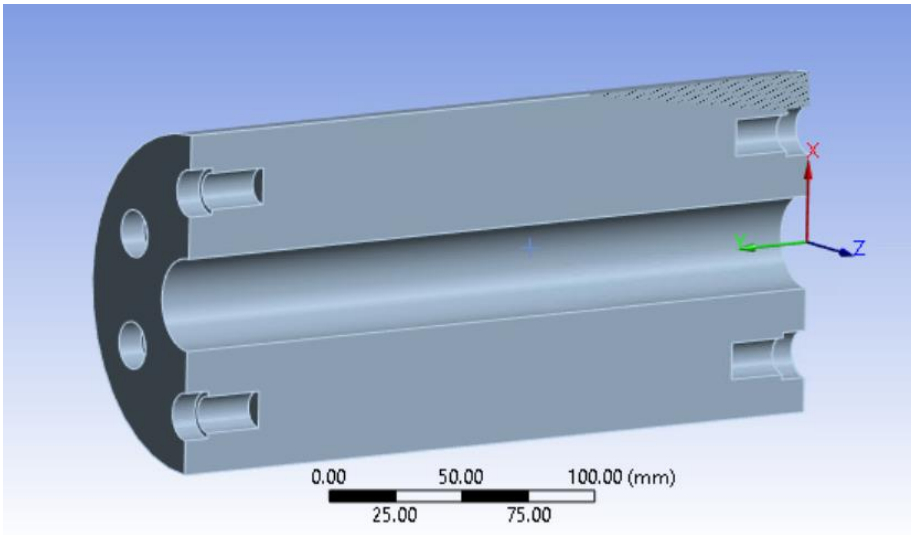

Figure 2-4: simplified 3D model of Alumina post-insulator "prototype b" [36] consistent with "testbed" reference frame.

The ceramic insulator is then connected to the structure via a couple of Stainless-Steel flanges directly bolted through 12 (6 per side) M14 screws on the frames sustaining the acceleration grids. The total distance "L" between the flanges is of 330 mm. Figure illustrates how such insulators will be installed on the acceleration frames of MITICA (the photo is from the MITICA Mock-Up electrodes, which will be described in the next sections).

According to the numerical simulation [34,36], the most loaded post-insulators are located at the bottom part of the grounded frame, where the accelerator leans against the BS tilting system. [37] They are subjected to a combination of 3D forces and moments, which can be reconducted to a set of equilibrated system of forces and moments at the contacts "A" and "B" between the insulator and the flanges and along the insulator symmetry axis (see Figure 2-4). According to the reference frame in Figure 2-6, the stress and values are equal and opposite for points "A" and "B" and are equal to:

- compressive loads of 52.02 kN in y direction;
- bending moment of 5.56 MN*mm in z direction;
- a smaller shear force of 9.66 kN in x direction.

Figure 2-5: Installation of insulators on a frame of the MITICA Mock-Up Beam Source. [38]

All of these values include possible effects of dynamic loads during seismic activity or handling operations, by applying a safety factor of 2. Besides, to take into consideration the worst-case scenario, the compressive loads are replaced by tensile ones, by inverting the force direction. This decision also eases the experimental verification of the ceramic insulator prototype. In fact, tensile tests, apart from applying traction forces being more severe than compressive ones, avoid the risk of non-valid results due to buckling or another non-linear behavior. To recreate the equilibrated loads through the usage of a tensile test machine, a dedicated tool has been designed to apply the specific loads. [34] This choice allowed to easily verify different alumina prototypes thanks to tensile tests to check if the component can satisfy the load requirements as shown in Figure 2-6.

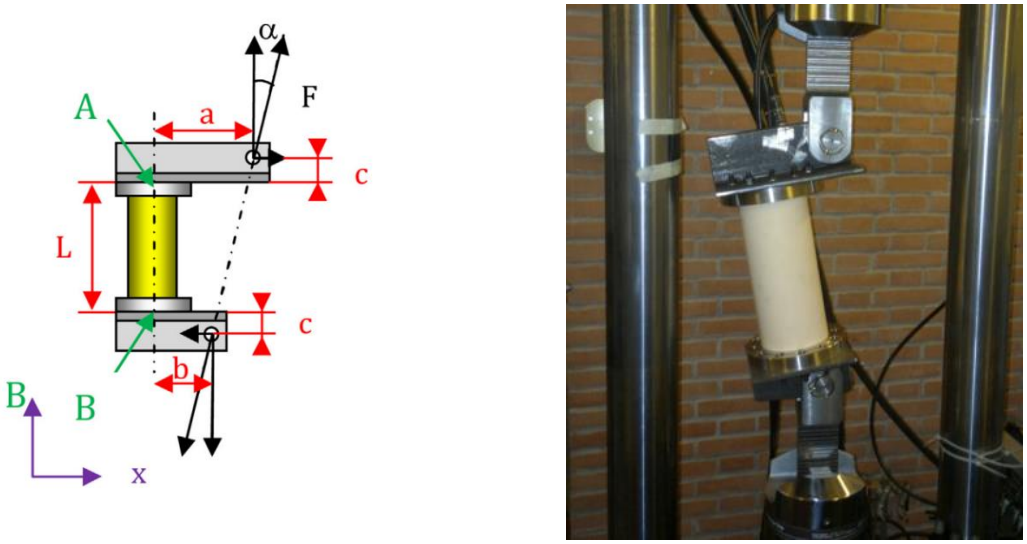

Figure 2-6: equipment sketch design (left) and insulator prototype during testing (right) [34].

The final design of Alumina insulator prototype, referred to as “type b2” [34], successfully passed the mechanical test withstanding an external tensile force of F=80 kN without any structural damage.

Regarding the electrical insulation requirements, the same Alumina prototype has the requirement to sustain 200 kV without breakdown. The experimental verification consisted in 140 h of high voltage conditioning, reaching 240 kV without breakdowns for at least 3 hours. The achievement of this result required the insertion and redesign of a rod made of Vespel®, forcing it inside the hollow cavity of the ceramic insulator via interference coupling.

In this way both mechanical and electrical verifications have been carried out for the final prototype of Alumina post-insulator. However, considering the electrical insulation of the structure, there is still the need to verify the absence of breakdowns (“voltage holding”) in the most critical vacuum gap of 600 mm between the -1MV surface of the BS and the Vacuum Vessel at ground potential. For this purpose, a prototype of the MITICA experiment has been designed, developed and built to conduct an experimental campaign of electrical tests during 2022-2023.

2.3. MITICA Beam Source Mock-Up

The most effective way to verify and optimize the High Voltage vacuum insulation of the entire structure of the MITICA Beam Source (BS) is through experimental validation of a prototype of the beam source reproducing only the geometry relevant for High Voltage (HV) holding.

It is fundamental to distinguish the “MITICA Beam Source” from the “MITICA Mock-Up Beam Source”. The former is the prototype of the complete NBI designed to be integrated as part of ITER’s heating systems. Instead, the latter is a 1:1 scale Mock-Up of the Beam Source containing only the electrodes whose geometry is relevant for electrical tests.

It is important to stress out that the MITICA Mock-Up Beam Source simplifies the geometry of the electrodes of the acceleration grids and uses different materials. Using the same materials would be more expensive and useless to prove the HV vacuum holding of the MITICA BS. These differences to the original design of the MITICA BS are important from structural standpoint and are summarised in the following: [39]

- the Acceleration Grids are not C-shaped, instead the “grid support frames” are represented only by their own support frame;
- Grid frames made in aluminium;
- The insulators connecting the frames are made of PEEK;
- There are only 8 insulators between the ME10 and the ME08 and twelve between the other electrode frames;
- The grid segments and the nested supporting frames on the Mock-Up Beam Source are replaced by Stainless Steel sheets;
- The internal components of the real BS such as RF drivers, magnetic field systems, caesium ovens are not present.

The Mock-Up Beam Source is constituted by a series of five electrode with frames connected by PEEK post-insulators. Depending on the result of the Mock-Up tests, it may be necessary to mount an additional Electrostatic Shield at -600kV at one extremity referred to as “ES06”. In case breakdown occurs even with the electrostatic shield at -600 kV, another shield is foreseen to be put at -200 kV, referred to as “ES02”. The electrical tests have started on November 2023 and will continue at least until the end of 2023.

An image of the MITICA Mock-Up electrodes without the electrostatic shield is shown Figure 2-7. [40] The whole structure is cantilevered and supported by a steel beam at the grounded grid and two inferior supports who can move to allow tilting of the accelerator.

According to the documents [40–42]:

- ME00 mock-up of electrode at ground potential, directly attached to the vessel by a steel barrel;
- ME02 mock-up of electrode at -200 kV;
- ME04 mock-up of electrode at -400 kV;
- ME06 mock-up of electrode at -600 kV;
- ME08 mock-up of electrode at -800 kV;

- If necessary, also the effect of an intermediate electrostatic shield (ES06) at -600 kV will be tested;

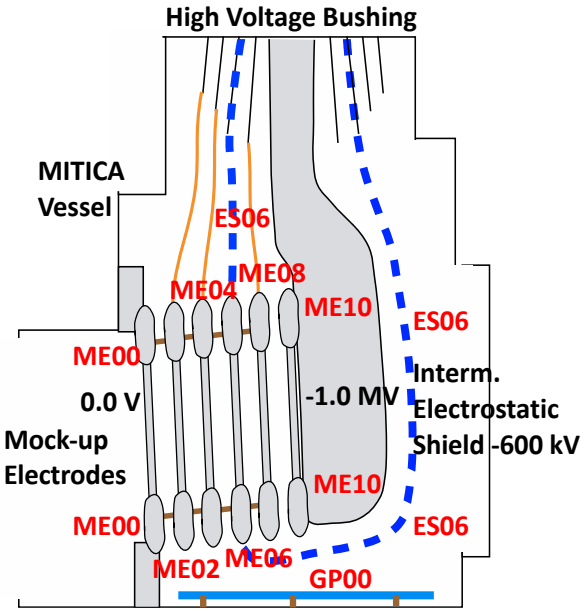

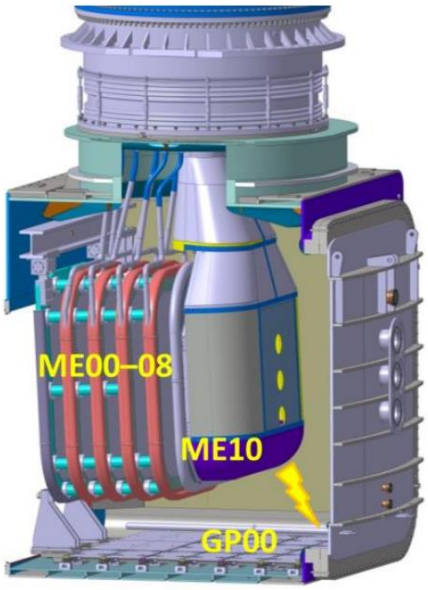

Figure 2-7: Scheme of experimental setup for HV vacuum test of MITICA Mock-Up electrodes (left) [33] and 3D model of MITICA Mock-Up electrodes without intermediate electrostatic shield ES06 [40].

The electrode ME10 represents the ion source at is at -1MV, where generation and extraction of negative deuterium ions occurs. The Electrode ME00 is mechanically attached to the vacuum vessel. The electrodes ME02 to ME08 are mechanically supported by means of cylindrical post-insulators made of PEEK bolted in between the electrode frames. Twelve insulators are used for supporting each of the first 4 electrodes (ME00-ME06). Instead, only 8 are present between the ME006 and ME08 grids. The Mock-Up of the ion Source (ME10) is instead mechanically attached to the High Voltage Bushing (HVB).

The whole structure constitutes a cantilevered beam weighting about 4 tons, compared to the 14 tons of the original (real) MITICA BS.

Due to the change of the post-insulator material of the Mock-Up with respect to the real MITICA Beam Source (from Alumina to PEEK), new structural simulations and verification had to be done both to the insulators and to the whole structure. The experimental nature of the thesis focuses on the structural validation for the mechanical loads foreseen on the PEEK insulators.

2.4. Mechanical loads on PEEK insulators

Overall, the most critical component in terms of structural verifications are the PEEK insulators. Even though preliminary FEM verifications of the insulators have been made, experimental validations are considered very important to fully validate their design. Considering the numerical model of the MITICA Mock-Up electrode structure and the numbering of the insulators [41] shown in Figure 2-8, the most stressed insulators are in between ME00 and ME02.

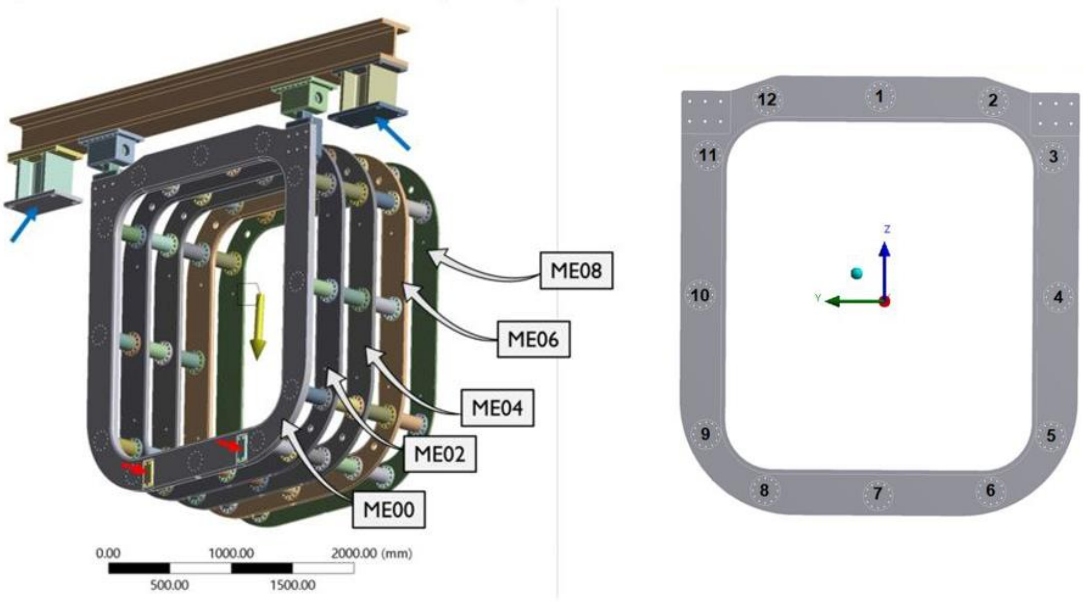

Figure 2-8: MITICA Mock-Up accelerator electrodes (left) and numbering of insulator per grid (right) [41].

The foreseen mechanical loads on the insulators have been numerically evaluated for three different load cases: [43]

- normal operation (NO);
- NO + seismic load 1 (SL-1);
- NO + seismic load 2 (SL-2).

The NO condition corresponds to the Mock-Up accelerator electrodes loaded by its own weight and rotated by 1° around its hinges, corresponding to -50 mm displacement in x direction according to the “ANSYS frame” shown in Figure 2-8.

The SL-1 condition correspond to a seismic event with probability of 10^{-2} per year (a foreseeable event) after which the facility must operate without special maintenance or test. In case of a combination between NO and SL-1 the structure should survive 5 events, in which each of the assures 10 maximal stress cycles whenever a fatigue or a cyclic analysis is required.

The SL-2 condition corresponds to the seismic level required by French nuclear practice (RFS 2001/01), for which the facility must survive once maintaining all the safety functions.

Among those, the one of interest for the Mock-Up electrodes is the normal operation condition since its usage is foreseen only to conduct the experimental campaign for the verification of the MITICA BS electrical insulation.

For the experimental validation of the PEEK insulators, the tensile test specifically designed for Alumina insulators [34] is used as well to test the most critical loads of the PEEK insulators of the Mock-Up electrodes. Therefore, it is useful to determine the forces and bending moments according to the same reference frame as of the "testbed" shown in Figure 2-9.

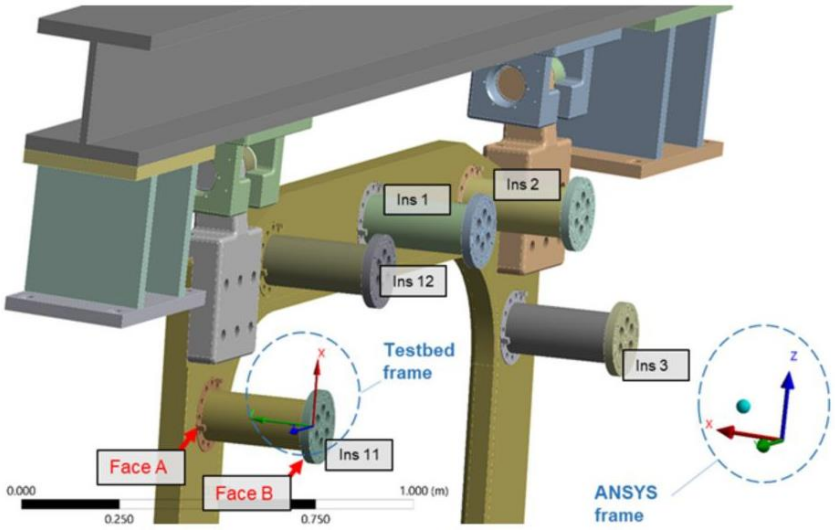

Figure 2-9: MITICA Mock-Up electrode frame at ground potential (ME00) with focus on "ANSYS" and "testbed" reference frames [41].

The most loaded insulators, their forces and moments are shown in Table 2. The insulator n° 2 has the largest traction force, while the insulator n° 3 has the largest shear force and bending moments.[41] To consider the effects of additional seismic and handling operations a penalty factor of 100% is applied to all loads, doubling them. Furthermore, the loads corresponding to compression loads are not studied since they are not considered as critical as tension forces.

Insulator	$F_{X,A}$	$F_{Y,A}$	$M_{Z,A}$	$F_{X,B}$	$F_{Y,B}$	$M_{Z,B}$	F_X/F_Y	Main load description
n°	[N]	[N]	[N·m]	[N]	[N]	[N·m]	/	/
Ins. 2	2196	5859	582	-2063	-5864	122	0,4	traction
Ins. 3	4377	541	935	-4243	-546	439	8,1	Traction, shear dominant

Table 2: most critical insulator loads in between ME00-ME02 at points A and B according to "testbed" reference frame [41].

2.5. Poly-ether-ether-ketone PEEK

As already mentioned, during the design of the MITICA Mock-Up electrodes, different materials were chosen to satisfy mechanical and electrical requirements at a reasonable cost. Regarding the post-insulators, a good compromise is offered by engineering thermoplastics. They offer many advantages such as corrosion resistance, lightness, but especially economy in fabrication.

The precise material chosen is PEEK 450G (not fiber reinforced), a polyketone among the highest performing materials in the world. It shows excellent environmental resistance, high mechanical properties, resistance to chemical environments at high temperature, excellent friction and wear resistance and impact resistance. [44]

The principal properties, also needed for numerical simulation, are listed in Table 3.

Density	Elastic Modulus "E"	Tensile Yield Strenght	Ultimate Strenght
$Kg \cdot m^{-3}$	GPa	MPa	MPa
1310	3,8 (at 23°C)	99,5	106,5

Table 3: material properties of PEEK material.

It is necessary to point out that these properties corresponded to the PEEK plastic material found in ANSYS engineering libraries, which does not properly correspond to the 450G properties. Nevertheless, this decision was taken to ease and speed up the modelling of the tensile test with the experimental set-up explained later. In fact, even if more accurate material properties were used, an experimental validation of the PEEK insulator would have been necessary anyways. Furthermore, as shown in Table 4, the more accurate properties do not significantly differ from the ones suggested by the ANSYS PEEK plastic material.

Density	Elastic Modulus "E"	Tensile Yield Strenght	Ultimate Strenght
$Kg \cdot m^{-3}$	GPa	MPa	MPa
1300	4 (at 23°C)	98	/

Table 4: accurate mechanical properties of PEEK 450G [45].

3. Experimental test and results for PEEK insulators validation of MITICA Mock-Up Beam Source

3.1. Mechanical configuration and experimental targets

The numerical modelling of the MITICA BS Mock-Up electrodes [42] and of the MITICA BS post-insulators [35] together with previous tests on the alumina post insulator [36] indicate which new stresses such component should resist and what equipment is needed for experimental verification.

To simplify the test procedure and shorten the preparation time for the tests, it has been decided, to use the same equipment as the one used for the alumina insulators in previous similar tests. However, while on the real MITICA accelerator the alumina insulators are principally loaded in tension, the PEEK insulators of the Mock-Up electrodes undergo larger and dominant shear forces. For the most critical insulators, identified as n° 3, the load is almost pure shear.

The set of forces and moments generated during the tensile tests are defined by the Eq I, where the geometric parameters a, b, c and α are defined by Figure 2-6. This set of equations explains the issue related to the use of the set-up (Figure 2-6) designed for Alumina insulators [36] to test the PEEK insulators: a large traction force is required to reach the target shear force, which could cause a breaking of the insulator before the shear target is reached.

In other words, the force "F" that needs to be applied by the tensile machine must be high in order to achieve high shear force "$F_{X,A}$" due to the conversion constant 0,182. Thus, besides the critical shear force, a huge traction force is applied at the same time which could break the insulator before the target shear force is reached. In such case, mechanical pure shear tests should be made to validate the insulator design. [41]

$$\text{(Eq I)} \quad \begin{cases} F_{X,A} = -F_{X,B} = F\sin(\alpha) & = 0.182F \\ F_{Y,A} = -F_{Y,B} = F\cos(\alpha) & = 0.983F \\ M_{Z,A} = F(\mathrm{a} * \cos(\alpha) - c * \sin(\alpha)) & = 0.105F \\ M_{Z,B} = -F(\mathrm{b} * \cos(\alpha) + c * \sin(\alpha)) & = -0.045F \end{cases}$$

As described [41], the test has the following 2 targets:

- the highest expected loads of the insulators most loaded in tension (referred to as insulator 2) are reached with a machine tensile force of 24.1 kN;
- With a tensile force of 48kN, the highest loads of the insulators most loaded in shear (referred to as insulator 3) are reached.

However, with the second target, the other loads result to be much higher than compared with the real model. In fact, since the largest shear force applied is on insulator n° 3 with $\boldsymbol{F_{X,A}}$ equal to $\mathbf{8754\ N}$, considering the 100% penalty factor, the corresponding traction force that needs to be applied by the tensile machine is about $\mathbf{F = F_{X,A}/0.182 = 47992\ N \approx 48\ kN}$.

As Table 5 shows, by applying 48 kN with the tensile machine, all worst loading conditions of insulators 2 and 3 are at least doubled. On the other side, the traction force is considerably higher with 47.2 kN instead of 5.9 kN. This condition could lead to a premature rupture of the component before reaching the second imposed target.

	$F_{X,A}$ [N]	$F_{Y,A}$ [N]	$M_{Z,A}$ [N·m]	$F_{X,B}$ [N]	$F_{Y,B}$ [N]	$M_{Z,B}$ [N·m]
Largest tensile machine traction force			47992			
Corresponding loads	8754	47186	5043	-8754	-47186	2153
Worst loadings of Ins. 2 and 3	4377	5859	935	-4243	-5864	439
Corresponding loads / worst loadings	2	8,1	5,3	2,1	8	4,9

Table 5: comparison of imposed forces and moments from the tensile machine with the worst insulators loading conditions derived by numerical simulations.

The tests were performed on a total number of 4 PEEK insulators. The first pair has been tested on 23rd March 2023 to assess around which value of tensile force fracture occurs and whether the component would resist nominal loads. The second pair has been tested afterwards, on 7th June 2023, with the additional usage of strain gauges to see if further information about load distribution until fracture could be derived.

3.2. Discussion on the test set-up and alternative solutions

As visible on Eq I and Figure 2-6, the tensile test set-up available is not well suited to produce a large shear force on the sample. A first solution would consist in increasing the angle α. This can be done by inverting the orientation of one bracket respect to the other, as shown on Figure 3-1.

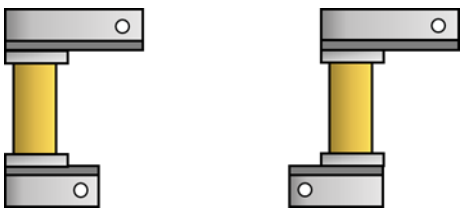

Figure 3-1: inversion of bracket respective orientation to increase the shear.

The advantage of such configuration is that shear and traction target forces are reached with a machine tensile force of 15 kN. This value is less than half of the target value for the shear force (48 kN) set for the original configuration of the bracket. However, in this configuration a very large machine tensile force (81 kN) is required to reach the target bending moment. This target is by far greater than the target set by the original experimental set up (48 kN) and it increases the chances of the insulator's mechanical breakdown due to excessive shear and traction forces before the target value for the bending moment is reached.

Building new brackets for the tensile test to increase the eccentricity of the anchor points would consume time and resources for an insufficient outcome. Instead, it would be more reasonable to change the set-up from a tensile test to a pure shear test. This could be done as follows: two insulators are connected through their flanges to a central plate, which is pulled in a direction perpendicular to the insulator axes. This setup is illustrated by Figure 3-2.

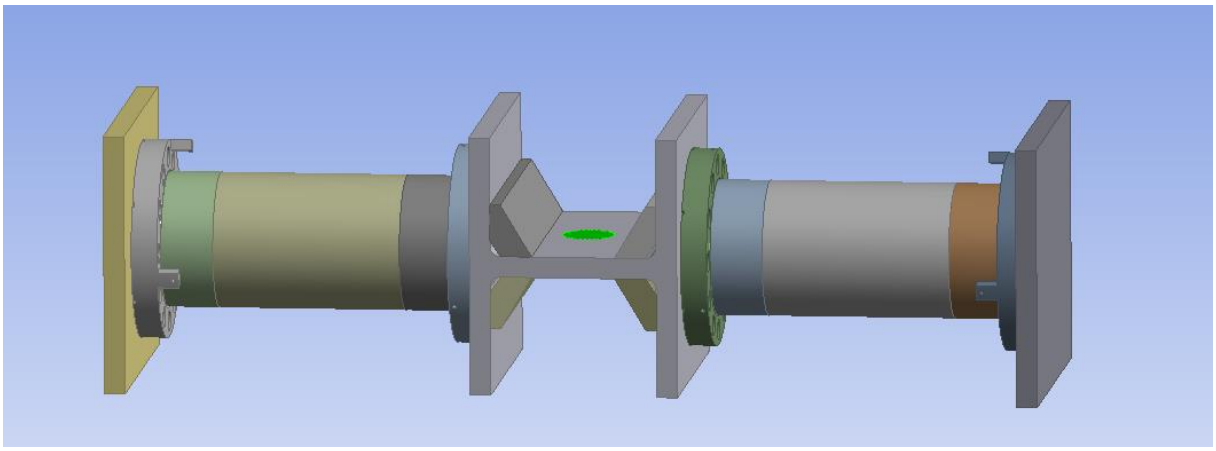

Figure 3-2: example of setup for a pure shear test: the traction force is applied at the green-highlighted anchor point, along a direction perpendicular to the insulator axes.

It was foreseen to implement this last solution in the case where the insulator would break before reaching the target shear force with the tensile test set-up. In the end, this target was reached with a large margin, hence it was decided not to investigate further on the pure shear testing set-up.

3.3. Mechanical test

3.3.1. Equipment

The machine used for the tensile tests is a “810 material test system MTS” [46] with a hydraulic grip “MTS 647 hydraulic Wedge Grip”. [47] Correct installation and preparation of the machine should be ensured to get reliable results. The tests were performed at the Department of Management and Engineering of the University of Padova in Vicenza and Figure 3-3 shows the equipment and the set up used for the experimental verification, which is the same as used on the alumina post insulators tests. [36]

Figure 3-3: PEEK insulator assembly and testing configuration.

3.3.2. Procedure

To prepare the sample for the test, the PEEK insulator’s extremities are fixed to the flanges by 12 (6 per side) M14 bolts with a tightening torque of 38 Nm, using a torque wrench. Then, the flanges are fixed to the tool designed for the structural test by mean of 20 (10 per side) M10 bolts with the same tightening torque of 38 Nm. During the fixing procedure of the parts, the assembly has been laid down on a horizontal plane to facilitate the alignment between parts. Afterwards, the remaining parts of the structure are fixed to the hydraulic grip of the machine, still ensuring proper vertical alignment.

As previously mentioned, the tensile machine should be prepared by executing some cyclic loading to reduce eventual friction present due to its inactivity.

The 4 PEEK post-insulators have been loaded differently. The first sample is used to verify whether the component survives the foreseen loading condition [41], reaching or not the target value of 48 kN, and to define the value for which fracture occurs. The loads and cycles applied are specified in Table 6.

Cycle number	1	2	3	4
Force target [kN]	98	40	80	Fracture at 87

Table 6: loads and cycles applied on first PEEK sample.

The reason why the first cycle reached an uncommon value of 98 kN is that, not knowing if the isolator would survive, a too high sampling rate has been chosen, so that the test had to be interrupted before the breaking point could be reached.

Instead, the second sample is used to see the component's behavior below the expected nominal operational stress level (48kN) and slightly above it. Also, after 5 cycles, this component has then been stressed until fracture. The cycles and loads are specified at Table 7.

Cycle number	1	2	3	4	5	6
Force target [kN]	20	40	50	50	60	Fracture at 103,7kN

Table 7: loads and cycles applied on second PEEK sample.

For the third PEEK insulator, the chosen cyclic loadings are slightly higher to better understand if high loads would greatly affect the component's stability. The cycles and loads are specified at Table 8.

Cycle number	1	2	3	4	5
Force target [kN]	20	40	60	80	Fracture at 94,7kN

Table 8: loads and cycles for the third PEEK sample.

The same loading cycles of the third sample have been applied to the fourth PEEK insulator. But this time a different orientation has been chosen as shown in Figure 3-4 to investigate if a different orientation could greatly affect the results. In fact, in the last configuration used for the fourth PEEK sample, one M14 screw is subjected firstly to most of the bending moment and traction forces causing a fracture at lower values of machine traction force. The cycles and loads are specified at Table 9.

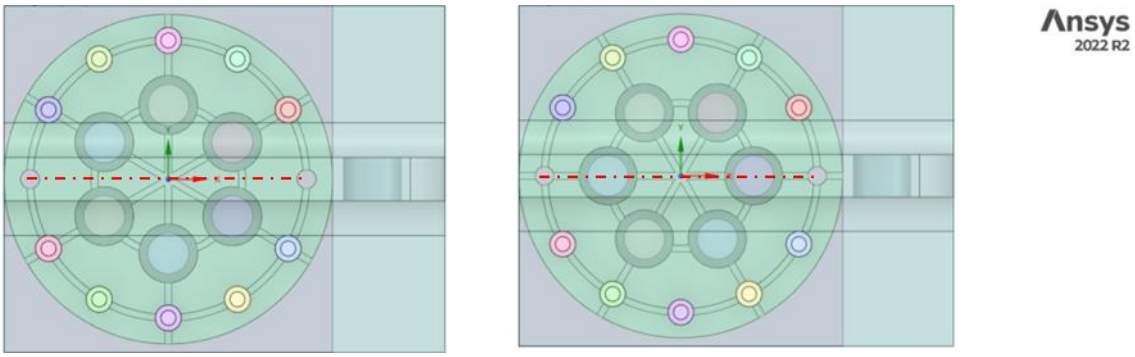

Figure 3-4: Top view of PEEK insulator in the original orientation for the first three samples (left) and different orientation for the fourth PEEK insulator (right).

It is important to mention that the reference frame shown in Figure 3-4 is not consistent with the “testbed” reference frame used until now.

Cycle number	1	2	3	4	5
Force target [kN]	20	40	60	80	Fracture at 97kN

Table 9: loads and cycles for the fourth PEEK sample.

3.3.3. PEEK sample results

The following sections shows the results obtained for each of the 4 PEEK insulators showing the cyclic loadings with no fracture occurring separately from the fracture curve. The former gives indication of whether plasticity or hysteresis occurs, and the latter identifies the insulators' ultimate strength.

It should be noted that the loading curves for the first PEEK sample are different to the others for reasons explained later, so that it is considered less reliable than the others.

At the end, a comparison of PEEK and Alumina insulators loading curve is show as well highlighting the expectable difference of mechanical behavior between ceramic and plastic materials.

3.3.3.1. Cyclic loadings without fracture

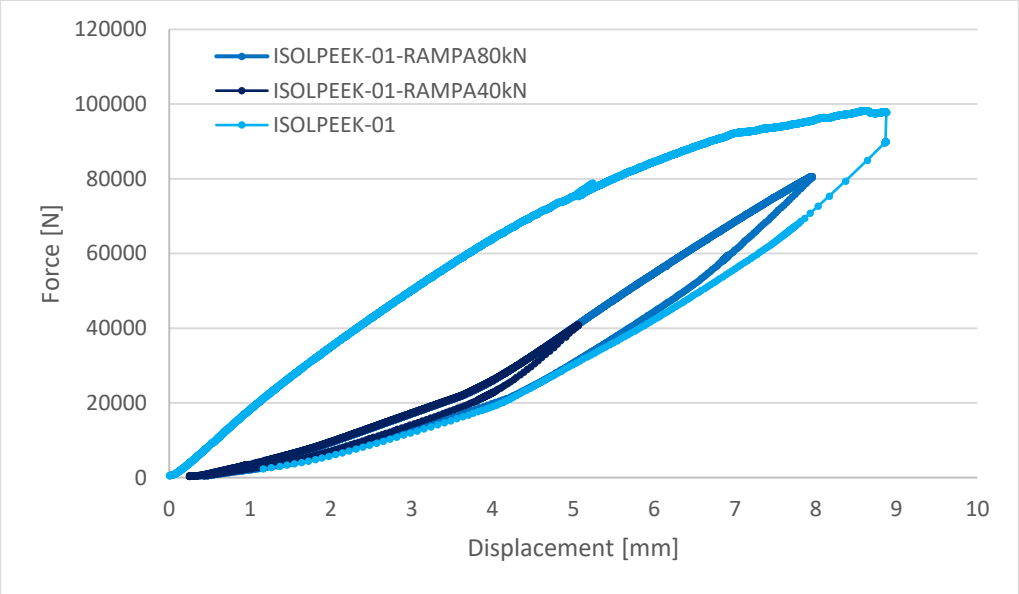

Figure 3-5: cyclic loadings of first PEEK insulator with 98, 40 and 80 kN.

The sample has been loaded with an increasing tensile force to reach the two defined successive targets of 21.1 kN and 48 kN. [41] Since the sample didn't break even at values way higher than the design threshold and due to the choice of a too high sampling rate, the test had to be temporarily interrupted before reaching the breaking point because of lack of memory availability. For this reason, a stress relaxation phase occurred between the last point of the loading curve (upper part) and the first of the unloading curve (lower part). After freeing up

memory from the storage, the sample has been unloaded to qualitatively see the amount of plastic deformation done by the material as Figure 3-5 shows.

Since loading and unloading curves do not coincide, some energy is dissipated plastically by the material. But apparently, little global permanent plastic deformation remains, because the curve tends to go back to the origin of the force-displacement graph. On the other hand, the first loading of 98 kN considerably damaged the insulator as demonstrated by the large slope difference between the first cyclic loading and those of 40 and 80 kN.

Nevertheless, the threshold values of both 21 and 48kN are largely exceeded, reaching - even with plastic behavior - values greater than 90kN. But it should be noted that a significant discontinuity appears around the displacement of 5.1 mm as shown in Figure 3-6 . In a first interpretation, this discontinuity was attributed to the fact that some of the screws lost their effective tightening function and consequently it was decided to define this value as the breaking point. Instead, as shown in the next sections, this discontinuity is more probably caused by the tensile test machine due the displacement-controlled setting. In fact, such irregularities have only been observed for the first two samples, executed both on the same date (23rd March).

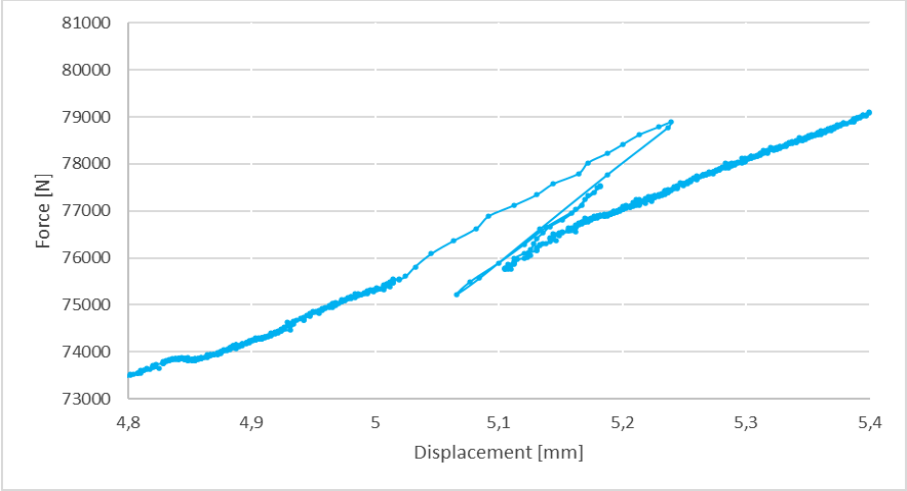

Figure 3-6: zoom in at discontinuity from the first sample loading curve.

Additionally, Figure 3-7 shows how the component's bending creates a gap between the PEEK insulator and the connected flange due to the traction force imposed by the tensile machine. Such image is used as reference for future comparison with the numerical results of the test.

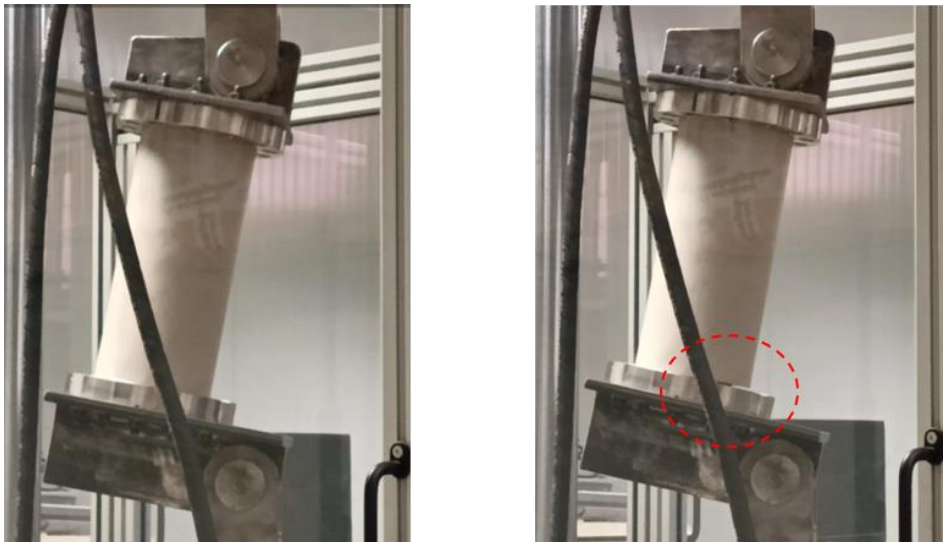

Figure 3-7: unloaded test configuration (left) and loaded test configuration (right). The red circle evidences the gap between the PEEK insulator and the flange.

3.3.3.2. Loading until fracture

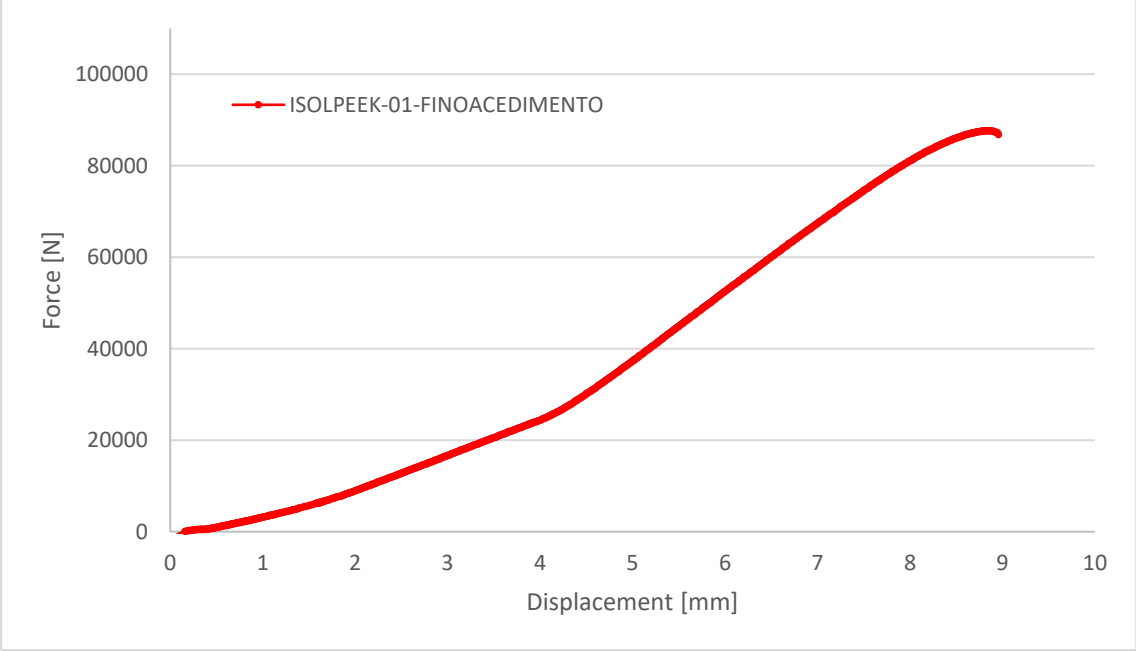

Figure 3-8: loading cycles of PEEK insulator until fracture.

It is possible to define the upper limit force value from Figure 3-8, as 87 kN. The insulator showed overall higher plasticity than expected, so that a bigger amount of energy is absorbed by the material, leading to a sudden and explosive rupture. From Figure 3-9 it is possible to visually interpret how the fracture may initiate and propagate inside the component. Two bolts out of six were stressed the most during the test, in a way that the PEEK material undergoes there a local plastic deformation until the load gets redistributed with the remaining bolts. Indeed, once redistribution occurred, the cracks propagated radially from the second pair of bolts until the remaining cross section couldn't resist the applied load, leading to a sudden and fast rupture. Therefore, even though the material reaches a 40% deformation rate, the rupture was not purely ductile. Rather the macroscopic behavior is fragile.

Figure 3-9: first PEEK insulator's fracture surface after rupture.

3.3.4. Second PEEK sample results

3.3.4.1. Cyclic loadings without fracture

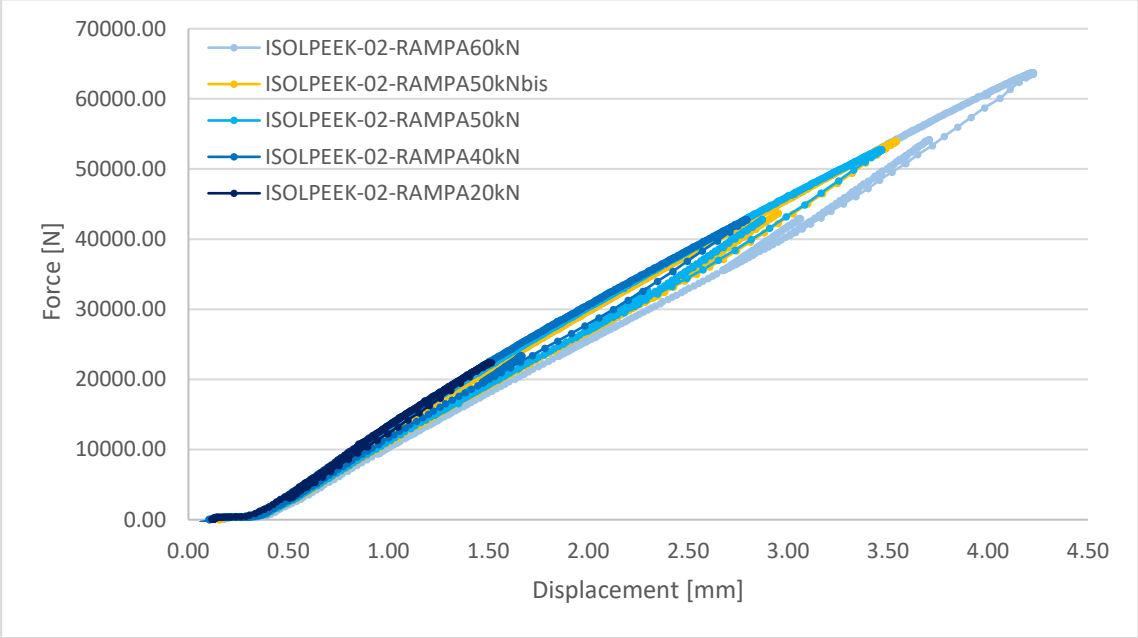

Figure 3-10: second PEEK insulator sample's cyclic loading with 20,40,50 and 60 kN.

The various cycles shown in Figure 3-10 highlight how the behavior is linear for the 20kN ramp. In fact, loading and unloading curve overwrite each other. Instead, some plastic behavior appears for all other ramps, especially for the last 60kN one. But even in this case the amount of plasticity that occurs is locally concentrated and probably located in the threaded holes of the PEEK in contact with the screw and helicoil.

It is noteworthy to state that several discontinuities are present during all unloading cycles of this sample, which are still probably caused by the tensile machine due the displacement-controlled setting. In fact, the testing of the second insulator sample occurred on the same date of the first one (23rd March), in which another of such discontinuity is present. Some examples of discontinuities are shown in the Appendix B and they all show a similar pattern, proving that the displacement-controlled setting of the machine is responsible for such irregularities.

In addition, the hysteresis behavior is clearly visible and the area between the curves generated for each loading-unloading cycle represents the energy dissipated by the material.

3.3.4.2. Loading until fracture

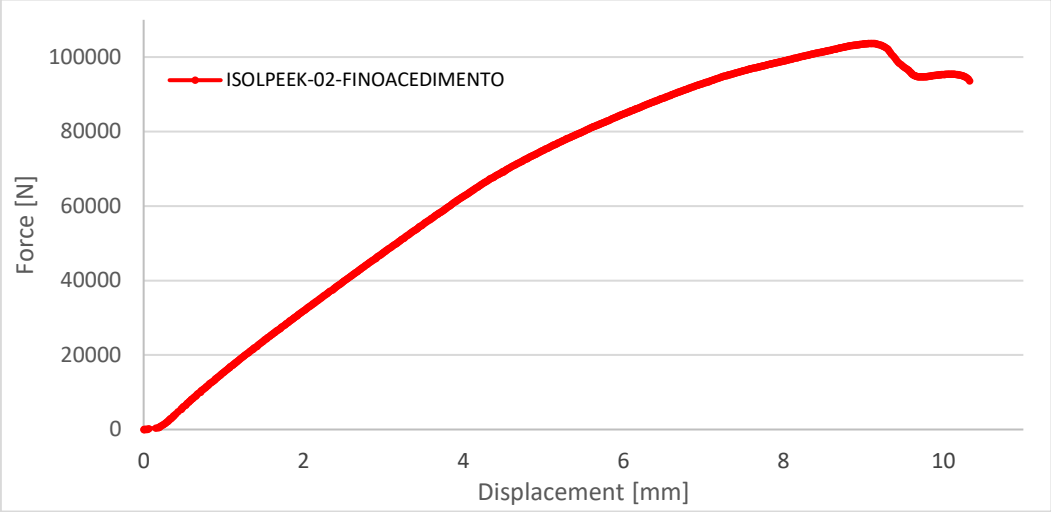

Figure 3-11: second PEEK insulator sample's loading until fracture at 94.4 kN.

The loading until fracture of the second PEEK insulator shown in Figure 3-11 occurs at a value of 94.4 kN, significantly higher than the one of the previous insulators. Evidence shows how such rupture is anticipated in this case by a nonlinear behavior where a maximum value of 103.7 kN has been reached.

3.3.5. Third PEEK samples results

3.3.5.1. Cyclic loadings without fracture

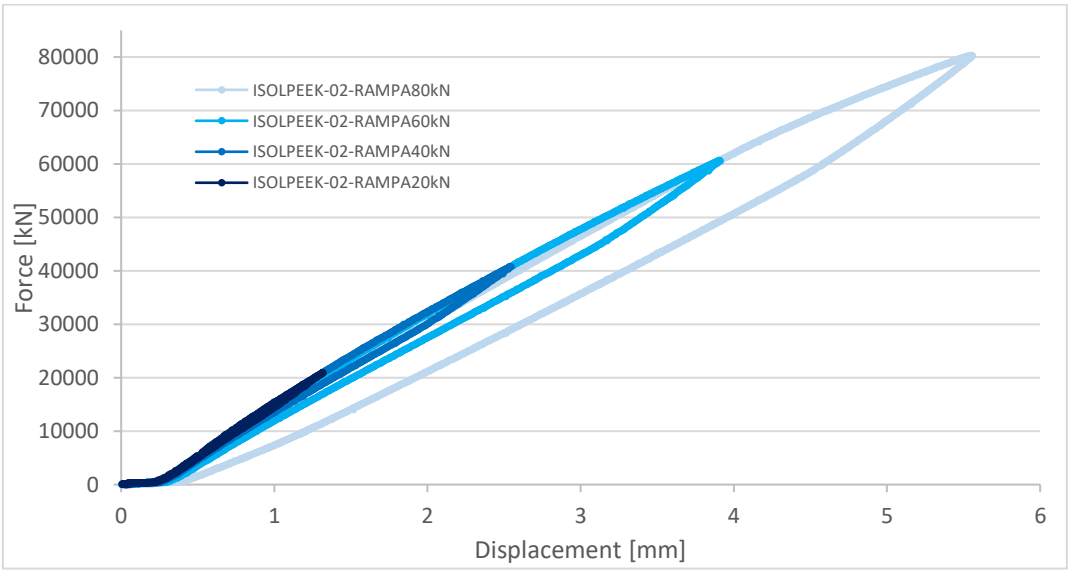

Figure 3-12: third PEEK insulator sample's cyclic loading with 20,40,60 and 80 kN.

As shown in Figure 3-12 no evident discontinuity is shown during the loading or unloading phases, suggesting that in the previous sample a systematic error from the tensile machine affected the measurements. The area underneath the 20,40,60 kN cycles are comparable with the second PEEK insulator. On the other side, the area between the loading and unloading curves for the 80 kN cycle is considerably bigger compared to the others, which means that a non-negligible percentage of global and local plastic behavior is present.

3.3.5.2. Loading until fracture

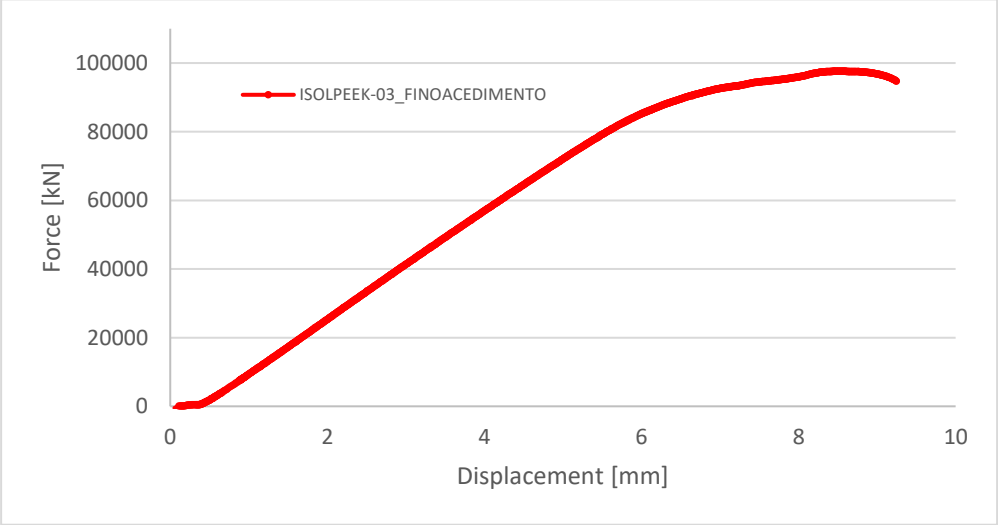

Figure 3-13: third PEEK insulator sample's loading until fracture at 93.7 kN.

The loading until fracture of the third insulator shown occurs at a value of 93.7 kN (Figure 3-13), similar value to the second insulator. No unexpected discontinuity is present.

3.3.6. Fourth PEEK samples results

3.3.6.1. Cyclic loadings without fracture

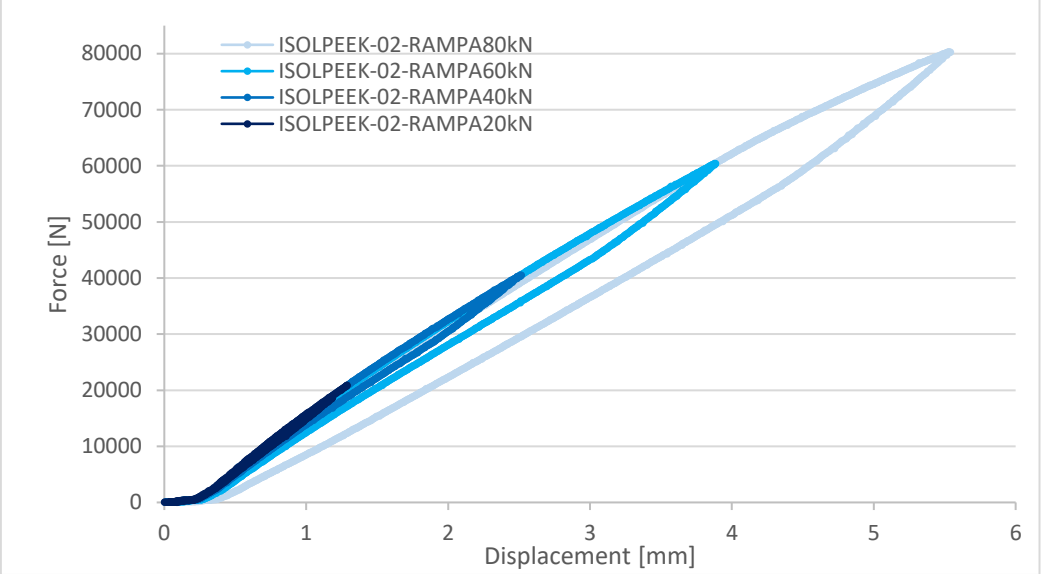

Figure 3-14: fourth PEEK insulator sample's cyclic loading with 20,40,60 and 80 kN.

As for the previous insulator, the fourth insulator has similar trends as shown in Figure 3-14. The different orientation (Figure 3-4) does not affect the stability and resistance of the insulator, which again resists the nominal stresses of 21.1 kN and 48 kN.

3.3.6.2. Loading until fracture

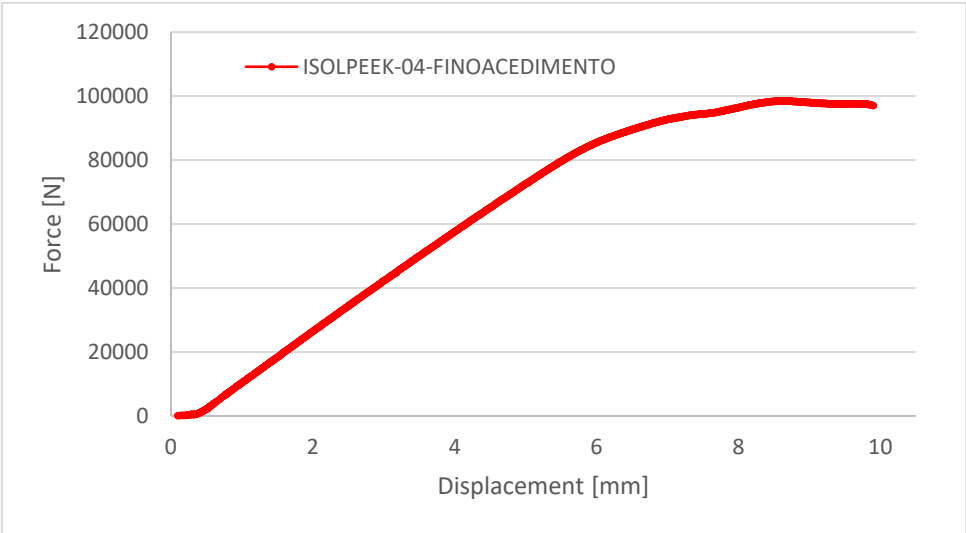

Figure 3-15: fourth PEEK insulator sample's loading until fracture at 97 kN.

The fracture of the third insulator shown in Figure 3-15 occurs at a value of 97 kN. Even at rupture there is no evidence of a different behavior due to the different orientation between insulator and flange. Instead, this orientation might even lead to a comparable or slightly greater overall resistance.

3.3.7. Results of all PEEK insulator tests

To ease the comprehension of the results, in Figure 3-16 all four tests are plotted in the same graph.

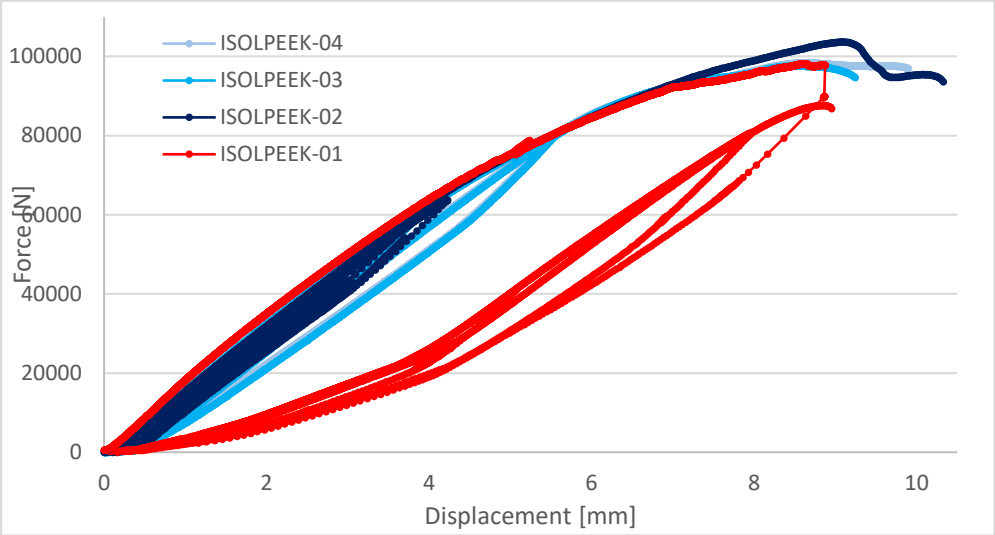

Figure 3-16: load-displacement graphs of all cycles and fractures for all four PEEK insulators.

As mentioned before, the only insulator showing different results is the first one, referred to as ISOLPEEK-01, due to a different order of loading and memory availability issues. In fact, all other insulators were previously stressed with ascending loading cycles and then stressed until fracture.

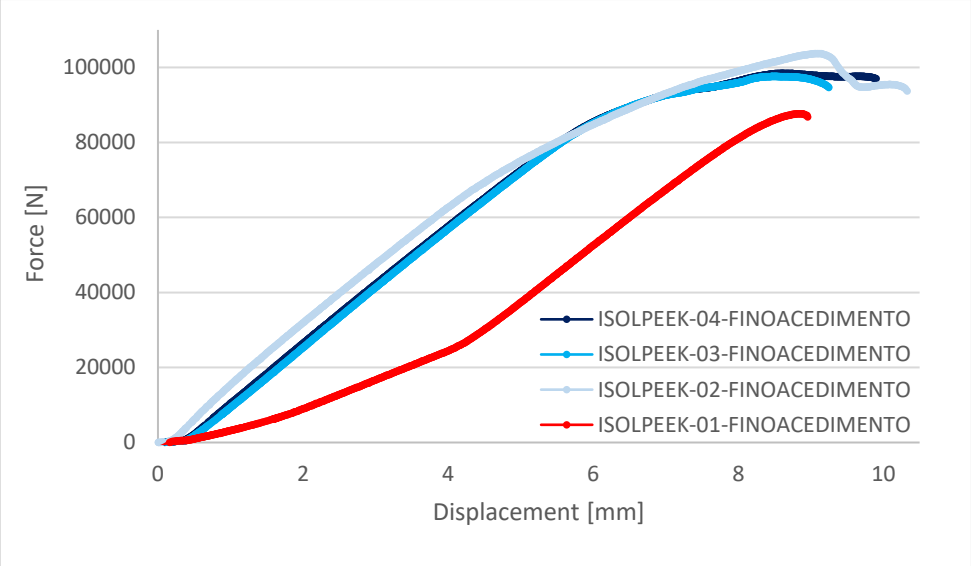

Figure 3-17: comparison of load-displacement graphs leading to fracture of all four PEEK insulators.

Instead, for the first PEEK insulator the first loading almost reached the fracture level, severely damaging the component and therefore showing a weaker trend. Hence, by considering the second to fourth insulator the results are similar for both lower loading cycles and fracture as shown in Figure 3-17.

3.4. Comparison of test results vs. expected operational loads: verification criteria

As shown in Table 2, during operation the insulators numbered as 2 and 3 are expected to be the most loaded: the insulator 2 undergoes the largest tensile force while the insulator 3 is almost loaded in pure shear and undergoes the largest shear force [41]. The results of the mechanical tests show that the PEEK post insulator design satisfies with a large margin the criteria defined [41] corresponding to the nominal loading on those two insulators. It withstands the 21.1 kN and 48 kN targets. Only around 87 kN failure is detected. However, to be conservative the worst-case scenario is chosen as reference. By doing so, the first PEEK sample is chosen as reference showing a discontinuity at 75.5 kN, even if it is probably caused by the setting of the control system of the tensile test machine, as indicated by the engineers responsible for the operation of the machine.

Figure 3-18 and Figure 3-19 compare the shear and tensile loads reached during the test with the loads foreseen on the single insulators mounted on the Mock-Up electrodes, including a 100% penalty factor.

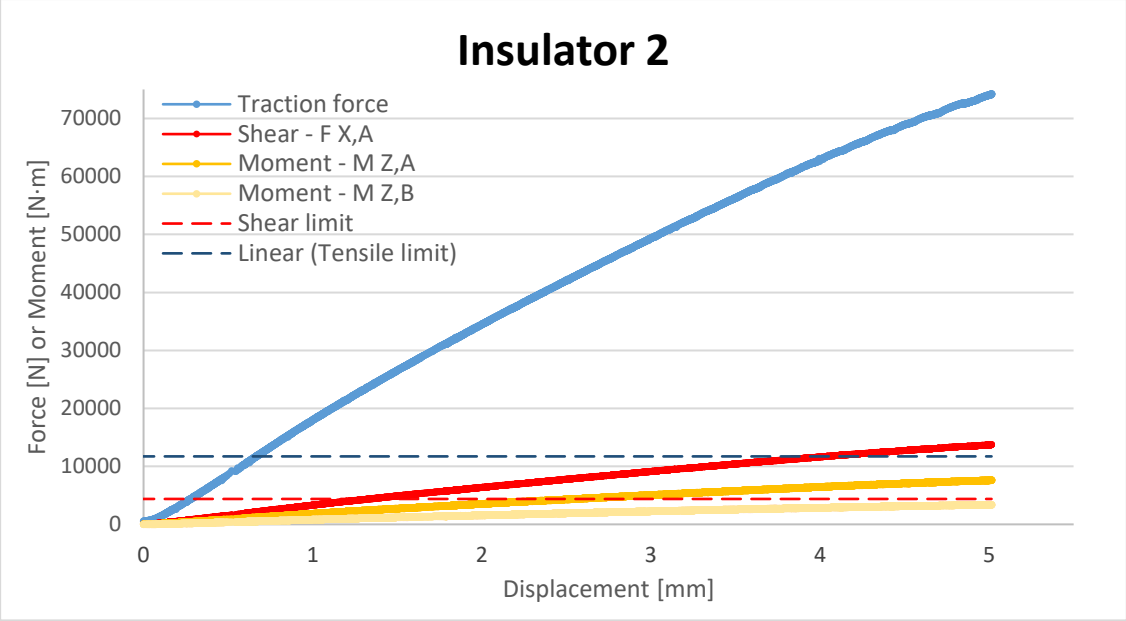

Figure 3-18: comparison between experimental and target loads for insulator 2.

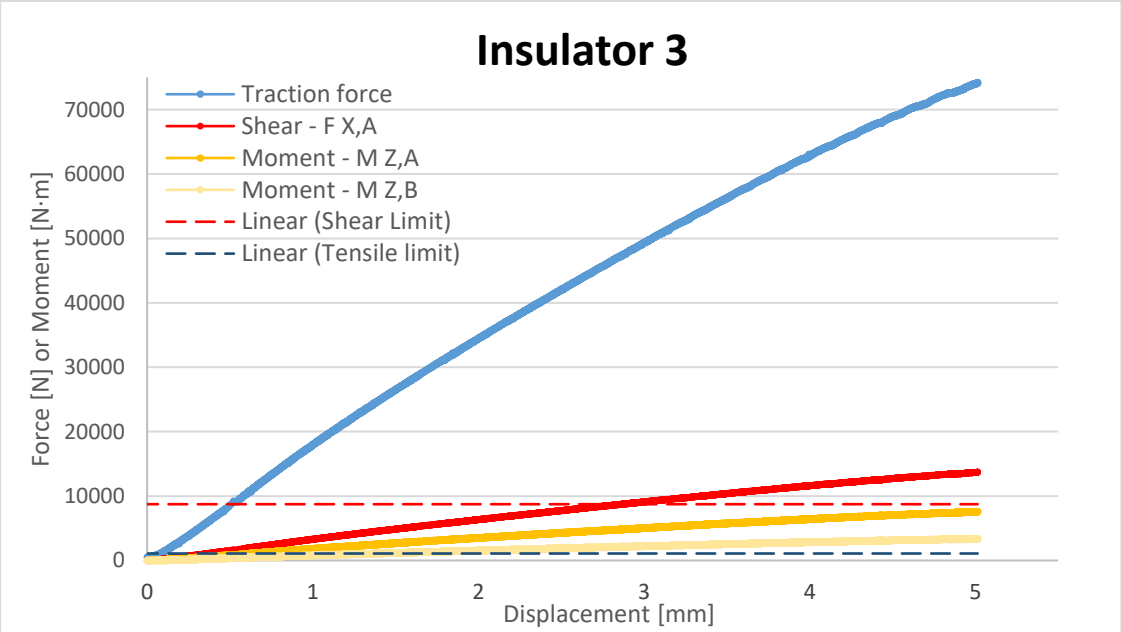

Figure 3-19: comparison between experimental and target loads for insulator 3.

The value of 75.5 kN can be taken as as the upper limit of the mechanical loads (being the worst value out of 4 tested PEEK insulators) admissible by the PEEK insulator. This tensile force on the test setup corresponds to the following set of forces and moments:

	$F_{X,A}$	$F_{Y,A}$	$M_{Z,A}$	$M_{Z,B}$
	N	N	N·m	N·m
Max. admissible traction force	75500			
Corresponding max. admissible loads	13741	74217	7626	3398

Table 10: admissible loads obtained by the experiments.

Table 11 summarizes the results of the experimental campaign: two limits are defined from the experimental results:

- the tensile force at which the insulators break;
- the tensile force at which the insulator behavior is not elastic anymore, characterized by a change in slope of the force-displacement curve corresponding to a tensile force around 60 kN, as visible in Figure 3-16.

The first table displays the forces and moments (calculated analytically from equation Eq I) of all 4 insulators at their breaking point. Instead, the second table displays the forces and moments (calculated analytically from equation Eq I) for which the tensile force reaches 60 kN, not considering the first insulator due to its different loading cycles (repeatability criteria isn't satisfied).

In both tables, an average value is calculated for each component of the loads, and compared to the load components on the most loaded insulators. [41] This allows to calculate the margin factors for breaking and for plasticity.

FRACTURE

	~~*first*~~	second	third	fourth	**average**
Max $F_{X,A}$ [N]	~~*15956*~~	18879	17767	17920	18189
Max $F_{Y,A}$ [N]	~~*86182*~~	101966	95959	96790	98238
Max $M_{Z,A}$ [N·m]	~~*8855*~~	10477	9859	9945	10094
Max $M_{Z,B}$ [N·m]	~~*3945*~~	4668	4393	4431	4497

MARGIN FACTORS

Ins.**2** loads	Ins.**3** loads	$\varepsilon_{Ins.2}$	$\varepsilon_{Ins.3}$	ε_{min}
4392	8754	4.14	2.08	**2.08**
11719	1082	8.38	90.79	
1163	1870	8.68	5.40	
244	878	18.43	5.12	

	RAMP60kN - PLASTICITY				
	~~first~~	second	third	fourth	**average**
Max $F_{X,A}$ [N]	≠	11606	11034	10993	11211
Max $F_{Y,A}$ [N]	≠	62688	59595	59375	60552
Max $M_{Z,A}$ [N·m]	≠	6441	6123	6101	6222
Max $M_{Z,B}$ [N·m]	≠	2870	2728	2718	2772

		MARGIN FACTORS		
Ins.**2** loads	Ins.**3** loads	$\varepsilon_{Ins.2}$	$\varepsilon_{Ins.3}$	ε_{min}
4392	8754	2.55	1.28	**1.28**
11719	1082	5.17	55.96	
1163	1870	5.35	3.33	
244	878	11.36	3.16	

Table 11: additional margin factors for fracture and 60kN ramp loadings without considering the first PEEK sample due to its different order of loading cycles and with consistent frames [41].

Although the number of samples is small, the amount of stress the PEEK insulator managed to resist is significantly greater that the nominal forces and the cyclic loadings of the second, third and fourth samples display no global plastic behavior if operated at nominal conditions. The target of 48 kN is reached with a significant margin, which means that no additional pure shear test is required to validate the insulator design.

Therefore, it can be stated that **the PEEk insulators can withstand the foreseen static loads of the MITICA BS Mock-up accelerator structure with a large margin,** being ε_{min}=2.1 for breaking and ε_{min}=1.3 for plasticity, added to the ×2 safety factor already present [41]. Moreover, the tensile tests provide lower bounds for the admissible load components on the insulators, displayed in Table 10.

After the validation of the PEEK insulator's mechanical requirements, the construction of the MITICA Mock-p has been initiated to start by the end of the year with the electrical insulation test. Some images of the prototype is shown in Figure 3-20. Finally, the raw data of the tests are displayed in Appendix A. It is noteworthy to state that some discontinuities are observed in the load-displacement curves, as listed in Appendix B.

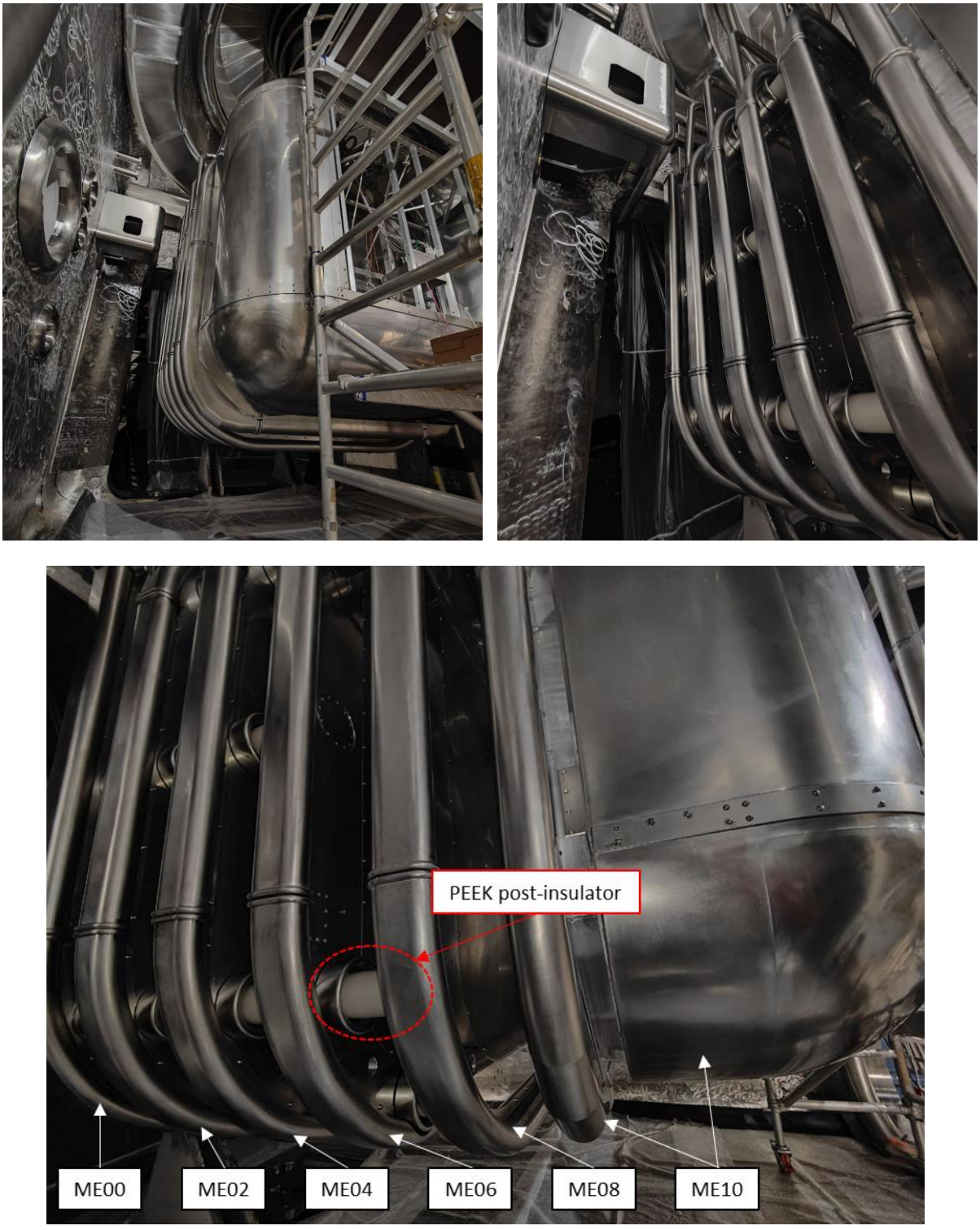

Figure 3-20: assembly of MITICA Mock-Up Beam Source with all electrodes ME00-ME10 without the electrostatic shield ES06 inside the vacuum chamber.

3.5. Comparison with previously tested alumina insulators

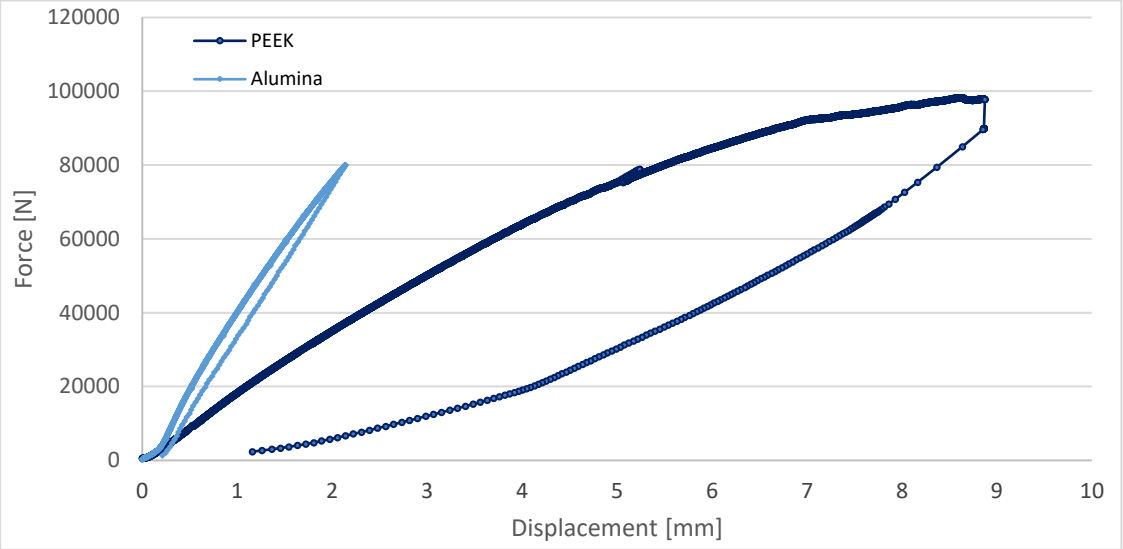

Figure 3-21: example of insulator loading case compared to first PEEK insulator in Figure 3-5.

For immediate understanding, the comparison of Figure 3-21 between the loading case of PEEK and alumina post-insulator gives a brief idea of differences and similarities between the mechanical properties of the two materials:

- Both alumina and PEEK show high resistance to the applied loads;
- PEEK insulators are subjected to bigger displacement with the same load;
- PEEK insulators show a less linear behavior compared to alumina insulators, hence having higher share of plasticity;
- PEEK insulators are more ductile;
- Higher hysteresis is shown for PEEK than for Alumina insulators.

4. Introduction to structural analysis by “Finite Element Method”

For ease of understanding, a brief description of the “Finite Element Method” also called “Finite Element Analysis” follows, with an insight on three of the ANSYS 2022 R2 analysis options named “Static Structural”, “Explicit Dynamics” and “Modal Analysis”.

The major settings and details are recalled together with the presentation of the numerical models. However, these paragraphs can be useful in case similar numerical models need to be established due to the presence of settings details description.

4.1. Finite Element Method (FEM) [48,49]

The finite element method is defined as a numerical technique suitable for finding approximate solutions to problems described by partial differential equations (PDEs). The approximated solution is found by reducing PDEs into a system of algebraic equations, making it possible to avoid solving the complex starting PDEs, which is not always possible.

This method is based on the division of the domain of interest (2D or 3D) into a finite number of subdomains, called "elements," for which approximate solutions is found using interpolating functions. In turn, “elements” are defined in the terms of the field of variables at specific points called "nodes," which connect the elements and are usually part of its boundary.

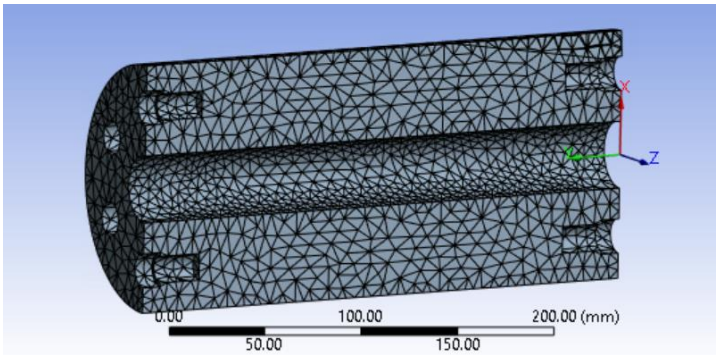

Figure 4-1: example of subdivision of a volume of a 3D object (domain) into smaller volume “elements” (subdomains) where one the vertices represent “nodes”.

Therefore, the ability to discretize a continuous domain with a finite number of elements makes the method useful for problem solving in multiple engineering disciplines. It allows the transformation of an engineering problem into its mathematical representation where the “node” is the fundamental identity of finite element theory.

Each node is characterized by 6 degrees of freedom, 3 translational and 3 rotational. Therefore, it defines spatial coordinates with respect to a defined coordinate frame, where the degrees of freedom and actions/effects of the physical problem are well defined. It is never considered individually, and it is connected to other nodes, creating elements of different geometries. Typically, the finite element defines a volume of space, being part of a set of contiguous finite elements that, then, form together the so-called "mesh".

The elements can be one-dimensional (line), two-dimensional (area) or three-dimensional (volume). For example, the most common three-dimensional ones are tetrahedral, right prism and regular hexahedron.

As mentioned before, interpolating functions are defined on the basis of the values at the nodes, and their order determines the order of the finite element. Usually, finite elements are of the first or second order.

In the first case, nodes are present on the vertices of the finite element. If it is subjected to a “real” displacement, it will have a linear “calculated” displacement equal to the difference in displacements between the various nodes and a constant strain and stress instead, the latter being the derivatives of the “calculated” displacement. In this case, since the derivative of the “calculated” displacement is continuous (formed as a broken line, with segments of varying slope), the strain and stress show a discontinuity.

Instead, in the second case, there are nodes also at the midpoint of each side of the finite element. Therefore, higher order elements possess more nodes. This time, the “calculated” displacement is obtained by a quadratic law, so that both strain and stress show now linear behavior.

By comparing these two groups of finite elements, the second order element reveals more accurate results than the first order one. However, higher order elements have higher order interpolating functions and higher number of nodes, requiring greater computational resources for the approximated solutions to be found. Therefore, the choice of using a precise order of finite elements is not trivial and requires a trade-off between results’ accuracy and computational resources.

In essence, the steps of the finite element method can be summarised as:

- the discretization of the domain into a finite number of subdomains, called elements;
- the choice of interpolating functions;
- the development of the element matrices;
- union of the element matrix parts for each subdomain to obtain the global matrix of the entire domain;
- imposition of boundary conditions;
- resolutions of equations.

There are many approaches to construct an approximate solution based on the concept of the finite element method. The 3 main ones are the direct approach, the weighted residuals method and the variational approach.

The former is used for simple one-dimensional problems. The weighted residuals method, on the other hand, is used in cases where functions cannot be constructed and, therefore, differential equations are used directly, such as those in heat transport or fluid mechanics. Finally, the variational approach is based on calculating variations involving the extreme points (maxima and minima) of so-called “functionals”, which are functions whose domain is itself a set of functions.

In matrix form the global system of equations can be written as:

$$\boldsymbol{K_G} \cdot u = F$$

Where $\boldsymbol{K_G}$ is the global stiffness matrix (considers all interactions between all nodes of the model), u is the vector of unknowns (representing the spatial variables of all nodes of the domain), and F is the force vector (acting as boundary condition to the nodes).

Besides the theory behind FEM, thanks to the Graphical User Interface (GUI), a typical simulation consists on the following steps:

- Defining the engineering data (materials and their properties);
- Sketching the geometry;
- setting up the model: element shape and size (mesh) and boundary conditions (constraints, interactions and applied loads);
- run the model to let the “solver” solve the model set-up;
- retrieve the results of interest and examine the details of the response.

4.2. ANSYS Static Structural Analysis

4.2.1. Overview

The “Static Structural” Analysis is used to determine displacements, stresses, strains etc. under static loading conditions. The primary unknowns (nodal degrees of freedom) are displacements, while other quantities are derived from nodal displacements such as strains, stresses and reaction forces. The assumptions of such analysis are:

1- inertial loads are neglected;
2- linear material response: Hooke's law is used, neglecting hysteresis and plasticization if not diversely specified;
3- small displacements: deformation is calculated with respect to the starting undeformed structure, instead of calculating a progressive deformation of the body, which would result in a change in stiffness and direction of load application.

Since the thesis focuses on three-dimensional engineering problems, the modelling of continuous structures usually requires three-dimensional models with solid elements, whose analysis will allow for the greatest degree of detail at the expense of greater computational costs. However, as shown later, it is always of good practice to idealize 3D problems to a two-dimensional analysis whenever possible, using plane stress, plane strain or axial symmetry.

In addition, non-linear material responses can also be modelled, but require additional material properties inputs to allow reliable results. Nonlinearity can include plasticity, stress stiffening, large deflection, large strain, hyper elasticity etc.

4.2.2. Mesh

In every model, obtaining a good mesh is critical to achieve reliable results of the simulation at a reasonable computational cost. There are many ways to fulfil this goal as there is no single procedure to follow. In the next models, the following steps help reaching good meshing:

- The first simulation is run with a coarse mesh to see if other types of errors prevent the solution to converge and to understand which parts require more attention, hence more elements;
- The overall “Element Order” option is generally left “Program Controlled”;
- The “Element Size” option is generally left to “default”;
- “Body sizing”, “Surface sizing” or “Edge sizing” functions are used to impose an “element size” to a precise body, surface or edge to achieve at least the presence of 2 connecting elements in the geometry’s smallest dimension;
- “Contact sizing” function is used to map meshes belonging to different body in contacts to assure continuous results (not mapped meshes lead to jumps in displacements and unreliable results);

- Bodies showing parts with little geometrical complexity are divided to separately mesh them, assuring a better mesh quality;
- If not extremely necessary, it is common practice to simplify the geometry of the model compared to the real one, neglecting small geometric details if possible, therefore easing the meshing process and reducing the computational cost of the simulation.

4.2.3. Boundary conditions

The type of boundary conditions of concern are mainly: contacts, forces, bolt pretensions, remote displacements, displacements, fixed support, cylindrical support.

For simplified models, the contact setting used is generally “bonded”. It is a default setting in which no sliding or separation between the involved faces or edges is allowed. This type of contact is particularly used for a linear solution since the contact length/area will not change during the application of loads. However, for more realistic representation, “frictional” contact is preferred. In this configuration, two contacting geometries can carry shear stresses up to a certain magnitude across their interface before sliding relative to each other. It is common practice to use a “friction coefficient” of 0.2.

Moreover, “bolt pretension” simulates the tightening of bolts, typical of an assembly involving screws and bolts. This condition is applied to the shank of the screw in two-time steps: one in which the tightening force is applied to the screw and one in which its degrees of freedom are locked.

4.2.4. Analysis settings

For the analysis setting only the “Step control” is varied form the proposed default settings. The “number of steps” to evaluate the results for many different loading conditions in the same simulation. For example, with 2 load steps, the bolt pretension is assigned at step 1, instead the main loading condition of the structure is assigned at step 2. In this way a more realistic loading of the structure is simulated.

4.2.5. Output controls

For Post-processing of the simulation the solution output used are generally: total deformation, directional deformation, equivalent stress. In the solution information, the convergence of forces, moments and deformation is visible to detect the convergence of the numerical model.

4.3. ANSYS Explicit Dynamics Analysis [50]

4.3.1. Overview

ANSYS Explicit Dynamics can perform, among others, the modelling of nonlinear dynamic behavior of solids, fluids, gases and their interaction. It is generally used to determine the dynamic response of a structure due to stress wave propagation, impact or rapidly changing time-dependent loads. Mechanical events with fairly short time scales (of the order of fractions of milliseconds) can be efficiently simulated with this type of analysis.

However, this type of analysis can be used to model mechanical phenomena that are highly nonlinear. It can contain both rigid and flexible bodies. For rigid/flexible body dynamic simulations involving mechanisms and joints, you may wish to consider using either the "Transient Structural Analysis" or "Rigid Dynamics Analysis" options.

This type of analysis is constrained to maintain stability and consistency via the "Courant-Friedrichs-Lewi condition". In this way a shock wave cannot propagate a distance longer than the minimum characteristic length in one cycle [50].

$$\Delta t \leq f \times \left(\frac{h}{c}\right)_{min}$$

Where f stands for the stability timestep factor (usually equal to 0,9), h stands for the "characteristic length", being the volume of the element divided by the square of the longest diagonal of the zone and scaled by $\sqrt{2/3}$, and c stands for the local material sound speed in a element (dependent on the material's density, elasticity and other properties).

Additional useful notes are:

- In the output controls the "result number of points" will become frames in the post-processing animation.
- Analysis setting → Step Controls → Resume from cycle useful to extend an analysis that has reached its end time (without doing again the whole simulation).

4.3.2. Mesh

A smooth uniform mesh should be sought in the regions of interest for the analysis, using the "Explicit" meshing preference (set by default) to auto-assign the default mesh controls that will provide a mesh well suited for Explicit Dynamics analyses. A coarse mesh can often be used to gain insight into the basic dynamics of a system while a finer mesh is required to investigate nonlinear material effects and failure.

Always set the "Element order" to "Linear" (should be a default).

Look at the max and min element size statistics because the run times are directly connected to the characteristic length through the time step (CFL condition). A very useful mesh metric is the “Characteristic Length”: it is primarily used to determine the timestep for an element. Swept/multi-zone meshes are preferred in Explicit Dynamics analyses so geometry slicing, combined with multibody part options in “DesignModeler”, are recommended to facilitate hexahedral meshing.

4.3.3. Boundary conditions

It is important to know that displacement and rotation boundary conditions must be ramped: they cannot have non-zero values at time 0. Moreover, loads must be applied in a single step.

4.3.4. Analysis settings

The required input for “step control” is the termination time for the analysis: “End Time”. It represents the maximum length of time to be simulated by explicit analysis. The best estimate of the solution time required to simulate the event being modelled can be based on the CFL condition.

The governing factor for the timestep value is the smallest mesh element size and its mass. The timestep is calculated based on sound speed (which depends on density and material properties) and it needs to have a small enough value to accurately simulate the stress waves traveling through the body.

The “Erosion controls” are used to automatically remove highly distorted elements from an analysis. The default setting will erode elements which experience geometric strains more than 150% (1.5 as parameter). The eroded nodes are displayed as red dots.

4.3.5. Output controls

There are three types of output controls for saving results, restart points, and results tracker data. The “Result Number of Points” controls how the visualization of the chosen solution tools will look. This determines how many and how frequent the evaluation points will be. These will later become frames in the post-processing animation. Having a lot of points that are tightly packed will increase the total solution run time.

The “Restart Number of Points” are useful when the simulated model goes through complex actions and it is important for you to be able to rerun the simulation from a certain point.

The “Result Trackers” save very specific information from small, localized areas and are important for monitoring places of interest.

4.3.6. When implicit models are suitable for explicit models

There is an overlap in the "Quasi-Static" application area, where both Implicit and Explicit methods can be used to solve a model. An implicit model like the one used in a Static structural might require the usage of an explicit model in case of:

- Large deformations (rubber like highly deformable materials);
- Large contact models (especially when the contact is not bonded, but sliding and moving);
- Rigid body deformations (rigid body snaps over a soft and flexible one).

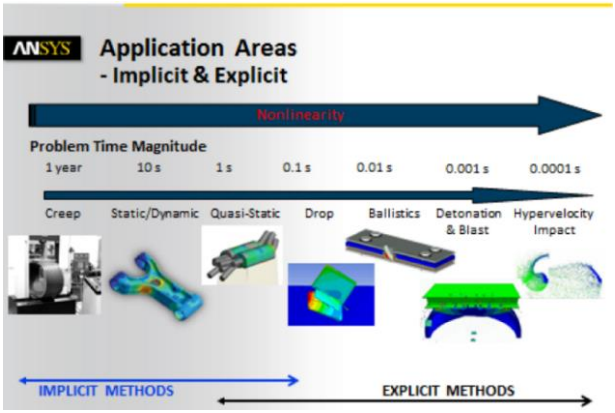

Figure 4-2: application areas of explicit methods for nonlinear problems.

4.3.7. Drag and drop geometry or model

In general, it is of good practice to avoid model connection between an implicit and an explicit solver because, generally, with a complex geometry different mesh are used for the two solvers.

If the model is dropped, then, performing an implicit static structural or transient structural analysis to an Explicit Dynamics analysis requires the same mesh for both the implicit and explicit analysis and only low order elements are allowed.

4.3.8. Applying pre-stress effects on Explicit Dynamics

Applying pre-stress effects on Explicit Dynamics simulation is effective for cases in which a generally slower (or rate-independent) phenomenon is followed by a much faster event.
It is possible to specify the transfer of either displacements only or the more complete Material State (displacements, velocities, stresses, and strains), from a static or transient structural analysis to an Explicit Dynamics analysis.

It is only applicable to 3D simulations.

The same mesh is required for both Implicit and Explicit analysis and only low order elements are allowed. If high order elements are used, the solve will be blocked and an error message will be issued.

4.4. ANSYS Modal Analysis [51,52]

4.4.1. Overview

Modal Analysis is the most basic and fundamental linear dynamics analysis, with the aim to identify the natural frequencies and mode shapes of a structure or machine component. These represents the vibration characteristics of a structure and give immediate information about concerns for its integrity.

This type of analysis is performed to avoid, for example, resonant vibration. Unpredictable seismic activity could represent a potential danger for the structure's survival due to the resonant transmission of energy. If the natural frequency of the earthquake is close to the structure's one, there is the maximal efficiency in energy transfer and, consequently, the biggest damage for the structure. Such concern is present for bigger assemblies as for the MITICA Beam Source and its Mock-Up.

For solving the dynamic response of a structure, the basic equation to refer to is the "general equation of motion":

$$[M]\{\ddot{q}(t)\} + [C]\{\dot{q}(t)\} + [K]\{q(t)\} = \{F(t)\}$$

The unknows are acceleration $\ddot{q}(t)$, velocity $\dot{q}(t)$, and displacement $q(t)$ for all points of the structure. Whereas $[M]$ is the mass matrix, $[C]$ is the damping matrix, $[K]$ is the stiffness matrix and $F(t)$ is the load vector. However, since the natural frequencies and mode shapes are load-independent, in linear Modal Analysis the external loads are set to 0. Additionally, for simplifying the resolution of the system of equation, the damping effects are ignored, yielding:

$$[M]\{\ddot{q}(t)\} + [K]\{q(t)\} = \{0\}$$

To find natural frequencies, it is necessary to chance form a time domain to a frequency domain, and to do so, one can assume harmonic motion in all "i" points of the structure:

$$x_i = A_i sin(\omega_i t + \varphi_i)$$

Every point's motion is expressed through an amplitude A_i, a frequency ω_i and a phase angle φ_i allowing to describe the acceleration through double derivation of the harmonic motion:

$$\ddot{x}_i = -\omega^2 A_i sin(\omega_i t + \varphi_i)$$

Combining the previous three equations, with $\Phi_i = A_i sin(\omega_i t + \varphi_i)$, t and assuming that geometry, mass distribution and material properties of the structure are known, the problem is well established and can be solved:

$$([M] - {\omega_i}^2[K])\,\Phi_i = \{0\}$$

The first part in brackets allows to determine the natural frequencies of the structure ($f = \omega/2\pi$), instead the second part allows to evaluate the different shape modes.

In other words, the mode frequencies and shapes depend on the mass and stiffness distribution within the structure:

$$\omega = \sqrt{\frac{K}{M}}$$

Nonetheless, most of the structures find themselves in a prestressed condition during normal operation such as cantilevered structures. When a structure is in a stress state, its stiffness changes due to stress-stiffening, such that tensile stresses tend to increase the natural frequencies, while compressive stresses tend to decrease them as it is possible to see from the updated set of equations:

$$\omega = \sqrt{\frac{K+S}{M}} \qquad ([M+S] - \omega_i{}^2[K])\,\Phi_i = \{0\}$$

Where $[S]$ stands for the stress stiffness matrix. This stress induced stiffness change can be modelled as well in a Modal Analysis, adding a prestress condition.

4.4.2. Mesh

The same guidelines as for ANSYS Static Structural can be used. Nevertheless, since this type of simulation is particularly time consuming, it is better to use a coarser mesh compared to static structural analysis, unless extremely necessary. Besides, it is not needed to refine the mesh at small geometries such as holes and pins, since such details have no contribution to the determination of the modes. The geometry can be modified to suppress such details, allowing for a cleaner and coarser mesh.

4.4.3. Boundary conditions

Only linear behavior is valid in modal analysis, thus any non-linearities, such as plasticity and contact (gap) elements, are ignored even if specified. All contacts are automatically set to bonded.

4.4.4. Analysis settings and post-processing

The two main options are “Max Modes to Find” and “Limit Search to Range”. The former sets a maximum value of mode shapes to be found, because the number of natural frequencies and shapes depend on the degree of freedom of a structure. A typical three-dimensional continuous body has theoretically infinite degrees of freedom, requiring an upper limit for the simulation. The latter specifies a range of frequency in between which searching for the natural frequencies

and shapes. This setting is useful, for example, to see if resonant vibration is at risk in a precise range of interest, which could be the one typical of seismic activity of a particular region.

Yet, not all the frequencies have the same importance. Some of them move more mass along precise directions compared to others. Both “Mode Participation Factor” and “Effective Mass” are parameters that measure the amount of mass moving along one direction for each mode. High mode values for a precise direction indicate that such modes is excited by excitations in such directions.

The mode participation factor is calculated as follows:

$$\gamma_i = \{\Phi\}_i^T [M]\{D\}$$

Where $\{\Phi\}_i^T$ represents the transverse matrix of the mode shapes, $[M]$ the mass matrix and $\{D\}$ the excitation vector assumed to be a unit displacement vector depending on the direction of excitation in each of the “Global Cartesian directions” and rotation about each of these axes.

The “Effective Mass” parameter is directly linked to the Participation Factor and the higher its value, the more dominant is the natural frequency found:

$$M_{eff,i} = {\gamma_i}^2$$

Additionally, also the “ratio of Effective Mass to Total Mass” is another important indicator. Besides showing the dominance of a natural frequency in a precise direction, it also gives further information. If the cumulative sum of all the effective masses in one precise direction is close to the total mass, then it is highly likely that most of the natural frequency of the structure are found.

However, it is important to keep in mind that for structures showing “fixed supports” as boundary conditions, The effective to total mass ratio remains far lower than 1. The reason why is that the material near the “fixed supports” will not move, hence showing lower “Effective Mass”.

5. 2D Explicit Dynamics model for PEEK fracture explanation

5.1. Objective

The manual and visual inspection of the broken samples of PEEK insulators indicate that the fracture starts from the threads connecting the M14 helicoil with the insulator, as shown in Figure 5-1.

An explicit Dynamics model is used to test this hypothesis and determine which part of the PEEK insulator can be considered as the starting point of the final fracture of the component.

Figure 5-1: mechanical breakdown of PEEK post-insulator sample 2 (left), 3 (middle) and 4 (right).

5.2. Geometry and mesh

The model's geometry makes use of 2D axial symmetry to reduce needed computational effort resources. This assumption is not completely representative of the real case scenario due to the presence of the spiral shape of the screw's thread. However, it can be considered reasonable for a first approximate insight.

As shown in Figure 5-2, the screw, helicoil and PEEK insulator interaction is modelled using a greater number of elements on the PEEK bulk material, allowing better solution quality of the total deformation caused to the PEEK thread. The element size is set to 0.5 mm with face sizing of 0.25 mm for helicoil faces and PEEK bulk material.

Additionally, a hex dominant mesh method is defined to assure quadrilateral elements, preferred for an Explicit Dynamics simulation. The mesh statistics are 12846 nodes and 12381 elements.

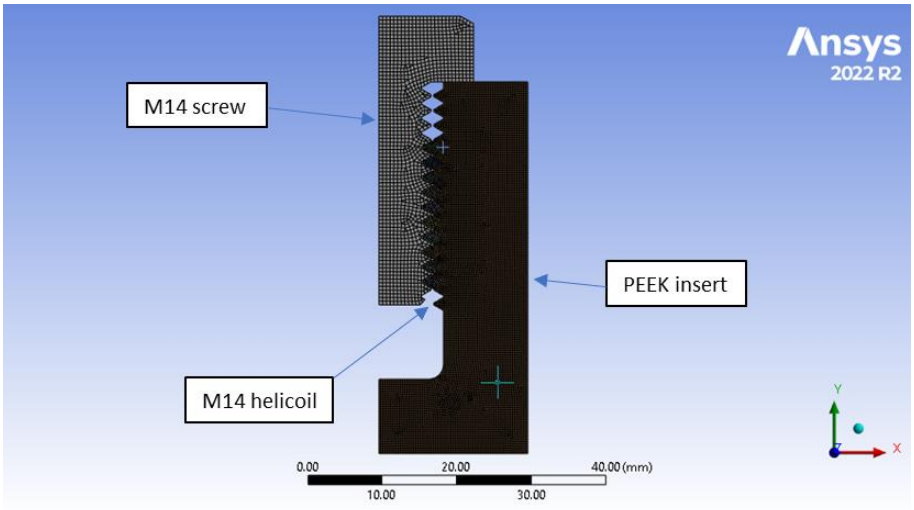

Figure 5-2: geometry and mesh of 2D explicit dynamics modelling of M14 screws, helicoil and PEEK interaction.

5.3. Boundary conditions

The contacts between all faces in contact must be specified. All contacts are set to frictional to allow sliding between faces, with friction coefficient of 0.2. As an example, the contact between one thread of the helicoil and the PEEK bulk material is shown in Figure 5-3. The same contact settings are used for all connections between:

- the M14 screw with the M14 helicoil;
- the M14 helicoil with the PEEK bulk material;
- the M14 screw head with the PEEK material.

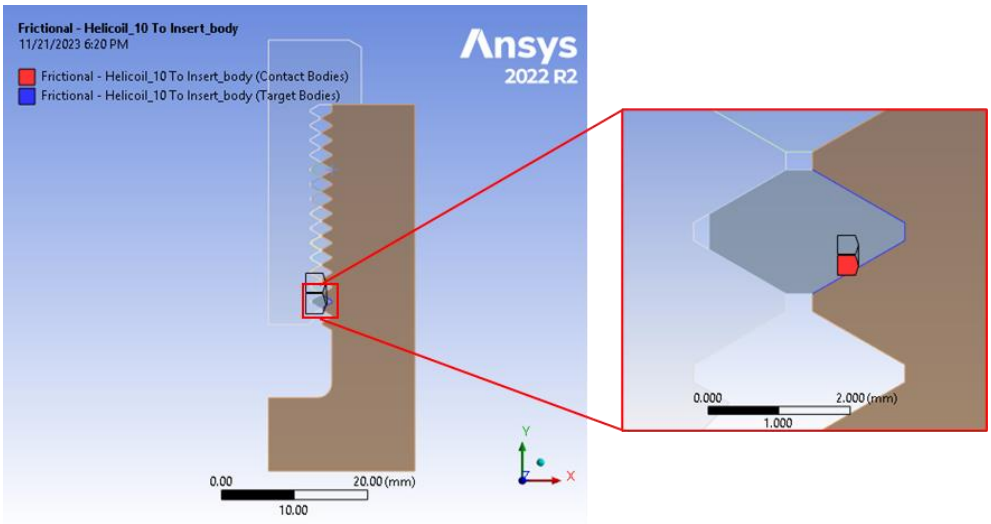

Figure 5-3: frictional contact type between helicoil and PEEK bulk material of 2D explicit dynamics.

As shown in Figure 5-4, the constraints imposed are fixed supports of the external edges of the PEEK bulk material to reproduce the presence of additional PEEK material in radial and vertical direction. Moreover, a remote displacement of 4 mm in positive y direction is defined to cause at least rupture of some part of the thread of the PEEK bulk material.

Lastly, the end time of the analysis settings is set to 0.001 s to contain the runtime of the simulation to a few minutes.

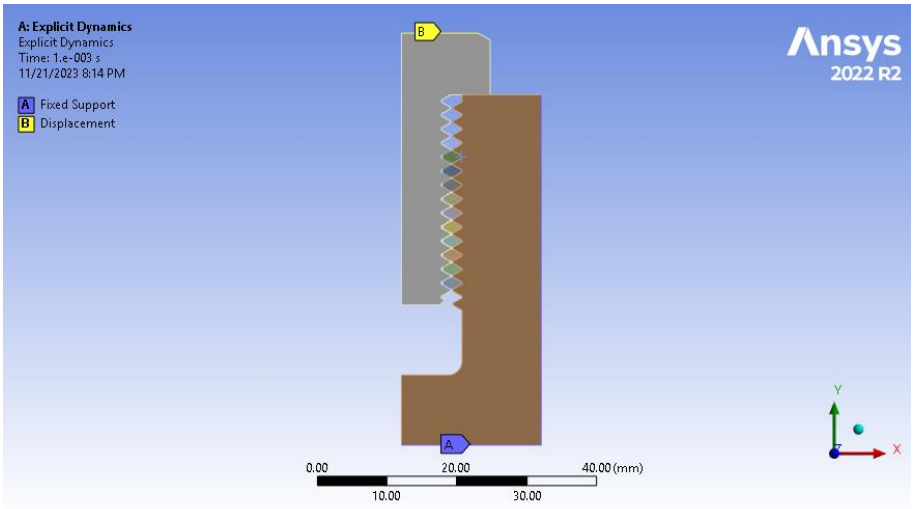

Figure 5-4: boundary conditions for 2D explicit dynamics simulation.

5.4. Results and post-processing

The result of interest is the total deformation required to achieve stresses close to the yielding point of the PEEK material. Thus, by selecting the right sub-step of the calculation it is possible to retrieve the result of total deformation and equivalent stresses acting on the PEEK bulk material as shown in Figure 5-5.

If the deformation of an element exceeds 50% of its original geometry, it gets deleted, its nodes get depicted as red dots as shown in the sequence of deformation instants of Figure 5-6.

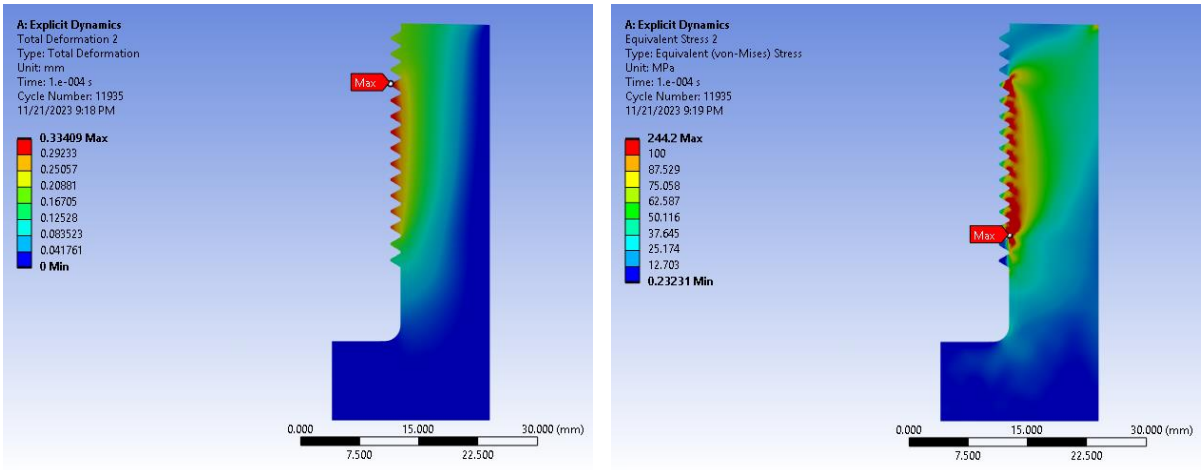

Figure 5-5: total deformation (left) and equivalent stress (right) of 2D explicit dynamics simulation.

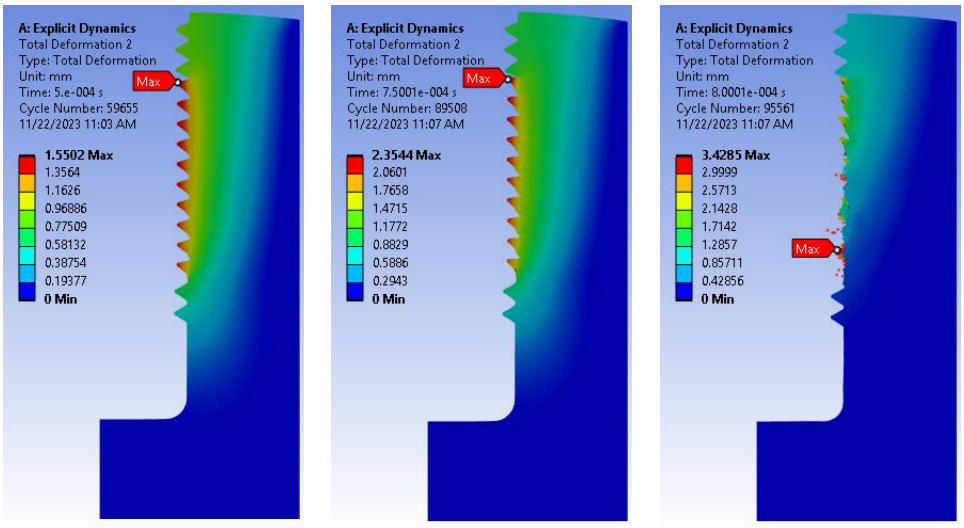

Figure 5-6: fracture sequence of PEEK bulk material from 2D explicit dynamics.

5.5. Result discussion

The second image of the sequence of Figure 5-6 already shows the elimination of an element in the lower part of the bulk material's thread, being its most stressed zone. Furthermore, as shown in Figure 5-5, also the maximum Von Mises equivalent stress in the same area is present at the lowest helicoil PEEK contact. These results are consistent with the fractures geometry and directional propagation seen for all four PEEK insulator samples, some of which are shown in Figure 5-7.

Figure 5-7: fracture at M14 helicoil and PEEK material of the fourth insulator sample.

5.6. Conclusion about 2D Explicit Dynamics model

The numerical modelling of the axisymmetric 2D simplification reveals consistent results in terms of maximal equivalent stress and stress propagation in the PEEK area close to the threaded hole for the M14 screw and M14 helicoil, as shown in Figure 5-8.

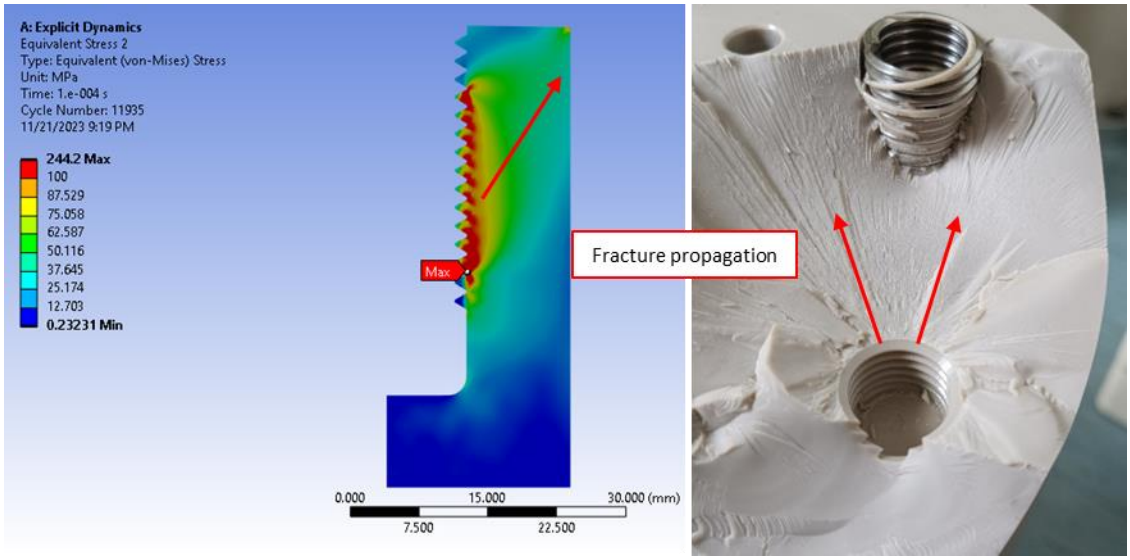

Figure 5-8: comparison of fracture propagation of “D explicit dynamics model and broken PEEK insulator.

6. Realistic 3D PEEK insulator model for tensile test simulation

6.1. Objective

This 3D model has been developed during this thesis and has the objective to evaluate the tensile test of the PEEK insulator in the configuration used for the experimental set-up. It is modelled to have higher geometrical accuracy compared to the already described numerical model of the MTICA Mock-Up insulators, in which screw-bolt connections are neglected. The higher geometrical detail requires smaller elements and more elaborated mesh definition to better capture the geometry, consequently increasing the computational time. However, to better investigate the behavior of the PEEK insulator, it is important to also model such screw and bolts connections.

Before the experimental tests were executed, this model was used to obtain an insight about how the PEEK post-insulator could behave in such tensile test.

6.2. Geometry and Mesh

The 3D geometry involves 5 different major bodies together with the smaller screws, helicoils and bolts:

- 1 insulator of 280 mm height and 130 mm diameter;
- 2 flanges of 25 mm height and 190 mm diameter;
- 2 differently shaped connecting elements between the flanges and tensile machine with lengths of respectively 190 mm and 255mm;
- 12 M14 screws (6 per side) to connect the insulator to the flanges;
- 12 M14 helicoils (6 per side) to better connect the insulator to the flanges, supporting the M14 screws;
- 20 M10 screws and bolts (10 per side) to connect the flanges with the other connecting elements.

A certain amount of approximation remains in this model since the thread of screws, helicoils and bolts are not modelled. Indeed, it is a common practice on ANSYS to model a screw thread as a simple cylinder whose section corresponds to the real screw stress area. For a M14 bolt of pitch 1.5, such area is 115mm, corresponding to a diameter 12.1mm. Helicoils, on the other hand, are often simulated as simple cylinder between the screw thread and the part threaded hole. Simulating a real thread is complex and require much more computational resources.

Therefore, the screws and bolts' surfaces are assumed to be smooth and their contact with other bodies is modelled as bonded contact type. Hence, no sliding or separation between the involved faces or edges is considered. In other words, every connection that involves threads is modelled with bonded contact type. Instead, the more realistic frictional contact type is used to model all connections in which threads are absent. For example, the contact between the

lower surface of a screw's head and the body to which it is fastened. More details of these contacts are given later.

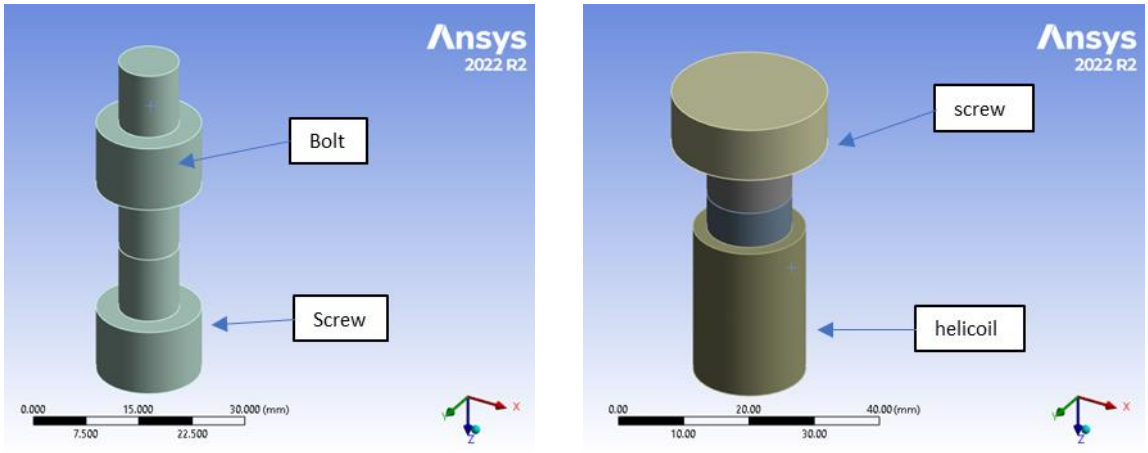

Figure 6-1: simplified model of M10 screw with bolt (left) and M14 screw with helicoil (right).

An example of the complete model's geometry is shown in figure Figure 6-2, in which three reference frames are specified. The "Global" reference frame is defined as default for the entire model. The "Testbed" reference frame is the one shown in Figure 2-9, consistent with target forces and moments expressed in Table 2. Lastly, the "Traction direction" reference frame is needed for the load application of the tensile machine.

An angle of 10.51° is present between the z axis of the "Testbed" and the "Traction direction" reference frames.

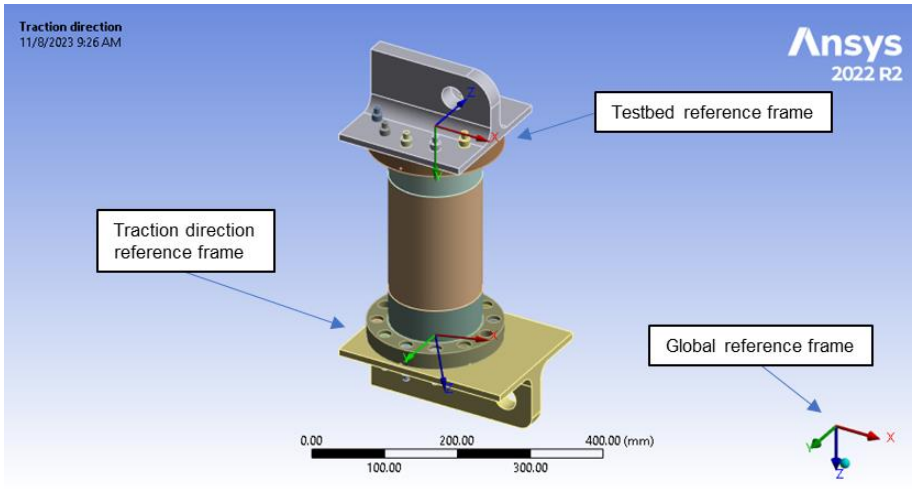

Figure 6-2: simplified geometry of PEEK insulator for tensile test simulation.

For mesh generation, it is notable that the insulator is divided into three parts, to ease the meshing of the central part, being a full cylinder. The upper and lower parts of the insulator include holes to host screws and helicoils making more difficult the generation of a good-quality mesh.

“Adaptive Sizing” is used with “Fast” transition option for the generation of the mesh, focusing on obtaining good mesh metrics in terms of element quality.

Furthermore, since many contacts are present, it is necessary to map the mesh in contact areas, which are between:

- connecting elements and flanges;
- flanges and insulator;
- M10 screws & bolts with connecting elements and flanges;
- M14 screws with flanges and M14 helicoils;
- M14 helicoils and insulator.

The final mesh of the complete model is shown in Figure 6-3.

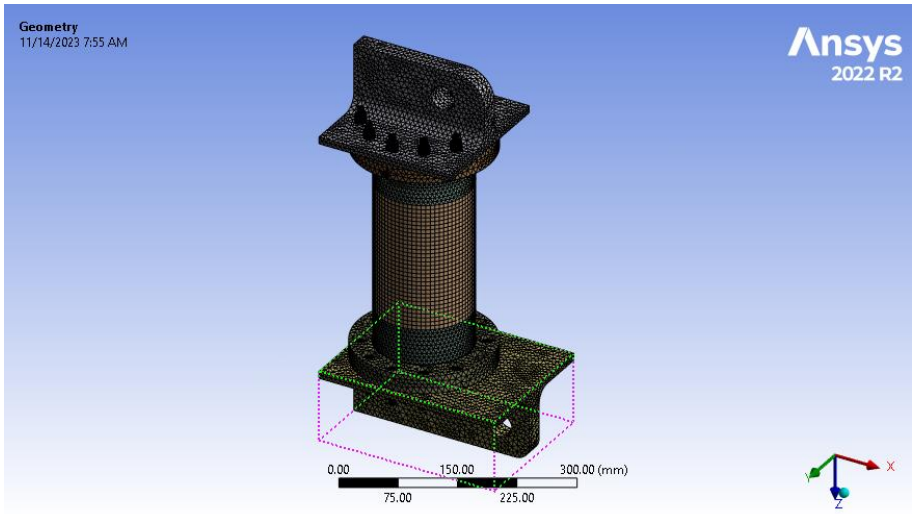

Figure 6-3: mesh of real PEEK insulator model for tensile test simulation.

The statistics of the mesh are: 1201685 nodes and 454125 elements. This high number of nodes and elements is required to accurately represent also smaller geometrical parts of the model such as M10 and M14 screw as shown in Figure 6-4.

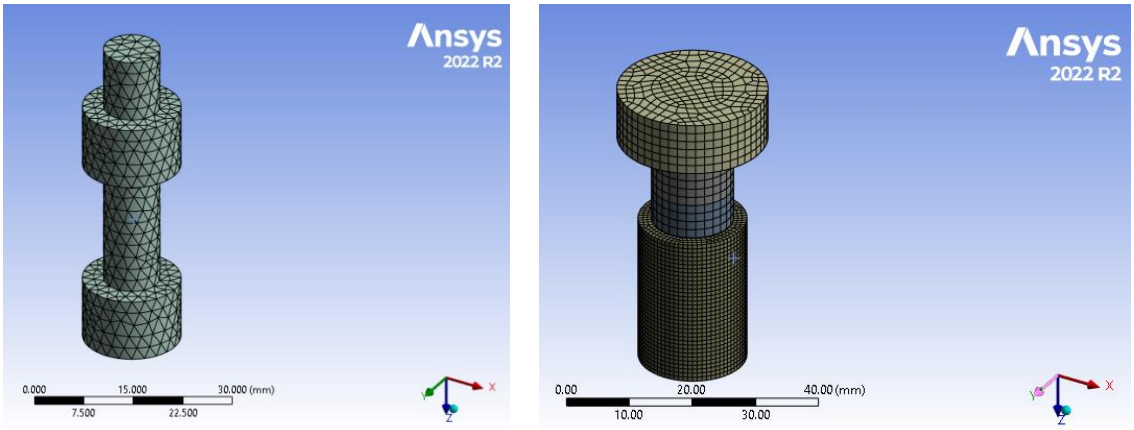

Figure 6-4: mesh of M10 screw with bolt (left) and M14 screw with helicoil (right).

6.3. Boundary conditions

As mentioned in the previous paragraph, many contacts have to be specified using the bonded and frictional connection option, to avoid or allow sliding between parts. In every connection in which threads are present, the bonded contact is used. Whereas for all other connections a frictional contact is applied.

However, in both contact types, it is necessary to specify a “contact” and a “target” surface. Contact elements are constrained against penetrating the target surface. Conversely, target elements can penetrate through the contact surface. Therefore it is suggested to do the following: [53]

- for rigid-to-flexible contact, the rigid surface is the target surface and the deformable surface is the contact surface;
- the surface with finer mesh should be the contact surface and the surface with coarse mesh should be the target surface;
- If a convex surface is expected to encounter a flat or concave surface, the latter should be the target surface.

For better understanding an example of both bonded and frictional contact types are shown in the following, but for sake of brevity not all contact types are explained as the procedure is repetitive.

An example of bonded contact is between the M14 screw and the M14 helicoil, which are responsible for the fastening between the flanges and the PEEK insulator. The real-life components’ geometry is shown in Figure 6-5, whereas the connection of the numerical model is shown in Figure 6-6. The screw’s surface is chosen as the contact surface (in red) since it has a convex shape. Instead, since the helicoil is modelled as a hollow cylinder, its internal surface is chosen as target surface, being of concave shape.

Figure 6-5: respectively from left to right: M14 screw, M14 helicoil and their assembly.

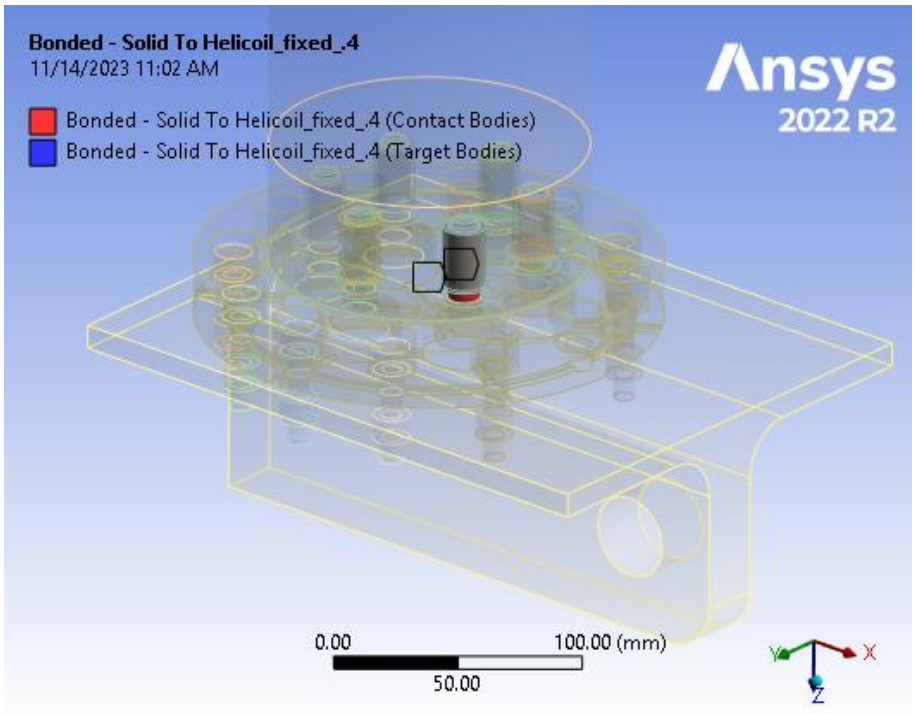

Figure 6-6: connection between M14 screw (contact surface) and M14 helicoil (target surface) in real PEEK insulator model.

An example of frictional contact is between the extremities of the insulator and the flat flanges surfaces. These are tightened together thanks to the bolt pretension induced by the fastening of the M14 screws. A real-life image of the Stainless-Steel flanges connected to the PEEK insulator is shown in Figure 6-7. In such case the connection involves a stiffer material with a softer material. Therefore, the flange's surface is defined as the target surface (in blue), while

the insulator's surface is defined as the contact surface as shown in Figure 6-8 . The friction coefficient is set to 0.2.

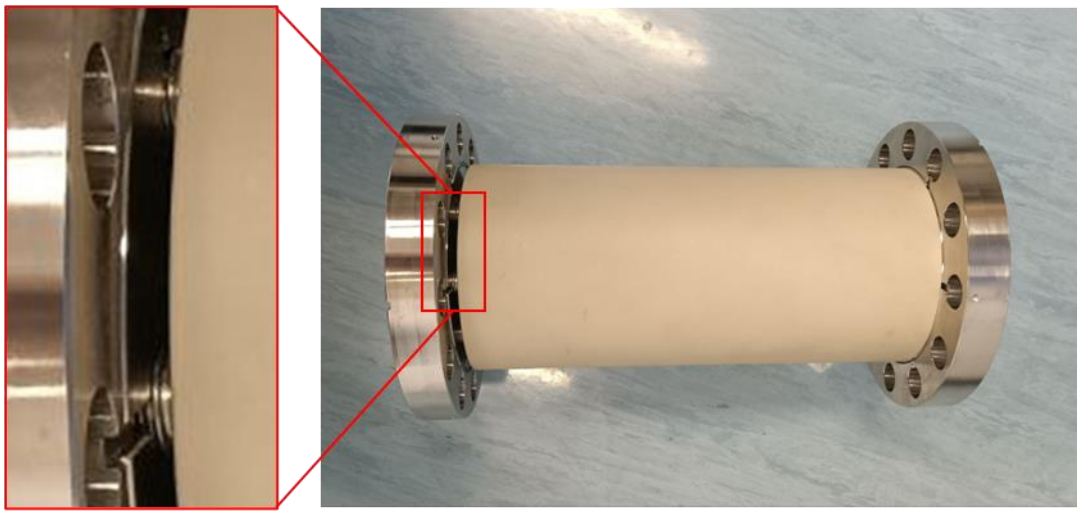

Figure 6-7: contact focus between real-life Stainless-Steel flanges and PEEK insulator.

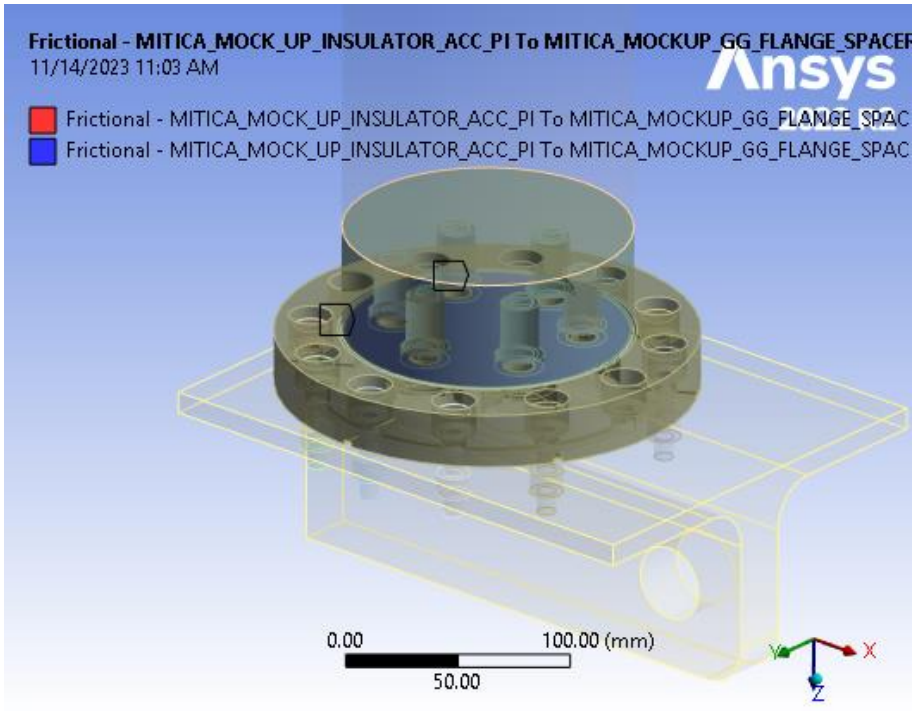

Figure 6-8: connection between bottom flange (target surface) and insulator (contact surface) in real PEEK insulator model.

Once the contacts are specified, it is necessary to define bolt-pretensions of each of the M14 and M10 screws to simulate the tightening of all bodies before the tensile test takes place. On ANSYS, the bolt pretension must be applied on the screw shank, that is on the cylinder surface between the screw head and thread. Bolt pretensions of respectively 20 kN and 10 kN are applied on the M14 and M10 screws. The bolt pretension is applied during a first simulation time step, before the loads corresponding to the tensile test are applied. More precisely the time steps are defined as follows:

- Load step 1: bolt pretension of M14 and M10 screws ("Load" option);
- Load step 2: locking of the screw element displacements ("Lock" option), lower value of tensile force;
- Load step 3: higher value of tensile force.

In case of the M14 screws, the tabular data looks like in Table 12. On the first step the load is applied, while in the second and third steps the contact is locked.

Steps	Define by	Preload [N]
1	Load	20000
2	Lock	N/A
3	Lock	N/A

Table 12: bolt pretension for M14 screw of real PEEK insulator model.

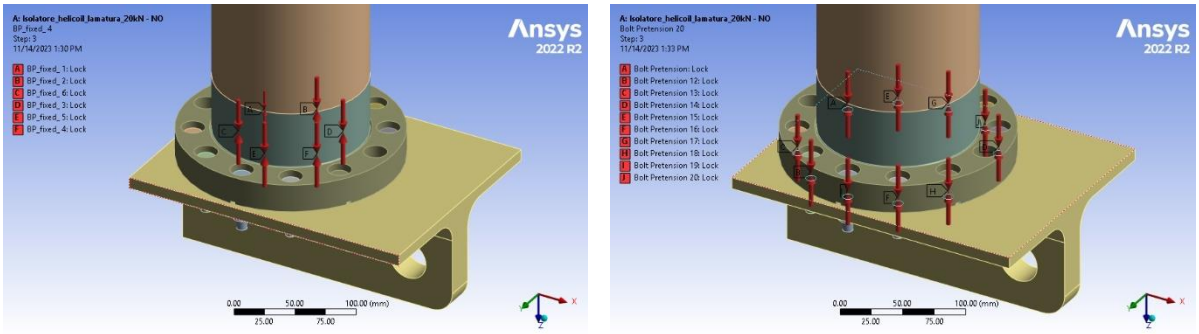

Figure 6-9: bolt pretension of 6 M14 (left) screws and 10 M10 screws (right) at the bottom part of the real PEEK insulator model.

Lastly, the tensile force of the machine must be applied along the "Traction direction" reference frame. To do so, a predefined displacement along the traction direction is applied to the two centres of the connecting bracket cylindrical apertures (upper bracket and lower bracket). Thus, the displacements that generate tensile forces of at least 21.1 kN and 48 kN need to be defined. The equivalent reaction force in z direction at the points A and B of the model (previously defined in Figure 2-9) can be calculated in the post-processing of the simulation.

These displacements are then applied respectively at the second and third load steps for the upper connecting element. Conversely the lower connecting element is fixed by imposing null displacements and rotation. However, in both remote displacements the rotation around the y axis (in green) remains free to allow flection of the insulator as shown in Table 13 and Figure 6-10.

Load steps	X [mm]	Y [mm]	Z [mm]	RX [°]	RY [°]	RZ [°]
1	0	0	0	0	Free	0
2	0	0	-4	0	Free	0
3	0	0	-8	0	Free	0

Load steps	X [mm]	Y [mm]	Z [mm]	RX [°]	RY [°]	RZ [°]
1	0	0	0	0	Free	0
2	0	0	0	0	Free	0
3	0	0	0	0	Free	0

Table 13: remote displacement A (upper) and remote displacement B (lower) applied on connecting elements according to “Traction direction” reference frame.

The values of 4 and 8 mm are chosen to cover a large range of load-displacement curve. A change of such values does not lead to significant differences since the structural simulation is assumed to be linear.

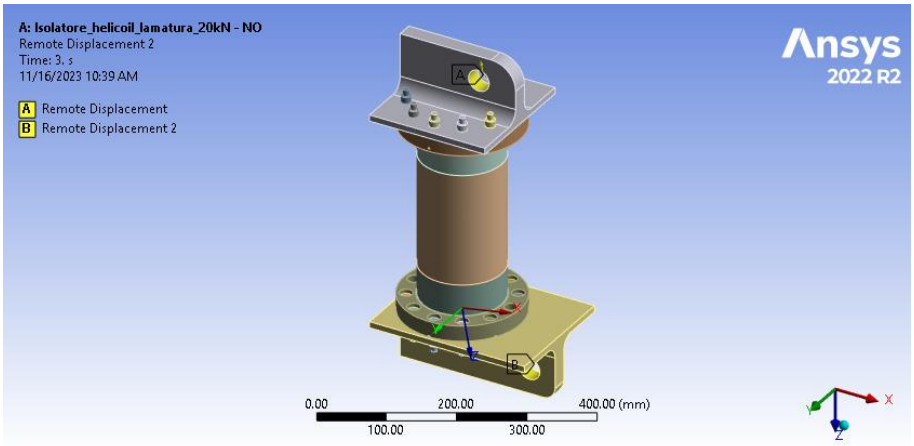

Figure 6-10: remote displacements of real PEEK insulator model for tensile test simulation.

6.4. Results and Post processing

The first results of interest are the reaction forces in z direction according to the “Traction direction” reference frame for one of the points A and B (since they are equal and opposite). This data allows to determine if tensile forces close to the target ones of 21.1 kN and 48 kN were reached. The results scale is set to be in this case equal to 15 times the true scale. The model is show in Figure 6-11, while the tabular data of the reaction force of one of the extremities is shown in Table 14.

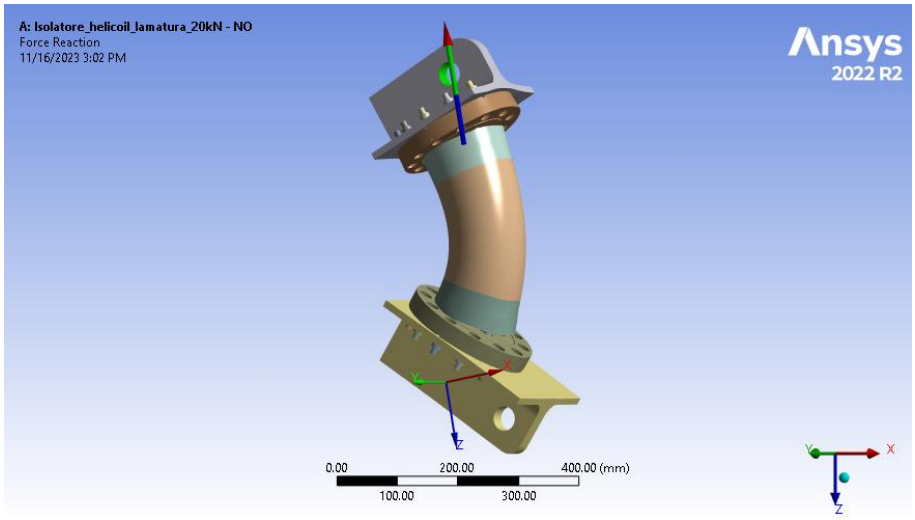

Figure 6-11: upper force reaction on real PEEK insulator model.

Load steps	Force Reaction (X) [N]	Force Reaction (Y) [N]	Force Reaction (Z) [N]	Force Reaction (Total) [N]
1	0.26	1.70	-3047.4	3047.4
2	1.54	-60.11	-101340	101340
3	3.55	-162.51	-194590	194590

Table 14: reaction forces on upper part of the real PEEK insulator model.

This shows that for a displacement lower than 4 mm, the yielding stress of the PEEK material, being 99.5 MPa, should be reached. Thus, the model is not valid beyond that point due to the presence of non-linear plastic behaviors.

Another result of interest is the equivalent stress acting only on the PEEK insulator, which is to be compared to the material yield strenghtt. At loading step number 2, corresponding to a

remote displacement of -4 mm in z direction of the “Traction direction” reference frame, the overall stress acting on the PEEK insulator is almost below 50 MPa as shown in Figure 6-12.

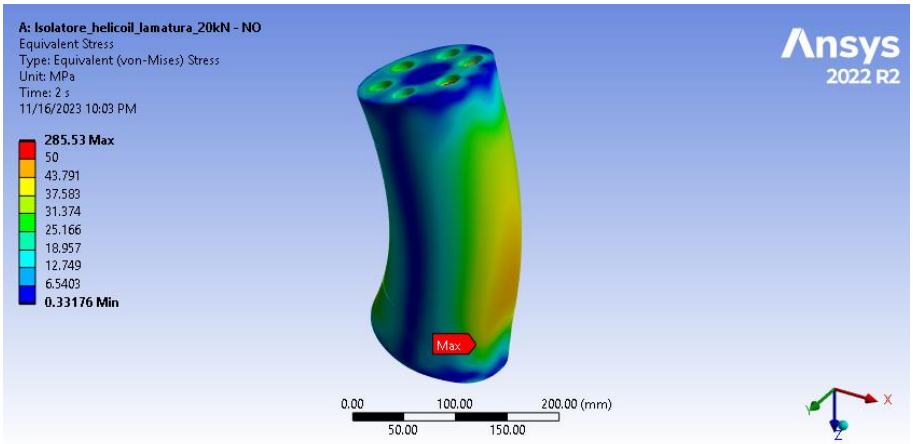

Figure 6-12: equivalent stress acting on the real PEEK insulator model.

At the same time, peaks well above the yielding point of the material are shown inside 2 of the 6 screw holes of the bottom part of the insulator, as shown in Figure 6-13. These are mostly stressed due to traction force and bending moment acting at the same time.

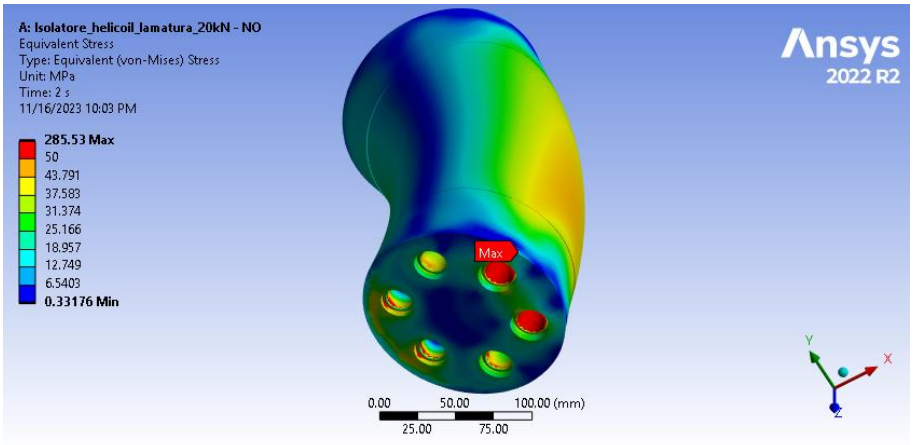

Figure 6-13: max equivalent stress acting on real PEEK insulator model.

6.5. Results discussion

A direct comparison of the numerical result with the experimental data reveals the significantly greater stiffness of the numerical model, which does not correctly describe the real-life mechanism with accuracy beyond the first part of the load-displacement curve as shown in Figure 6-14.

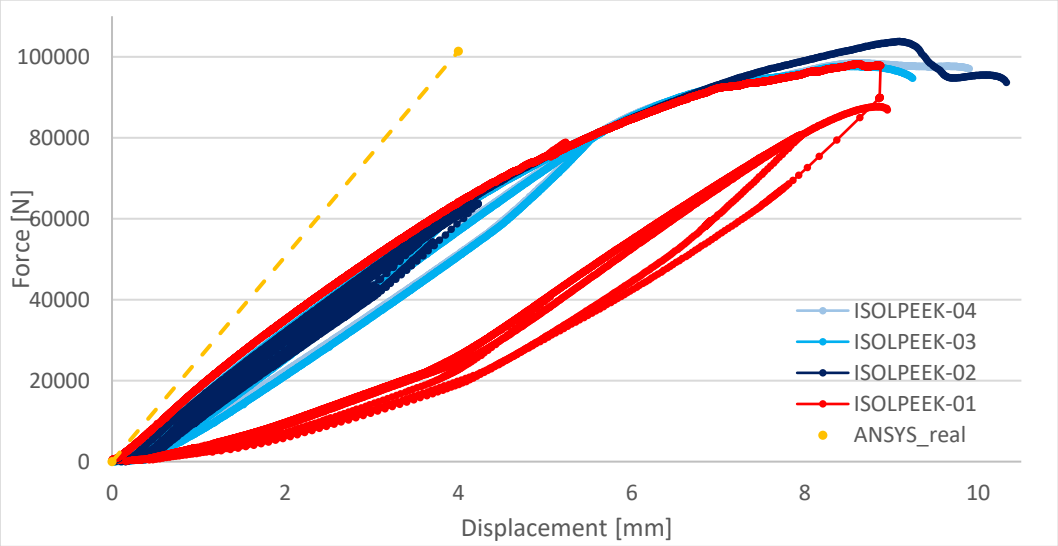

Figure 6-14: comparison of ANSYS real PEEK insulator model with experimental data.

Two possible causes are identified which can cause early stiffness weakening of the PEEK insulator:

- local plasticity affects the tightening effectiveness of the 2 most stressed M14 screws, decreasing the stiffness of the whole model;
- the modelling of the screws, helicoils and bolts threads as smooths surfaces with bonded contact type is responsible for overall higher stiffness compared to the real-life scenario.

The former is related to the presence of non-linear behaviors induced by an initial hardening of the material which then leads to high deformation and material failure. Modelling of local non-linearities of the material is difficult and might not be of great interest since usually the integrity of a structure is defined by avoiding the presence of global and local plasticity.

The latter, instead, could be an explanation of interest even if only material elastic ranges are considered. If it were true that the behavior of the simplified modelling of the contact between screws and helicoils is stiffer than in reality, then such modelling would overestimate the assembly stiffness, which is a non-conservative error. Higher values of deformation could be present compared to the simplified modelling of the screw and helicoil contacts.

6.6. Conclusion about the realistic 3D PEEK insulator model

The tensile test of the PEEK insulator simulated using higher geometrical accuracy compared to the already existing numerical model of MITICA Mock-Up electrodes has revealed:

- Values of equivalent stress macroscopically lower than 50 MPa on the insulator in case of a remote displacement of -4 mm, corresponding to a reaction force of 101340 N;
- Significantly higher stiffness for the numerical model compared to the experimental data.

Therefore, it is of interest to investigate if similar results are obtained by numerical modelling of the same experiment with a geometry like the simpler one used in the MITICA Mock-Up electrodes model. Thus, the simplified PEEK insulator model is described in the next section, in which M14 screws, M10 screws, helicoils and bolts are neglected.

7. Simplified PEEK insulator model for tensile test simulation

7.1. Objective

This model has the objective to understand the consequences of modelling the real-case scenario of the tensile of PEEK insulators with a simplified geometry, as done for the MITICA Mock-Up electrodes numerical model. Neglecting screws and bolts connections in the model affects the accuracy of the numerical simulation by a certain amount that can be quantified. Quantifying this amount can demonstrate whether this procedure leads to a non-negligible error or not.

7.2. Geometry and Mesh

As mentioned in the guidelines, the real geometry of the experimental set-up can be simplified. All screw and bolt connections together with the threaded holes are neglected, so that both the PEEK insulator and the pair of flanges are modelled as solid cylinders of different sections.

Nonetheless, all major dimensions are conserved:

- Insulator's diameter of 130 mm;
- Insulator's length of 280 mm;
- Flanges' diameter of 190 mm;
- Flanges' thickness of 25 mm;
- Total length of insulator + flanges of 330 mm.

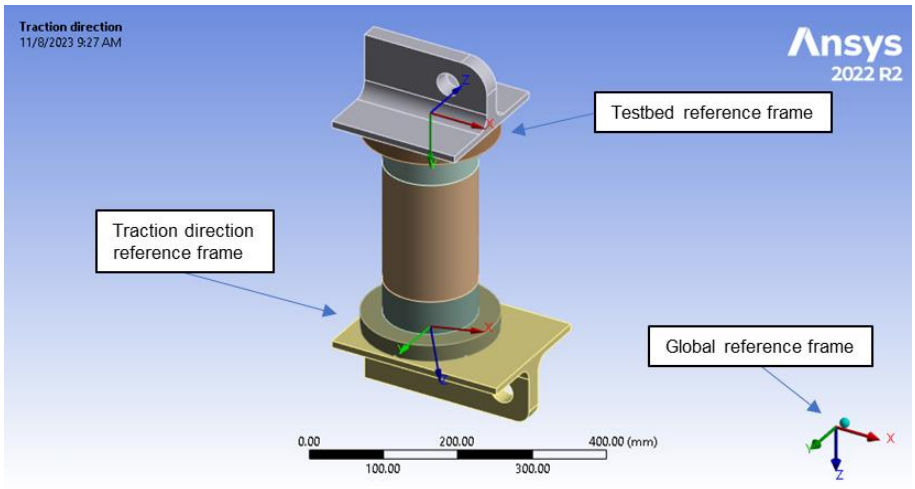

Figure 7-1: simplified geometry of PEEK insulator for tensile test simulation.

As for the previous model, “Adaptive Sizing” is used with “Fast” transition option for the generation of the mesh, focusing on obtaining good mesh metrics in terms of element quality. Hexagonal elements model the PEEK post-insulator, whereas the flanges and the connecting elements are modelled with tetrahedrons.

The statistics of the mesh are: 307725 nodes and 121307 elements. It contains about 75% less nodes and elements compared to the real case PEEK insulator model previously described. These statistics, together with the exclusively linear contacts, considerably reduce the runtime of the simulation.

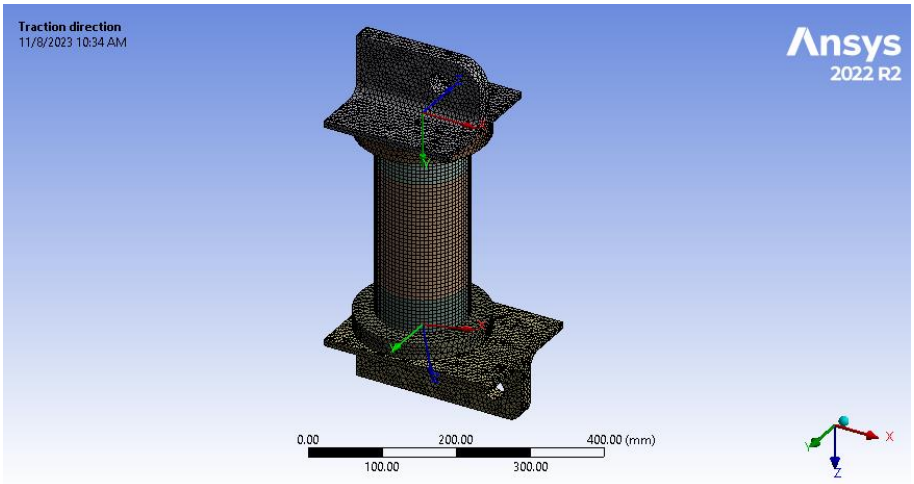

Figure 7-2: mesh of simplified PEEK insulator model for tensile test simulation.

7.3. Boundary conditions

The contact type established between all parts is bonded and the only other imposed boundary conditions are 2 “remote” displacements to the connecting brackets, in correspondence to the cylindrical holes to which the machine grippers are fixed.

The lower connecting element is blocked in all displacements and 2 rotations, allowing only a rotation along the y direction. The upper connecting element is constrained in 2 displacement directions and 2 rotations. Then, a displacement along the z axis of the “Traction direction” reference frame is imposed and only free rotation along the y direction is allowed.

In the “Step Controls” of the “Analysis settings”, 20 different step loads have been defined assigning up to a negative value of -4mm with intervals of 0.2 mm for each step. This allows to:

- sooner identify a value of displacement that generates reaction forces close to the ones of interest (21.1 kN and 48 kN);
- have results also beyond the nominal operation (NO);

- avoid reaching values out of the elastic range which would be inconsistent.

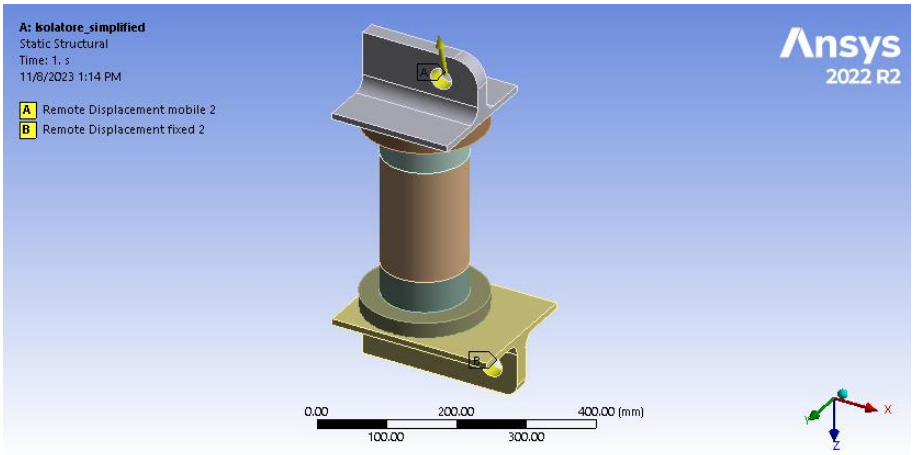

Figure 7-3: remote displacements of simplified PEEK insulator model for tensile test simulation.

7.4. Results and post-processing

As for the previous model, the first set of results concerns the reaction forces in z direction according to the “Traction direction” reference frame for at least one of the points A or B, more precisely on the bonded connection between the PEEK insulator and the flanges.

The results scale of the model shown in Figure 7-4 is set to be in this case equal to 15 times the true scale, while the tabular forces close to the target ones of 21.1 kN and 48 kN are shown in Table 15.

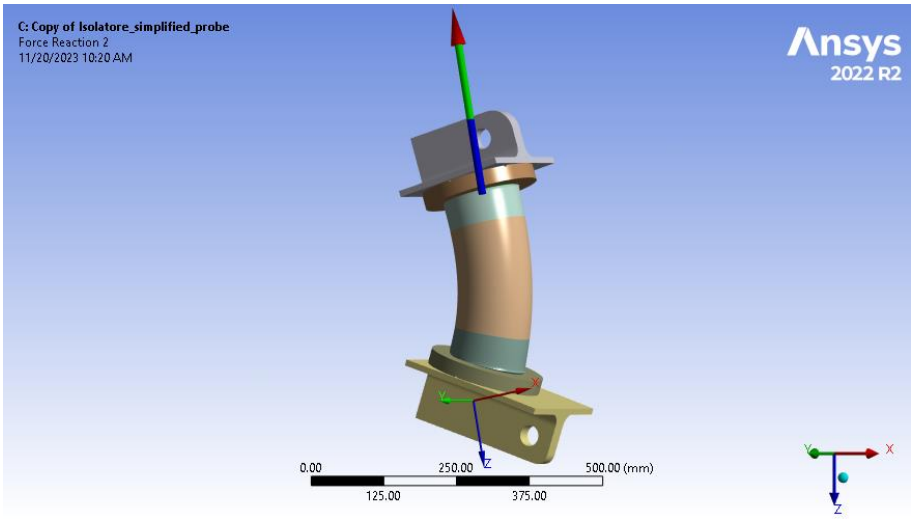

Figure 7-4: upper force reaction on simplified PEEK insulator model.

Load steps	Force Reaction (X) [N]	Force Reaction (Y) [N]	Force Reaction (Z) [N]	Force Reaction (Total) [N]
4	-0.77099	-0.43704	-21900	21900
9	-1.7347	-0.98333	-49276	49276
20	-3.85	-2.1853	-109500	109500

Table 15: reaction forces on upper part of the simplified PEEK insulator model.

The other result of interest is the equivalent stress acting only on the simplified PEEK insulator. At loading step number 2, corresponding to a remote displacement of -1.8 mm in z direction of the “Traction direction” reference frame, the overall stress acting on the PEEK insulator is almost below 30 MPa, well below the yielding point as shown in Figure 7-5.

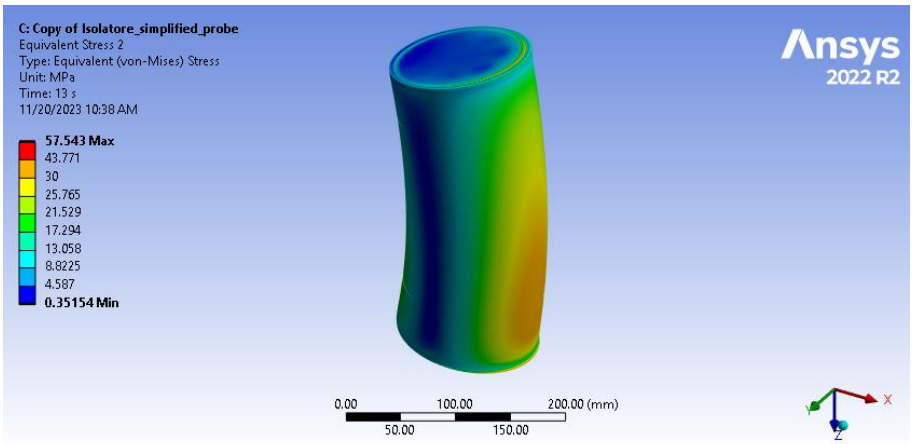

Figure 7-5: equivalent stress acting on the simplified PEEK insulator model at load step 2.

7.5. Results discussion

Plotting the numerical results with the previous numerical model and the experimental data, as shown in Figure 7-6, reveals:

- significantly higher stiffness for the numerical model compared to the experimental data;
- increased stiffness of the simplified PEEK insulator model (light green) compared to the real PEEK insulator model (orange).

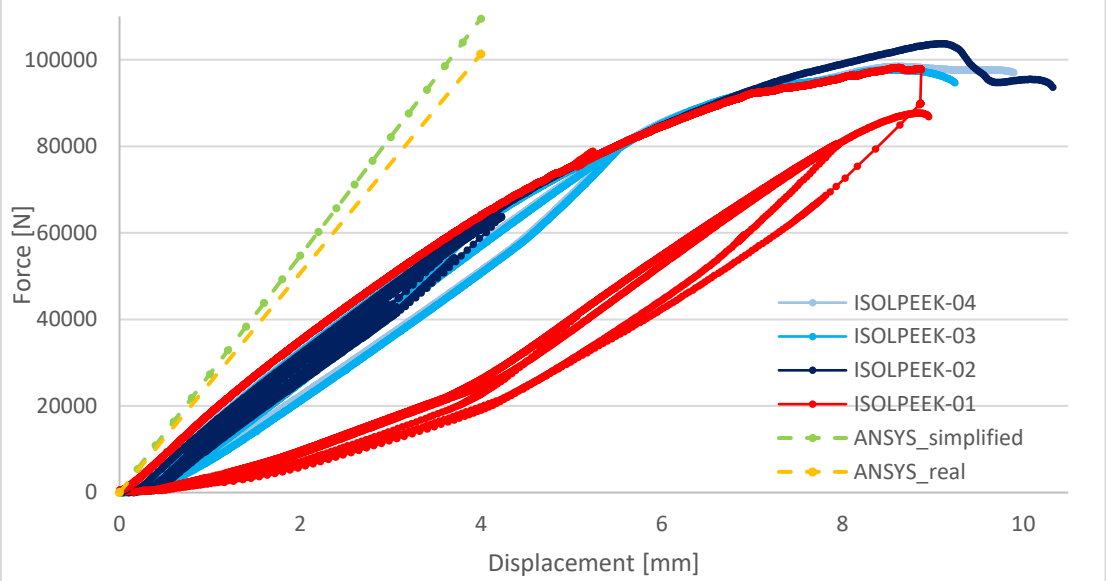

Figure 7-6: comparison of ANSYS simplified PEEK insulator model with experimental data and previous real PEEK insulator model.

The discrepancy between the stiffness of the numerical models and the experimental data has a direct impact on the whole MITICA Mock-Up electrodes model. Indeed, higher stiffness leads to lower values of displacements, but also increases the frequency of the structure natural vibration modes, following the vibration theory highlighted in Section 4.4. Therefore, optimizing the numerical model to better fit the experimental results, allows to see whether a non-negligible modelling error has been made on the MITICA Mock-Up.

To better fit the experimental results, the elastic modulus of the PEEK material has been changed, decreasing its value to 2630 MPa, instead of the original 3850 MPa. In other words an **equivalent PEEK material** is defined and used, with the sole purpose of artificially reproducing the experimental behavior without any indication on the real material behavior. This technique allows to report the experimental results on other broader models without the need to explain and correct the discrepancy between the tensile test and the insulator model. The force-displacement plot of the simplified PEEK insulator model with the equivalent PEEK material better fits the experimental results, by the very design of the virtual material. The last

load step of -4 mm together with the step load numbers in which the remote displacements generate force reactions close to the ones of 21.1 KN and 48 kN are shown in Table 16.

		Force reaction direction			
Load step	Remote Displacement	x	y	z	Total
[n°]	[mm]	[N]	[N]	[N]	[N]
6	-1.2	0.79728	0.43572	22648	22648
13	-2.6	1.7275	0.94428	49070	49070
20	-4	2.6577	1.4525	75493	75493

Table 16: remote displacement values at max force reaction and close to nominal operation conditions of 21.1 kN and 48 kN.

The results plot of the better fitting model “ANSYS_simplified_updated” is shown in Figure 7-7.

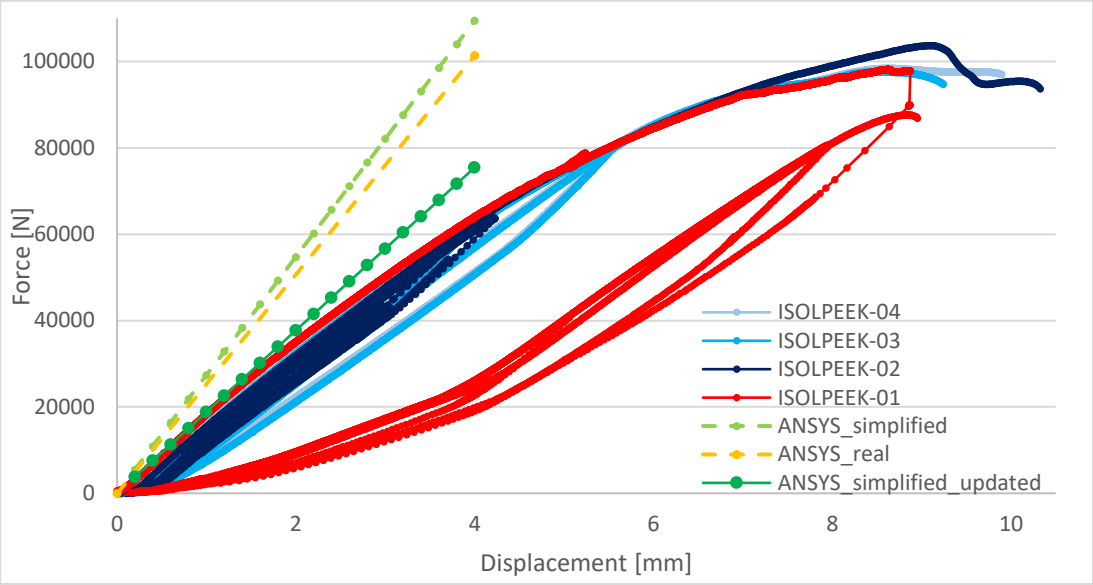

Figure 7-7: comparison of ANSYS updated simplified PEEK insulator model with experimental data and previous numerical models.

The data obtained through these simulations allows to define the precise machine loading force at which the behavior of the PEEK insulator cannot be considered elastic anymore. Thanks to the linear interpolation of both numerical and experimental results together with their comparison it is possible to:

- verify if numerical and experimental Force-displacement curve's slopes are similar;
- define a load limit over which the PEEK insulator, with the designed experimental set-up, does not possess only linear-elastic behavior anymore.

The slope of the numerical curve is calculated by linear interpolation and is found to be of 18873 N/mm as shown in Appendix C. Instead, the slope of the experimental curve is found by averaging the slopes of every similar loading cycle reaching up to 80 kN, but not above it.

The reason why only the first loading cycle of the first PEEK sample is considered and none of the fracture curves of all four PEEK insulator is related to the damaging of the material after the application of high loads. In fact, after every loading cycle, the material is weakened, resulting in a decreasing Force-Displacement curve slope. When values close to the fracture are reached, this slope is excessively weakened to be considered for the evaluation of an average experimental Force-Displacement slope, valid for elastic ranges.

As an example, Figure 7-8 shows the evaluation of the Force-Displacement slope in the first loading cycle of the first PEEK. All linear interpolations are shown in the Appendix C and listed in Table 17.

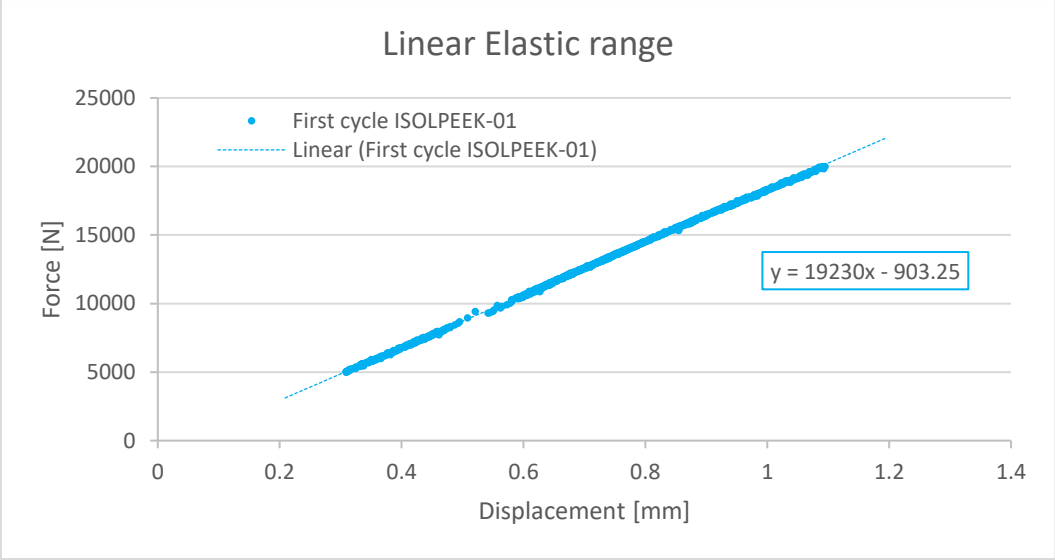

Figure 7-8: Ilinear interpolation of force range between 5 kN and 20 kN in first loading cycle of PEEK sample n°1.

	Equations	Slope
First cycle ISOLPEEK-01	y = 19230x - 903,25	19230
ISOLPEEK-02-RAMPA20kN	y = 19175x - 5862,7	19175
ISOLPEEK-02-RAMPA40kN	y = 19041x - 5773,6	19041
ISOLPEEK-02-RAMPA50kN	y = 18615x - 5697,2	18615
ISOLPEEK-02-RAMPA50kNbis	y = 18531x - 6163,9	18531
ISOLPEEK-02-RAMPA60kN	y = 18428x - 6009,4	18428
ISOLPEEK-03-RAMPA20kN	y = 18829x - 3509,7	18829
ISOLPEEK-03-RAMPA40kN	y = 18940x - 3723,1	18940
ISOLPEEK-03-RAMPA60kN	y = 18589x - 3914,8	18589
ISOLPEEK-03-RAMPA80kN	y = 17919x - 4502,8	17919
ISOLPEEK-04-RAMPA20kN	y = 19252x - 3543,1	19252
ISOLPEEK-04-RAMPA40kN	y = 19325x - 3775,8	19325
ISOLPEEK-04-RAMPA60kN	y = 19057x - 3975,5	19057
ISOLPEEK-04-RAMPA80kN	y = 18428x - 4448,8	18428
	average	**18811.4**

Table 17: average force-displacement slope of PEEK insulator samples.

All linear interpolations are defined in a range in between 5 kN and 20 kN. The lower value is chosen not to consider the non-zero starting point of some of the force-displacement curves. As a matter of fact, some of the loading curves show lower slopes, hence higher deformability, for values below 5 kN. Instead, the upper value of 20 kN is chosen to consider as little non-linearity as possible, while still considering a relevant number of points in the chosen range.

As a result, the averaged force-displacement slope of 18811 N/mm and the numerical one of 18873 n/mm differ only by 0.3%.

Lastly, a relative error of 2% between the updated simplified PEEK insulator model and the experimental curves is defined to determine the load limit beyond which the PEEK insulator is not in elastic range anymore. However, the numerical model's curve must be calibrated using an offset in displacement direction since some of the loading curves do not start from (0;0) coordinates of the force-displacement graphs.

For example, the second PEEK insulator sample has the 20,40,50 kN and 60 kN ramps starting away from the origin of the force-displacement graph shown in Figure 7-9. Thus, to match at least the 20 kN and 40 kN ramps. In this case the chosen offset is of 0.3 mm, translating horizontally the curve by that amount. The calibration of the other PEEK samples are displayed in the Appendix D.

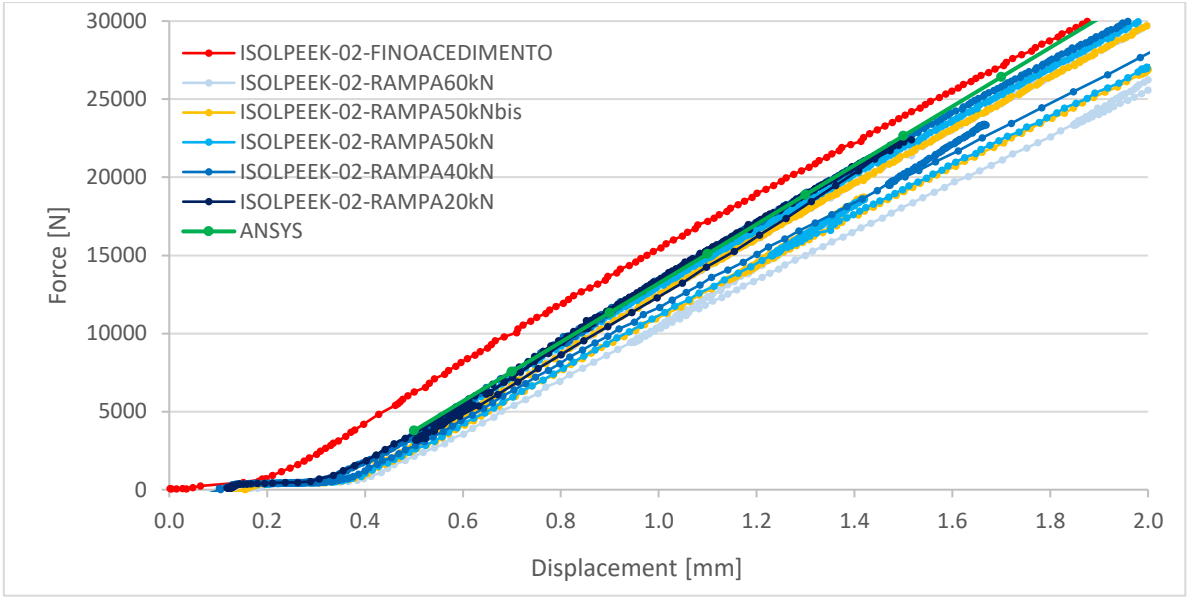

Figure 7-9: calibration of numerical force-displacement curve with experimental data of PEEK insulator sample n°2.

Afterwards, it is possible to identify the relative percentual error between the numerical and experimental points, defined as:

$$\%\, err = \frac{|(F_{numerical} - F_{experimental})|}{F_{numerical}} \cdot 100$$

Therefore, the difference between the numerical force value and the experimental force has to be higher than 2% to identify the upper load limit for elastic range. Nevertheless, due to the fluctuation of the experimental result, the upper load limit is identified if at least 2 consecutive points possess relative percentual error greater than 2%.

In case of the second PEEK sample such value is identified of 25554 N as shown in Appendix E. The calibration and relative percentual error determination is executed for all four PEEK sample. The results are summarised in Table 18. Among all 4 PEEK insulator, the worst value is chosen as final load limit for elastic range operation of the PEEK insulator, being of 24658 N.

N. sample	Force
/	N
1	26873.344
2	25554.63
3	**24658.24**
4	24882.336

→

limit value:
24658.24

Table 18: summary of load limits for all 4 PEEK samples.

7.6. Conclusion about the simplified PEEK insulator model

The modelling of the tensile test of the PEEK insulator in the experimental set-up with simplified geometry as for the already modelled MTICA Mock-Up numerical model has revealed:

- Both numerical models exhibit greater overall stiffness compared with experimental data;
- The simplified PEEK insulator model has greater stiffness compared to the detailed model;
- A better fit of the simplified model vs. the experimental results is obtained using a **equivalent PEEK material**, having an elastic modulus of 2630 MPa instead of the original 3850 MPa of PEEK;
- the average force-displacement slope of the experimental data is of 18811 N/mm;
- the numerical model making use of virtual PEEK material has a force-displacement slope of 18873 N, only 0.3% different from the experimental result;
- the upper load limit for elastic range of the PEEK insulator is of 24658 N, beyond this point the relative error on the reaction force with respect to linear elastic simulation for a same displacement value exceeds 2%.

The models discussed here below describe the whole structure of the MITICA Mock-Up Beam Source as modelled previously, without taking into account the discrepancy between the numerical and experimental results of the tensile test. Re-running such models using the equivalent PEEK material allows to check whether significant differences are caused by this mismatch.

8. Static structural FEM model of MITICA Mock-Up electrodes

8.1. Objective

The aim of this model is to perform static structural simulation using the calibrated equivalent PEEK material to verify if non-negligible overall inconsistencies exist in the adopted numerical models. The result of interest is the total deformation of the structure.

Since this model is already explained in detail in [42], focus is majorly given to the comparison of the new final results with the previous ones.

8.2. Geometry and Mesh

This model of the MITICA Mock-Up electrodes uses simplified contact geometries (the same used in the simplified PEEK insulator model). As shown in Figure 8-1 and described in the technical notes [42], the geometry of the Electrostatic Shield and accelerator are greatly simplified (ignoring small details, substituting some components by lumped mass and using simplified contacts) to reduce the computational resources needed.

The final mesh statistics are 5230928 nodes and 2530758 elements, thus requiring long running times, but yielding more accurate results. Also due to the large number of elements, the mesh is not shown as it would hinder the geometry comprehension.

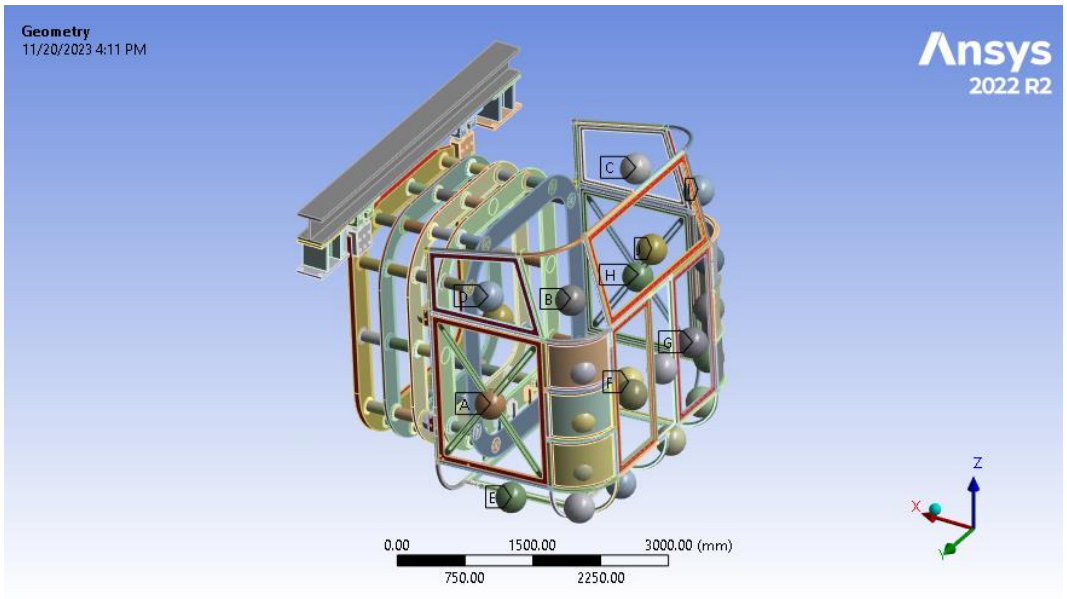

Figure 8-1: Strucutral model of the MITICA Mock-Up electrodes.

8.3. Boundary conditions

As shown in Figure 8-2, the imposed boundary conditions are:

- Standard Earth gravity of 9.8066 m/s^2;
- Displacement of -50 mm in x direction for the tilting system (yellow);
- Fixed support on the steel beam supporting the whole structure (blue).

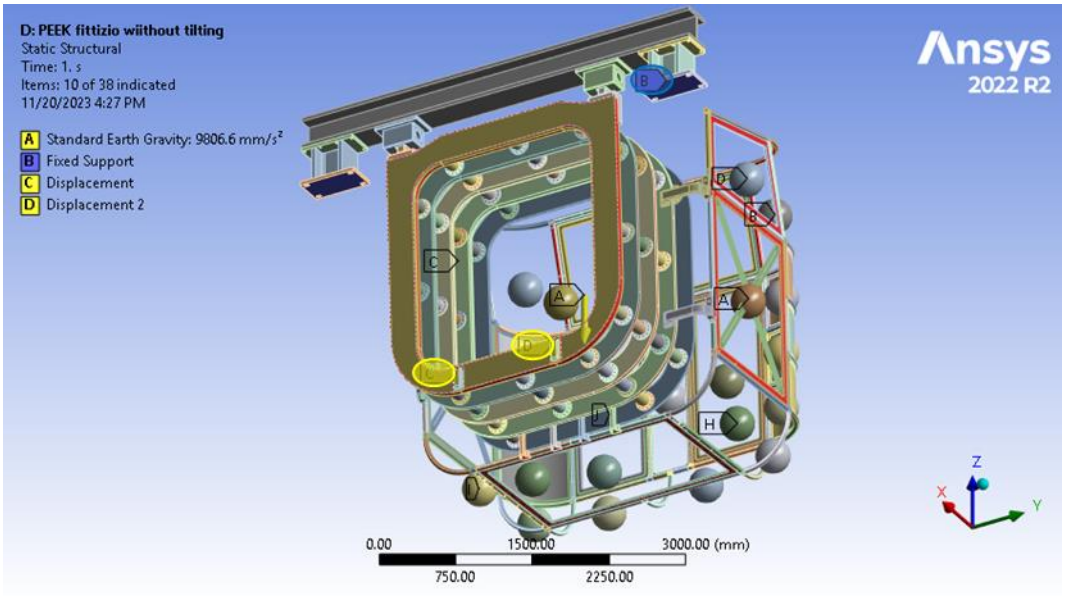

Figure 8-2: boundary conditions of MITICA Mock-Up electrodes model.

8.4. Results and post-processing

The result of interest is the maximum value of the structure's total deformation when the equivalent PEEK is used instead of the real one. Indeed, the structure deformation is critical point to check. From the electrostatic standpoint, a too large deformation could unmask some sharp or protruding elements and decrease the vacuum gaps between ME08 and ME10, increasing the risk of electrical breakdown. This result is compared with those obtained using the real PEEK material properties.

Figure 8-3 shows the total deformation, with scale 292 times the true scale, of the MITICA acceleration grids without the BS and the electrostatic shield using the real PEEK material and then the equivalent one. Furthermore, Figure 8-4 shows the same with the additional shield mounted on the structure, with scale 730 times the true scale.

The differences caused by the use of real or equivalent PEEK causes changes lower than 0.6 mm in total,

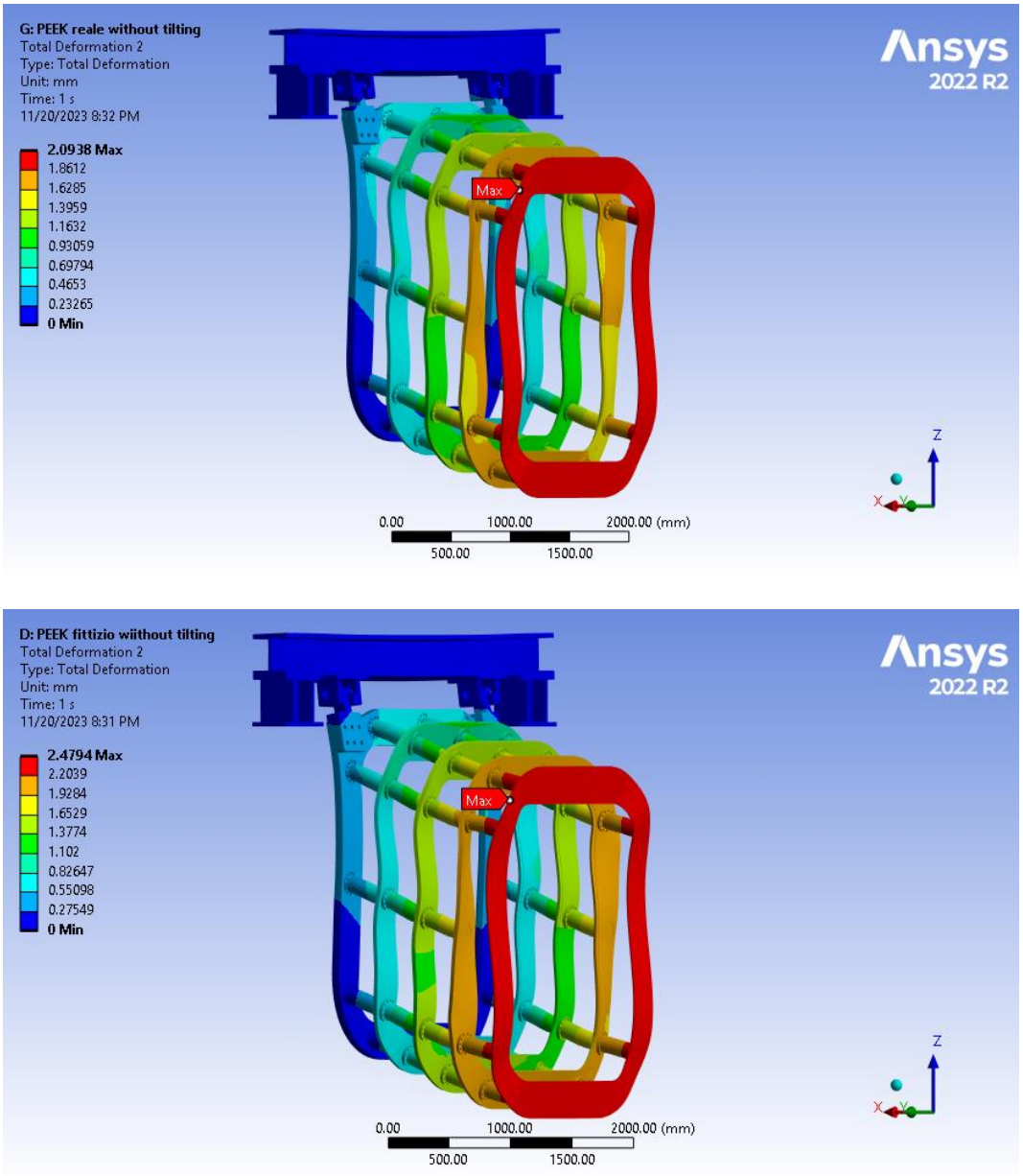

Figure 8-3: total deformation comparison of acceleration grids of MITICA Mock-Up electrodes model with real (top) and equivalent (bottom) PEEK.

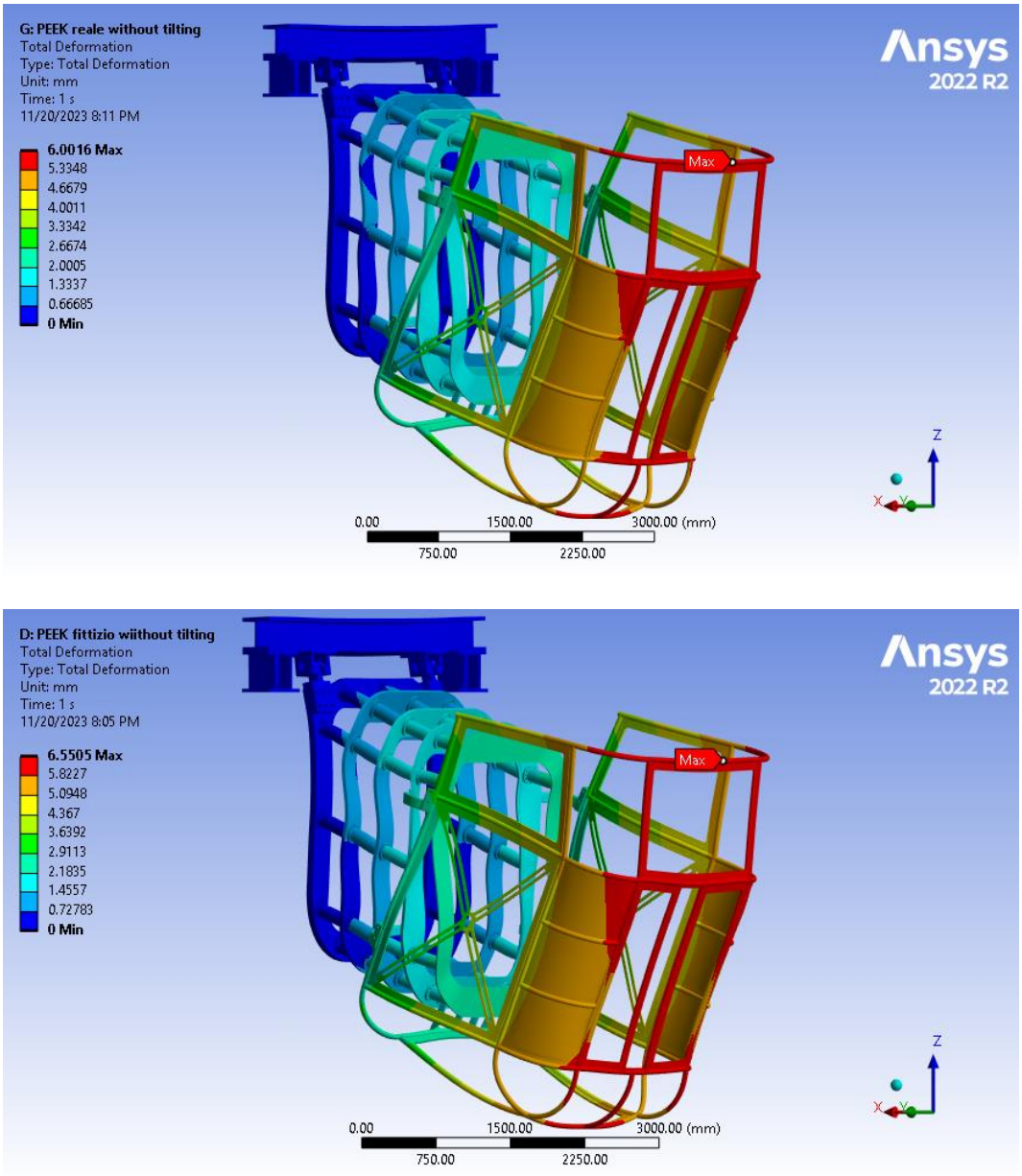

Figure 8-4: total deformation comparison of MITICA Mock-Up electrodes model with real (top) and equivalent (bottom) PEEK.

8.5. Conclusion about the structural model of the MITICA Mock-Up electrodes

The difference between the modelling of the MITICA Mock-Up electrodes using real or equivalent PEEK shows a difference of max 0.55 mm, as summarised by Table 19. This deformation remains anyway acceptable from an electrical insulation point of view, confirming the structural verification of the design of the MITICA Mock-Up electrodes model, even with the addition of the -600 kV electrostatic shield. In fact, the maximum additional deformation with the Electrostatic Shield ES06 is below the limit allowed of 10 mm[42].

	total deformation [mm]		absolute difference [mm]	relative difference [%]
only acc. grids	2.0938	2.4794	0.3856	18.42
acc. grids + shield	6.0016	6.5505	0.5489	9.15
PEEK type	real	equivalent		

Table 19: tabular results of maximal total deformations of MITICA Mock-Up electrodes model.

Since the stiffness of the PEEK insulator has been changed, it is also necessary to verify whether the natural frequencies of the structure have been substantially altered or not. Hence, a modal analysis is necessary to investigate this aspect.

9. Modal analysis of MITICA Mock-Up electrodes model

9.1. Objective

The aim of this analysis is to evaluate the natural frequencies of the structure using the calibrated virtual PEEK material and compare it to the original values of the simulation which make use of the real PEEK material.

As for the previous static structural model, this model is already explained in detail by technical notes [42]. Therefore, the focus is mainly given on the comparison of the new final results with the previous ones.

9.2. Geometry and Mesh

Since modal analysis are computationally expensive compared to static structural analysis, a coarser mesh is used even though the geometry is the same as the previous model. As a matter of fact, the mesh statistics is of 2978414 nodes and 1259848 elements, almost 60% less than in the static structural analysis. The mesh is shown in Figure 9-1.

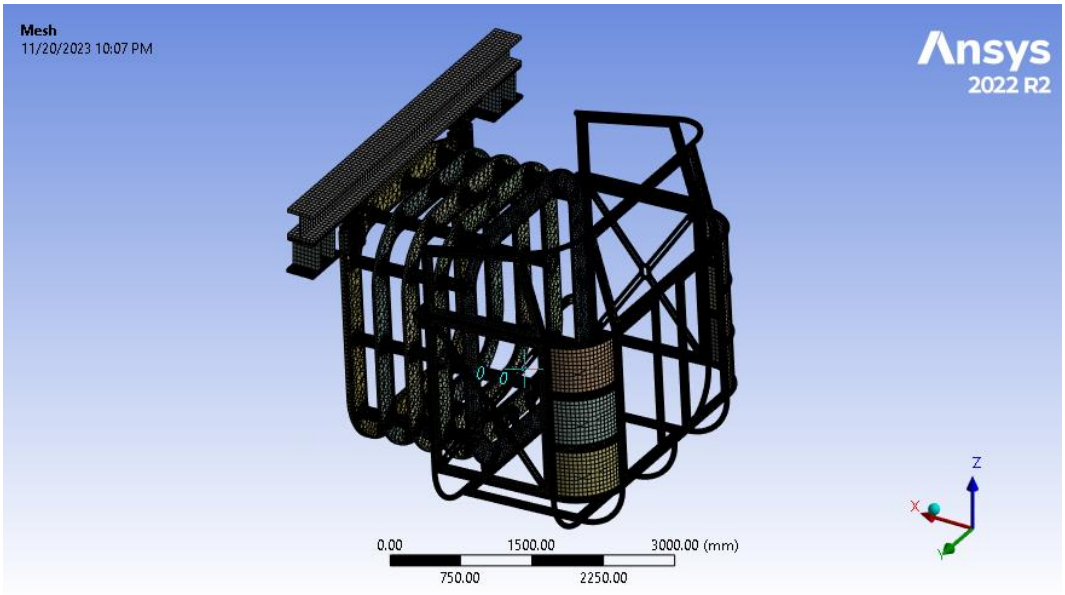

Figure 9-1: MITICA Mock-Up mesh in modal analysis.

9.3. Boundary conditions

The nominal operation condition of the MITICA Mock-Up BS would require a 50 mm displacement, at the bottom interface with the tilting support, equivalent to a 1° tilt around the

top hinges connecting the structure to the support beam. However, to actually identify the natural frequencies of the structure, without the influence of fixed boundary conditions, the tilting of the system is set to 0 mm. Thus, the boundary conditions of the model are the same of the previous static structural analysis, changing only the imposed displacements to 0 mm near the tilting system.

In the modal analysis setting, the number of modes set to be found is chosen to be of 20 since it is already known that these modes are found inside the range close to the frequencies of Padova's seismic activity [42].

9.4. Results and postprocessing

There are 2 major results of interest obtained by this simulation. The first one is the determination of the natural frequencies of the structure. The second is the evaluation of the participation factor of each of them, to determine which one is responsible for higher mass displacement. These can then be compared with the results obtained using the real PEEK material. The natural frequencies with the equivalent PEEK material are listed in Table 20.

Mode	Frequency [Hz]	Mode	Frequency [Hz]
1	4.1078	11	17.169
2	6.9463	12	18.661
3	9.1994	13	19.034
4	9.6296	14	21.681
5	12.79	15	21.872
6	12.816	16	23.07
7	14.235	17	24.124
8	14.831	18	25.442
9	14.849	19	27.328
10	16.357	20	27.979

Table 20: natural frequencies of MITICA Mock-Up electrodes model using equivalent PEEK material.

Not all frequencies have the same importance, thus the participation factor helps to determine which frequency mode prevails over the others. For each of these frequencies the participation factor is individually determined for all translations and rotations according to the global reference frame shown in Figure 9-1. Among these, the translation in z direction (gravity direction) is more critical because it corresponds to the highest accelerations and directly adds up to gravitational loads. Therefore, the structure's integrity is majorly put to test where resonant vibrations are added to the standard earth acceleration.

As an example, the participation factor in z direction, together with the effective mass and ratio between effective mass and total mass are shown in Table 21.

		z direction			
Mode	Frequency [Hz]	Partic. Factor	Normalized to max value	Effective Mass	Effective Mass / Total Mass
1	4.1078	1.32E-03	0.001584	1.74E-06	3.45E-07
2	6.94629	0.71568	0.858365	0.512192	0.101476
3	9.19936	1.90E-02	0.022815	3.62E-04	7.17E-05
4	9.62957	-0.77602	0.930745	0.602214	0.119311
5	12.7902	2.63E-02	0.031512	6.90E-04	1.37E-04
6	12.8157	-2.39E-03	0.002869	5.72E-06	1.13E-06
7	14.2349	-7.02E-03	0.008422	4.93E-05	9.77E-06
8	14.8307	-0.63073	0.756489	0.397827	7.88E-02
9	14.8494	-0.18828	0.225816	3.54E-02	7.02E-03
10	16.3566	-0.21397	0.256627	4.58E-02	9.07E-03
11	17.1688	0.83377	1	0.695167	0.137727
12	18.6611	-9.15E-04	0.001097	8.37E-07	1.66E-07
13	19.0345	-1.22E-03	0.001468	1.50E-06	2.97E-07
14	21.681	1.79E-03	0.002141	3.19E-06	6.32E-07
15	21.8715	-1.10E-02	0.013203	1.21E-04	2.40E-05
16	23.0698	-0.31826	0.381716	0.101291	2.01E-02
17	24.1241	-3.94E-02	0.04731	1.56E-03	3.08E-04
18	25.4423	-5.52E-03	0.006617	3.04E-05	6.03E-06
19	27.3281	-0.1232	0.147766	1.52E-02	3.01E-03
20	27.9786	1.60E-02	0.019244	2.57E-04	5.10E-05

Table 21: z participation factor of relevant modes for MITICA Mock-Up electrodes model using equivalent PEEK material.

The modes with participation factor larger than 0.5 are considered relevant and are highlighted. The frequency with the highest participation factor (yellow) is the **main natural frequency of the structure**, in this case 17.1688 Hz.

It should be noted that some of the low-frequency modes (orange) correspond to high participation factors and could cause high vertical accelerations in case of seismic activity. However, even if the MITICA Mock-Up is installed at PRIMA site of the Consorzio RFX (Padua), the Floor Response Spectrum (FRS) of ITER building is used. This FRS contains greater accelerations than the PRIMA site, making it more conservative. [39] For these reasons, these low-frequency modes are not taken into consideration as an already very conservative hypothesis is used for the design.

Furthermore, it should also be noted that the cumulative sum of the 20 effective mass over total mass ratios yields a value of around 50%. Therefore, there is a high chance that half of the

structure's modes are still not identified. However, these additional modes are all at greater frequency value and therefore correspond to low values of seismic acceleration, which are for such reason not of interest.

The structure's response for the main frequency of this structure is depicted in Figure 9-2, showing the deformation caused by this vibrational mode.

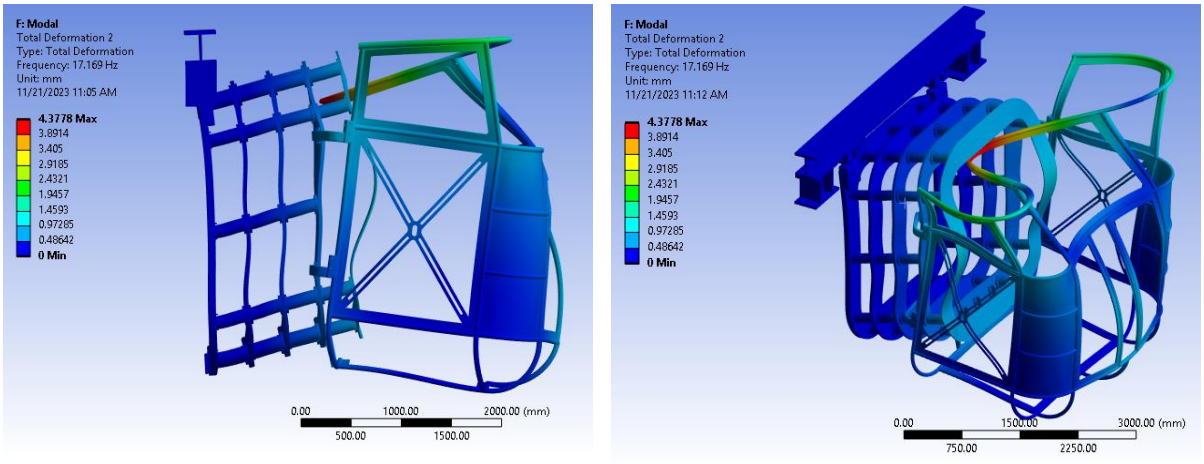

Figure 9-2: deformation caused by main natural frequency of MITICA Mock-Up electrodes model with equivalent PEEK material.

9.5. Result discussion

The comparison between the main frequencies individually obtained in all directions and rotations between the model run with real and equivalent PEEK is summarised in the following:

- x direction: real PEEK has 16.72 Hz, while equivalent PEEK has 16.36 Hz;
- y direction: real PEEK has 9.50 Hz, while equivalent PEEK has 9.20 Hz;
- z direction: real PEEK has 18.02 Hz, while equivalent PEEK has 17.17 Hz;
- rotational x: real PEEK has 9.50 Hz, while equivalent PEEK has 9.20 Hz;
- rotational y: real PEEK has 7.12 Hz, while equivalent PEEK has 6.95 Hz;
- rotational z: real PEEK has 4.18 Hz, while equivalent PEEK has 4.11 Hz.

In all cases, no difference is bigger than 0.9 Hz. Thus, in case of seismic activity, the structure's integrity is not threatened and the seismic verifications of the original model are still valid. Moreover, it should be noted that the decrease of the PEEK material's stiffness caused a decrease of all main frequency modes of the structure as described in chapter 4.4. Additionally, one can compare in more detail the z direction differences in terms of participation factors, effective mass, and effective mass over total mass in the Appendix F.

9.6. Conclusion about the modal analysis of the MITICA Mock-Up electrodes

The Modal analysis of the MITICA Mock-Up electrodes model run using the equivalent and the real PEEK material revealed that:

- The main frequency of the structure remains the mode 11 of 17.1688 Hz, being 4.74% lower than before;
- The presence of other low frequency modes with high participation factor can be neglected due to the conservative FRS approached used.

Thus, it is possible to conclude that the consequences of the stiffness discrepancy between the numerical and experimental data does not threaten the structure's integrity by causing an excessive total deformation of the cantilevered structure or a decreased value of natural frequencies of the structure.

10. Detailed M14 screw-helicoil sub model

10.1. Objective

The aim of this sub model is to verify if overall stiffness of the PEEK insulator model is overestimated when the threaded surfaces of the M14 screw and helicoil are neglected. This would explain the reason why the simplified PEEK insulator model is stiffer compared to the real-case PEEK insulator model.

In this detailed model, both accurate and simplified M14 screws and helicoils are modelled and then subjected to the same boundary conditions. The reaction forces estimated at the contact between the elements connected by the screw and helicoils are then compared.

10.2. Geometry and mesh

The geometry of the model involves a real-case model and a simplified case model. The former includes the actual geometry of M14 screws and M14 helicoil insert according to the ISO standard 724:2023(E) [54] (directly imported from existing libraries [55]), whereas the real PEEK bulk material, which hosts screw and helicoil, is obtained as the complementary geometry of the outer part of the helicoil's insert. The latter uses simplified geometries and dimensions following the modelling used in the real-case PEEK insulator model as shown in Figure 10-1.

Some other adjustments are made to avoid possible errors during simulation. In case of the real-case model, gaps between the imported screw and helicoil geometries are filled to avoid their presence which would be responsible for contact errors. Conversely, for the simplified model, the screw's diameter is the same as the resistive diameter of the M14 screw.

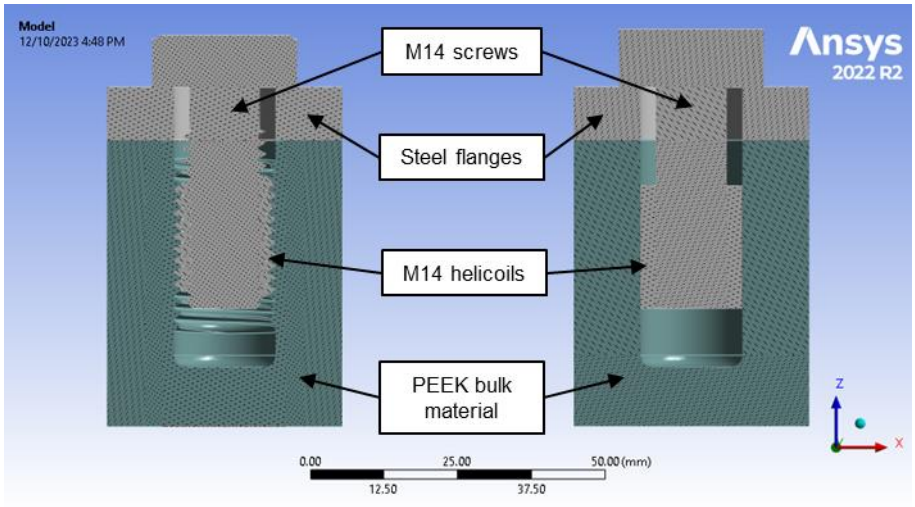

Figure 10-1: sectioned geometry of M14 screw-helicoil-PEEK sub-model (color based on materials).

In both cases a steel flange surface is added on top of the PEEK bulk material to better simulate the real case scenario in which the stainless-steel flanges are connected to the PEEK insulator using M14 screws and helicoil. For this reason, the screws are increased in length by the same amount of the flange's thickness.

The generation of the mesh is more critical in the real-case scenario part, which includes complex geometry bodies in contact with each other, requiring smaller elements and contact meshing.

The general element size is set to 2 mm, but more detailed body sizing and face sizing conditions are used to accurately follow the nominal geometry of the real-case M14 screw-helicoil. These mesh sizing functions range from 0.7 mm to 5 mm.

An additional important step that improves the mesh efficiency is the separation of regions having complex geometry from simpler ones. In the simplified M14 screw-helicoil sub model, the head of the M14 screw and the bottom part of the PEEK bulk material contain sharp edges or fillets, making its meshing more critical. Whereas, for the real-case M14 screw-helicoil sub model, the PEEK bulk material is divided into 3 hollow cylinders connected to each other. The final sectioned mesh is shown in Figure 10-2.

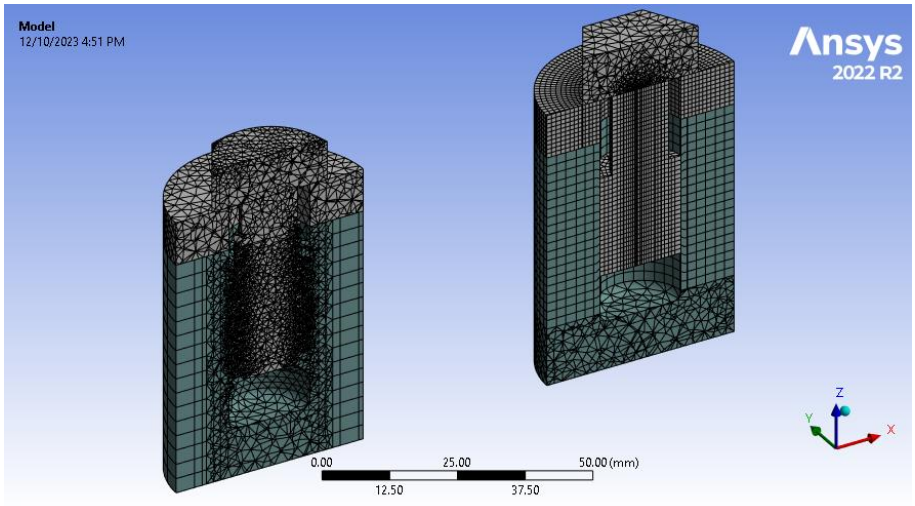

Figure 10-2: sectioned mesh of real-case (left) and simplified (right) M14 screw-helicoil model.

10.3. Boundary conditions

The first type of boundary condition concerns the contacts between different parts of the sub-model, which involve the use of specific contact parameters. In case of the real-case screw-helicoil sub model, frictional contact type with friction coefficient of 0.2 is used and the involved surfaces are between:

- screw's external threaded surface with internal threaded helicoil's area;
- helicoil's external threaded surface with PEEK bulk material's threaded area;
- screw's bottom head surfaces and flange's top surface.

On the other hand, for the simplified screw-helicoil model, both bonded and frictional contact type are used, which are specified in the following involved surfaces:

- bonded between screw's external surface and helicoil's internal area;
- bonded between helicoil's external surface and PEEK bulk material's internal area;
- frictional between screw's bottom head surface and flange's top surface.

Another boundary condition concerns the bolt pretension of 20 kN, this condition is set for both real and simplified sub models as shown in red in Figure 10-3. This simulates the tightening of the screws before the actual tensile force is imposed.

Furthermore, fixed supports are set to the outer surface of the PEEK bulk material. This type of constraint is preferred compared to cylindrical supports because it does not lead to a simulation error during the solver's operation. In the meantime, 2 remote displacements of 4 are imposed mm in positive z direction on the upper surface of both real and simplified screws as shown in yellow in Figure 10-3.

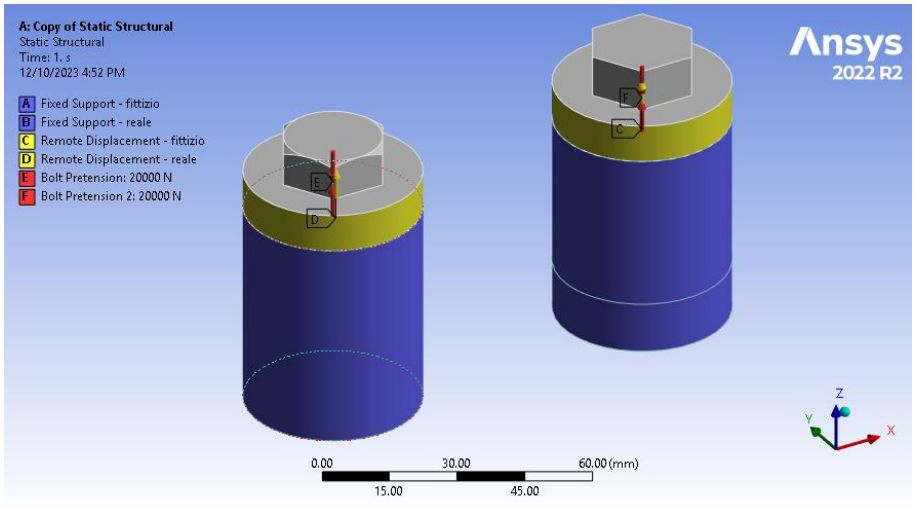

Figure 10-3: boundary conditions for M14 screw-helicoil sub model.

10.4. Results and postprocessing

The major result of interest is the reaction force set along the upper part of both screws' axis of symmetry. Due to the asymmetry of the real-case screw's geometry, it is expected that greater components of the force reaction act in directions different from the vertical z axis. The tabular data of the results is shown in Table 22, while the visual representation is shown in Figure 10-4.

	Force reaction (X)	Force reaction (Y)	Force reaction (Z)	Force reaction (Total)
simplified sub model	0	0	59785	59785
real-case sub model	906.97	-406.6	41127	41139

Table 22: force reaction results of screw-helicoil sub model.

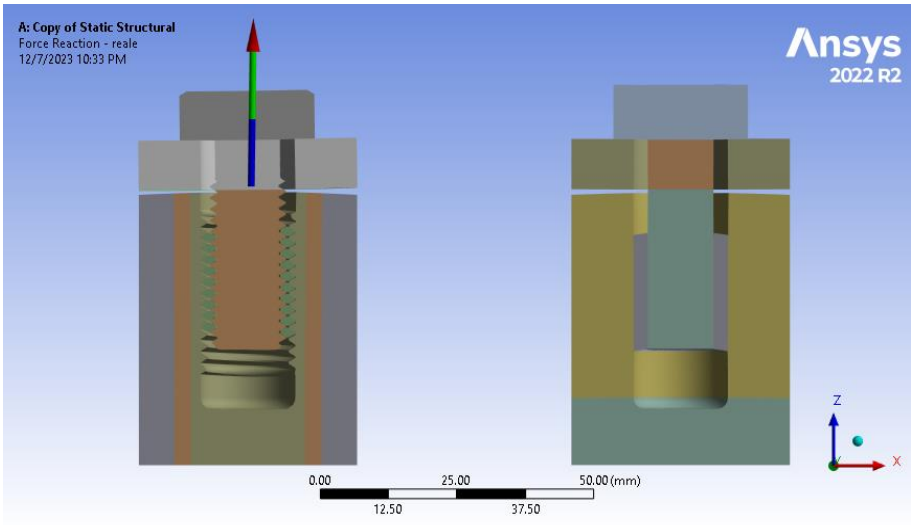

Figure 10-4: force reaction of real-case screw-helicoil sub model (color based on bodies).

The asymmetry of the real-case sub model is also noted in the equivalent stress distribution acting on the model as shown in Figure 10-5. The 4 mm displacement generates stresses which are by far greater than the yielding stress of 210 MPa of the AISI 304L material, of which both the screw and the helicoil are made of. However, since the model is assumed to be a linear static structural simulation, it still gives a general indication of the most stressed zones of screws, helicoils and PEEK bulk material.

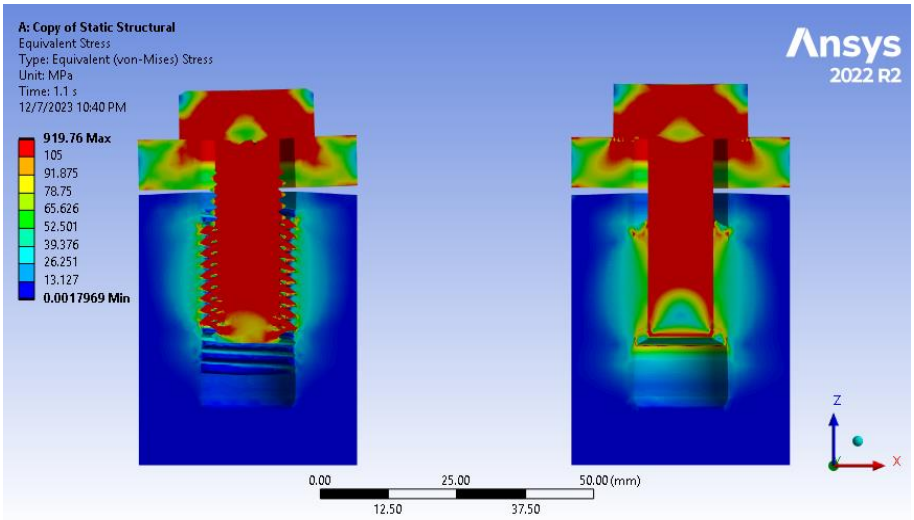

Figure 10-5: equivalent stress distribution of screw-helicoil sub model.

10.1. Results discussion

By examining the inner hollow cylinder of the real-case PEEK bulk material, it is possible to see that the 4 mm remote displacements is just enough to generate stress close to the yielding point on the threaded PEEK surfaces if the real PEEK material is used, as shown in Figure 10-6. The most stressed area is the first round of the helicoil thread, starting from the bottom. Thus, it is likely that local plastic deformation occurs in the threaded surface of the PEEK material which gradually moves from the bottom threads to the upper ones. The experimental validation done allows for visual inspection that shows similar behavior as shown in the figure below.

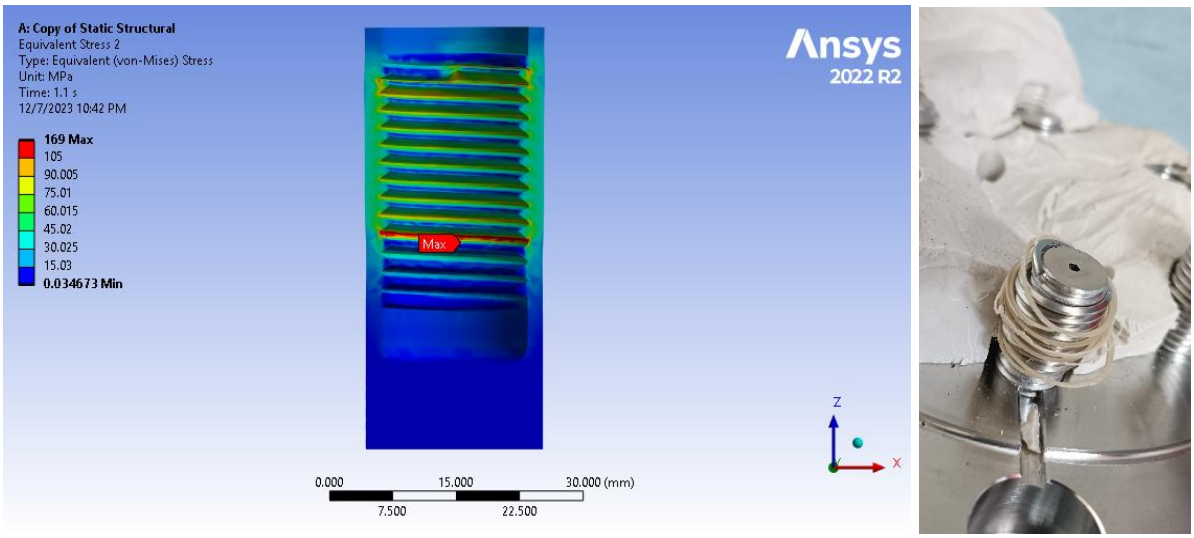

Figure 10-6: equivalent stress of PEEK bulk material of real-case screw-helicoil sub model (left) and local plastic deformation occurred during experimental validation of PEEK insulator.

Moreover, there is 31.2% result difference between the reaction force measured by the real-case and simplified model, as shown in table Table 23. Hence, the simplified modelling of the screw-helicoil system adopted for the MITICA Mock-Up model is stiffer than the real case scenario. This could make the use of simplified geometry and of bonded contact type a not fully conservative decision.

	Simplified	Real	abs. err. [N]	rel. err. %
Force reaction (Total) [N]	59785	41139	18646	31.2

Table 23: absolute and relative error between reaction forces of real-case and simplified screw-helicoil sub model.

However, the simplified modelling has great advantages in terms of computational efficiency and it would be inefficient to run the real-case PEEK insulator tensile test simulation using real-case screw-helicoil connections. Therefore, it seems more reasonable to use again the equivalent material technique, this time to the simplified helicoil to obtained similar reaction forces between the real and simplified screw-helicoil sub models.

Due to the hollow cylindrical shape of the simplified helicoil model and due to the presence of intense shear forces generated by the vertical remote displacement, changing the elastic modulus of the AISI 304L material is not effective at decreasing its stiffness. The way adopted to efficiently decrease the stiffness of the simplified model is to decrease the shear modulus while keeping the same bulk modulus as the original material. This is done by fixing the bulk modulus value and increasing the Poisson's ratio. This equivalent material AISI 304L material is defined in Table 24.

	AISI 304L				
	Temperature [C°]	Elastic modulus [Gpa]	poisson's ratio	Bulk modulus [GPa]	Shear modulus [GPa]
real	20	199.96	0.3	166.64	76.91
virtual	20	2.60	0.497	166.64	0.87

Table 24: comparison of real and equivalent AISI 304L for M14 helicoils.

10.2. Conclusion about the Structural Analysis of the M14 screw-helicoil sub-model

The Static Structural Analysis of the M14 screw-helicoil sub-model revealed that:

- The real-case modelling of the screw-helicoil connection is less stiff compared to the simplified one as obtained for the real and simplified PEEK insulator model for the tensile test;
- The reaction force of the simplified scenario is 31.2% greater than the real-case scenario;
- The most stressed part of the PEEK bulk material is the thread in contact with the helicoil's lowest thread, generating local plasticity which gradually moves to all upper threads;
- The use of an equivalent AISI 304L material with lower shear modulus can generate the same reaction force in the simplified scenario model.

Therefore the numerical sub model of the screw-helicoil connection allowed to demonstrate the increased stiffness caused by simplified modelling of such connection and the definition of an equivalent AISI 304L material which can be used for more accurate modelling of the PEEK insulator tensile test modelling, done in the next section.

11. Update of real-case PEEK insulator model

11.1. Objective

The objective of the update of the real-case PEEK insulator model is to verify whether the equivalent AISI 304L material generates force-displacement results that better explain the experimental data of the PEEK insulator tensile test.

To do so, the helicoil's material of the real-case PEEK insulator model is set to this equivalent AISI 304L material. Then the simulation is run again so as to compare the new values with the original ones.

11.2. Model set-up

The same model is used as described in chapter 6, using the same geometry and meshing techniques. The main difference of this model is the usage of a symmetry to reduce the computational time of the simulation. In fact, all constraints like bolt pretensions and remote displacements are symmetric with respect to the x-z plane of the global coordinate frame shown in Figure 11-1.

For completeness the remote displacement imposed to the whole of the upper connecting element is set to 1 mm.

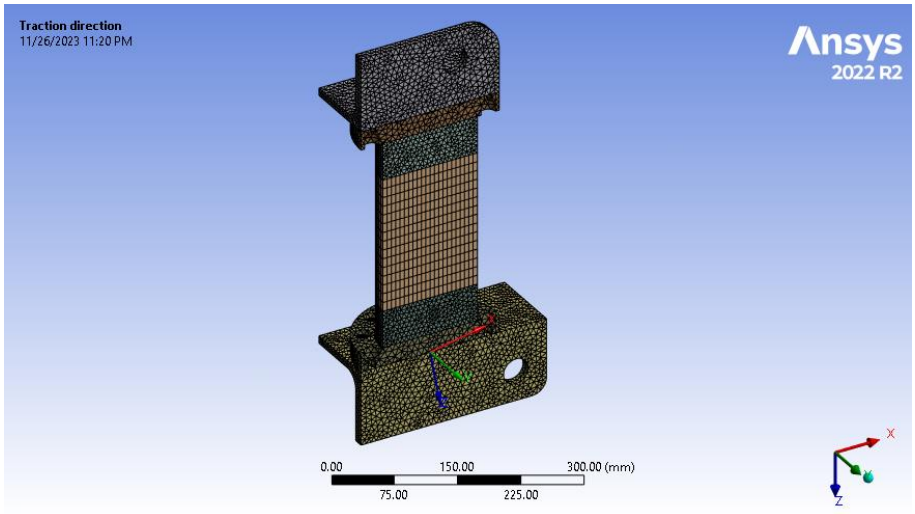

Figure 11-1: geometry and mesh of the updated real-case PEEK insulator model.

11.3. Results and post-processing

The result of interest is the evaluation of the reaction force acting along the z axis of the "Traction direction" reference frame in case of the use of real AISI 304L material and its equivalent version applied on the simplified hollow cylinder shaped helicoils. The tabular results are summarized in Table 25 and the visual representation of the reaction force is shown in Figure 11-2.

	Force reaction (X) [N]	Force reaction (Y) [N]	Force reaction (Z) [N]	Force reaction (Total) [N]
real AISI 304L	-1.078	-2354.8	-30518	30608
equivalent AISI 304L	-1.016	-2355.4	-29032	29118

Table 25: reaction force (doubled due to symmetry of model) comparison of real-case PEEK insulator model with the use of real and equivalent AISI 304L for helicoils.

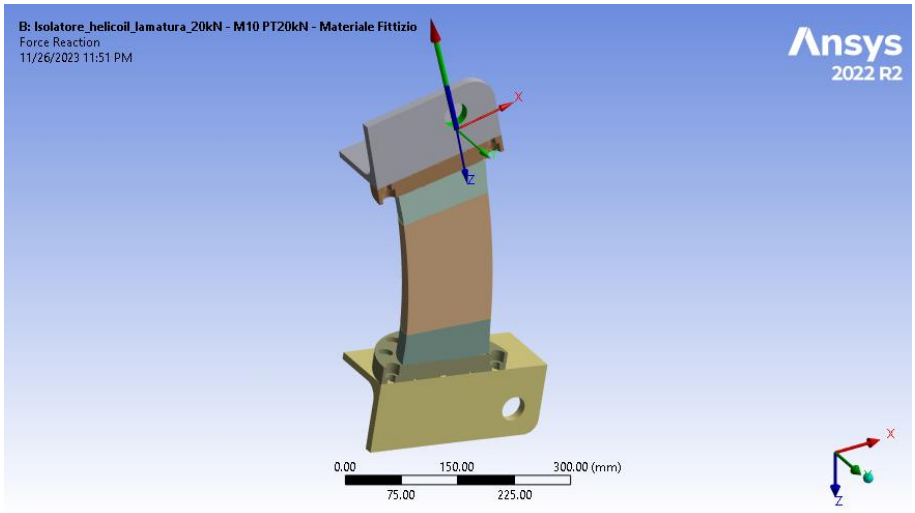

Figure 11-2: reaction force of updated PEEK insulator model for tensile test.

11.4. Results discussion and conclusion

The adoption of the equivalent AISI 304L generates little improvement. The values displayed in Table 25 shows the reaction force acting on the total PEEK insulator. Therefore, the absolute difference between the model using the real and equivalent AISI 304L material for helicoils is of 1490 N, which corresponds to a 4.9% decrease in stiffness. This value is still far from the 18873 N value which should be obtained after 1 mm displacement, but it shows that change of a small component's material like the helicoils does not dramatically affect the outcome of the simulation even if it represents the connecting element between the insulator and the flanges.

Therefore, other solutions should be investigated to find an effective and efficient way to model the helicoil component in a simple and effective way as there is still room for improvement.

12. Conclusions

The work of this thesis concerned the validation of the structural design of the MITICA Beam Source Mock-Up electrodes and was carried out during the months of March until December 2023 at Consorzio RFX, under the supervision of Prof. Chitarin Giuseppe and Dr. Denizeau Sylvestre.

The work included both experimental tests on specific structural components (PEEK post-insulator) and the development of FEM models for numerical analyses of the structure during normal operation conditions and of the components during the tests.

The experimental tests of the PEEK post-insulator were a success, since they allowed to demonstrate that the structure of the MITICA Beam Source Mock-Up is compliant with the necessary mechanical requirements and enabled the assembly of the electrodes and the commencement of the electrical insulation tests.

The experimental set up used was based on the one previously used for the test on Alumina post-insulators, even if the loads acting on the PEEK post-insulators are shear-dominant instead of traction-dominant. Unexpectedly, the experimental data showed that the PEEK insulator can also exhibit a fragile macroscopic behaviour, even though the material reaches a 40% deformation rate. Besides plastic deformability, and differently from Alumina, also a hysteresis behavior is present, as indicated by the difference in trajectory between the loading and unloading curves which still share the beginning (origin) and end (final cyclic load) points.

During the thesis, seven specific FEM models have been developed for the analysis of the structure during operation and for interpreting the results of the experimental tests. The results of the numerical models are in fairly good agreement with the experimental ones concerning the expected stress distribution and the mechanism of failure propagation in the PEEK post-insulators.

However the experimental tests indicate lower stiffness compared to what could be expected on the basis of numerical models the same tensile test. This discrepancy might indicate that stress concentration is actually lower than expected, but also results in an underestimation of deformations, which, in some cases, can be critical from an electric insulation point of view. For this reason, the numerical model of the simplified PEEK insulator for tensile test simulation was calibrated to better match the numerical model. The force-displacement slope of 18873 N/mm allowed to identify with a 2% relative error that the PEEK insulator remains in pure elastic range until the load of 24658 N is reached. Afterwards, non-negligible plastic work is absorbed by the PEEK material.

The calibration of such model determined a equivalent PEEK material, whose elastic modulus is changed from 3850 MPa to 2670 MPa. Re-running the static structural simulation and the modal analysis of the complete MITICA Mock-Up model revealed no significant difference in the total deformation and new frequency modes of the structure. Therefore, no risks are present and the numerical design is validated.

Moreover, the component's fracture has been further investigated using both visual inspection and explicit dynamics & static structural modelling, leading to good correspondence between numerical and experimental results. It is likely that the fracture of the PEEK insulator initiated by the presence of local plastic deformation starting from the bottom thread of the M14 helicoils of the two most stresses M14 holes of the PEEK insulator. It then propagates to the upper threads and the fracture initiates still from the thread of the PEEK M14 hole in contact with the bottom thread of the helicoil since it remains the most stressed one.

Additionally, the sub model of the M14 screw-helicoil connection proved that the simplified modelling of such connection appears to be stiffer compared to the real-case model (reaction force of the upper screw's shank is reduced of 31.2%). Accordingly, an equivalent AISI 304L material for the simplified helicoil body has been defined to then be implemented in the real-case PEEK insulator model for the tensile test. Unfortunately, such equivalent material revealed not to be effective to simulate the tensile test. The force-displacement slope is reduced to a value 4.8% lower than in the previous simulation. Thus, different way of introducing a lower stiffness in the model should still has to be found.

Finally, future developments of the numerical models established could lead to better correlation between experimental and numerical modelling of the screw-helicoil model. This model could also be used to better investigate the behavior in case of the Alumina post-insulators, whose ceramic material can constitute an additional challenge to an effective simulation. This work not only addresses the current challenges but also lays the groundwork for future advancements for ongoing refinement in modelling techniques.

13. Table of figures

14. List of Tables

15. Appendix A

load-displacement graphs for all four samples

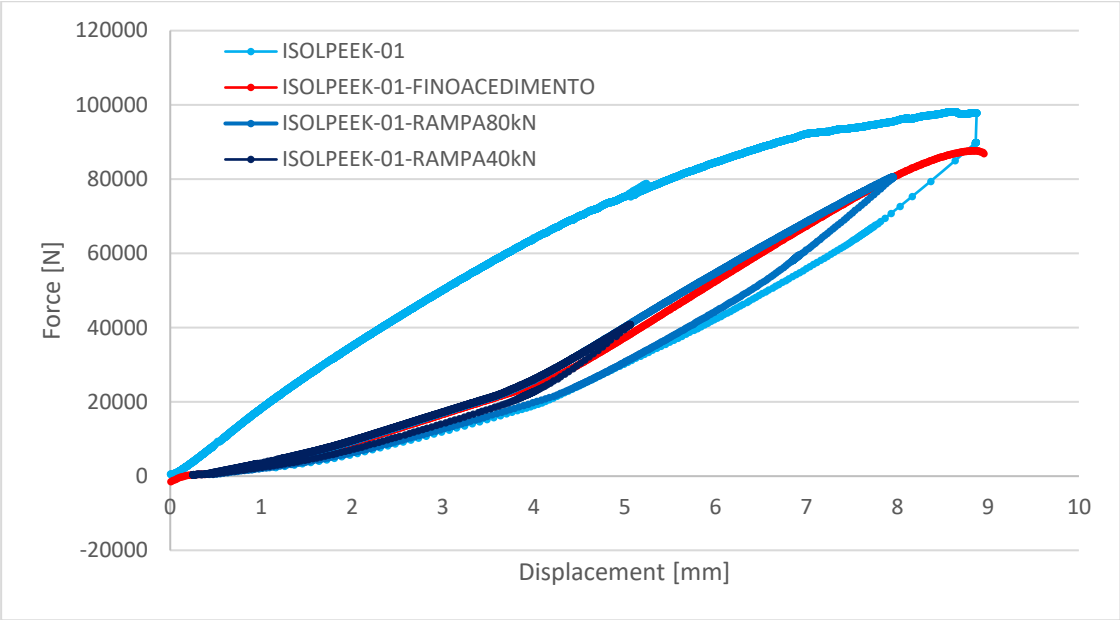

Figure A. 1: load-displacement curves for the first sample, with following order of execution ISOLPEEK-01, ISOLPEEK-01-RAMPA40kN, ISOLPEEK-01-RAMPA80kN, ISOLPEEK-01_FINOCACEDIMENTO.

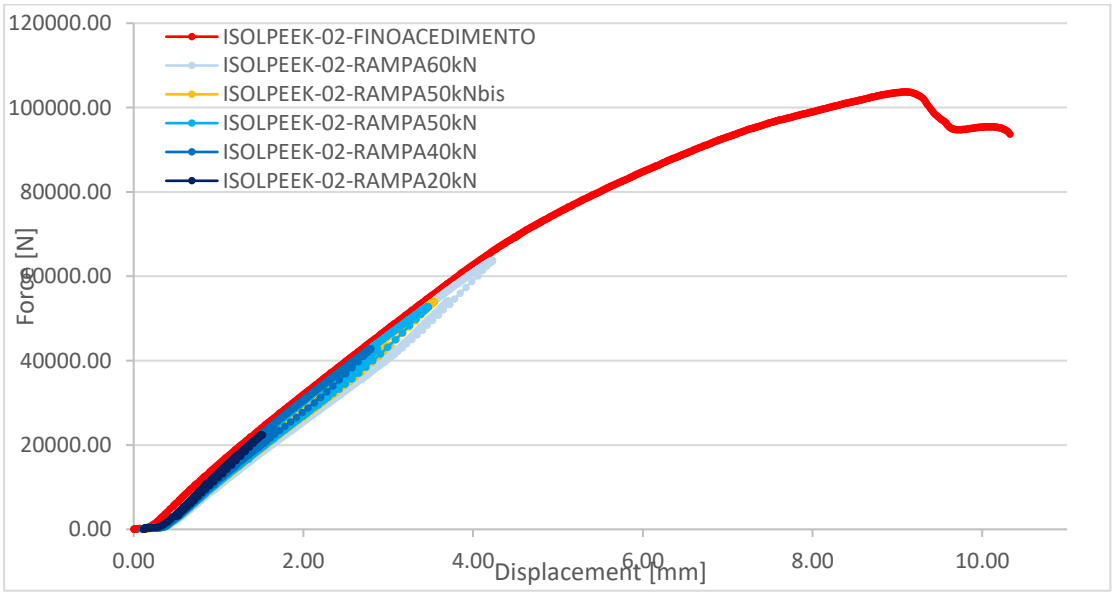

Figure A. 2: load-displacement curves for the second sample, with following order of execution ISOLPEEK-02-RAMPA20kN, ISOLPEEK-02-RAMPA40kN, ISOLPEEK-02-RAMPA50kN, ISOLPEEK-02-RAMPA50kNbis, ISOLPEEK-02-RAMPA60kN, ISOLPEEK-02-FINOACEDIMENTO.

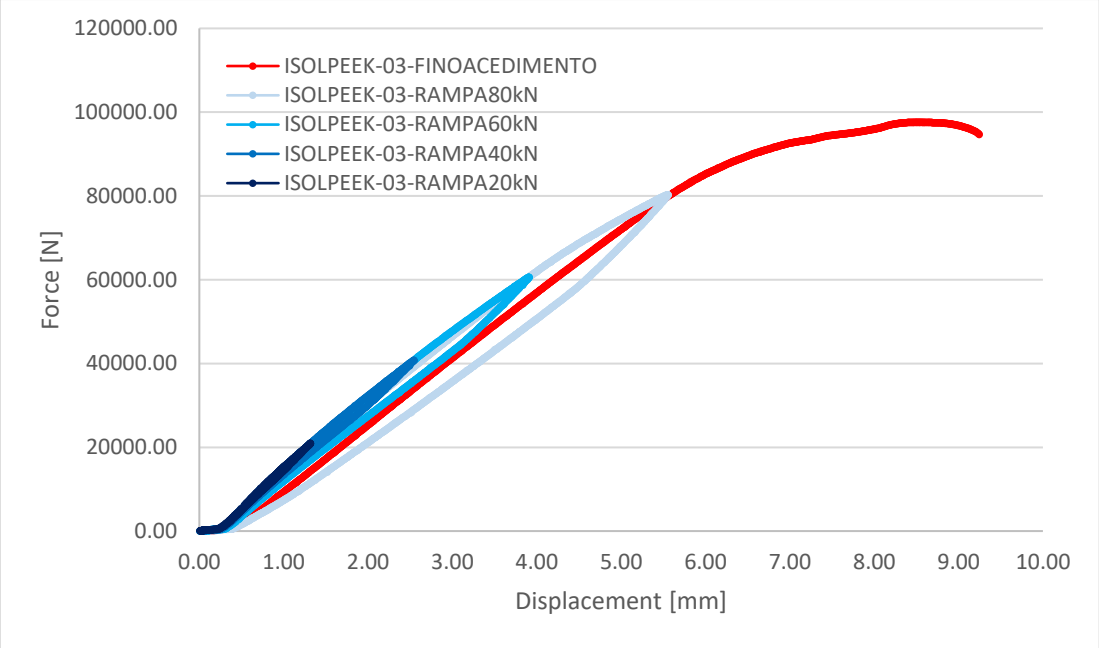

Figure A. 3: load-displacement curves for the third sample, with following order of execution ISOLPEEK-03-RAMPA20kN, ISOLPEEK-03-RAMPA40kN, ISOLPEEK-03-RAMPA60kN, ISOLPEEK-03-RAMPA80kN, ISOLPEEK-03-FINOACEDIMENTO.

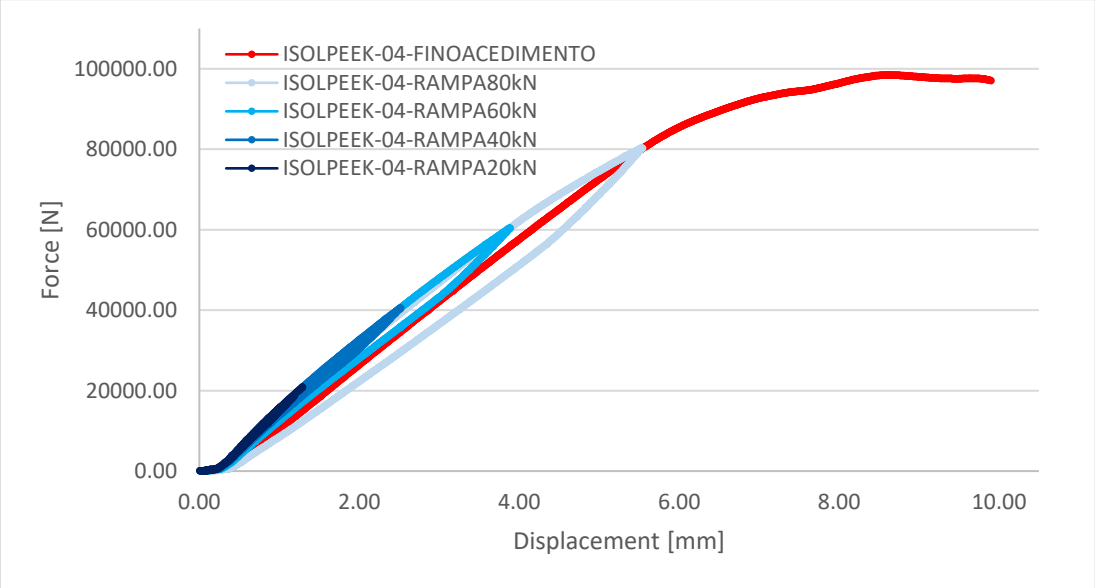

Figure A. 4: load-displacement curves for the fourth sample, with following order of execution ISOLPEEK-04-RAMPA20kN, ISOLPEEK-04-RAMPA40kN, ISOLPEEK-04-RAMPA60kN, ISOLPEEK-04-RAMPA80kN, ISOLPEEK-04-FINOACEDIMENTO.

16. Appendix B

Examples of discontinuities recorded during unloading phase of second PEEK insulator test

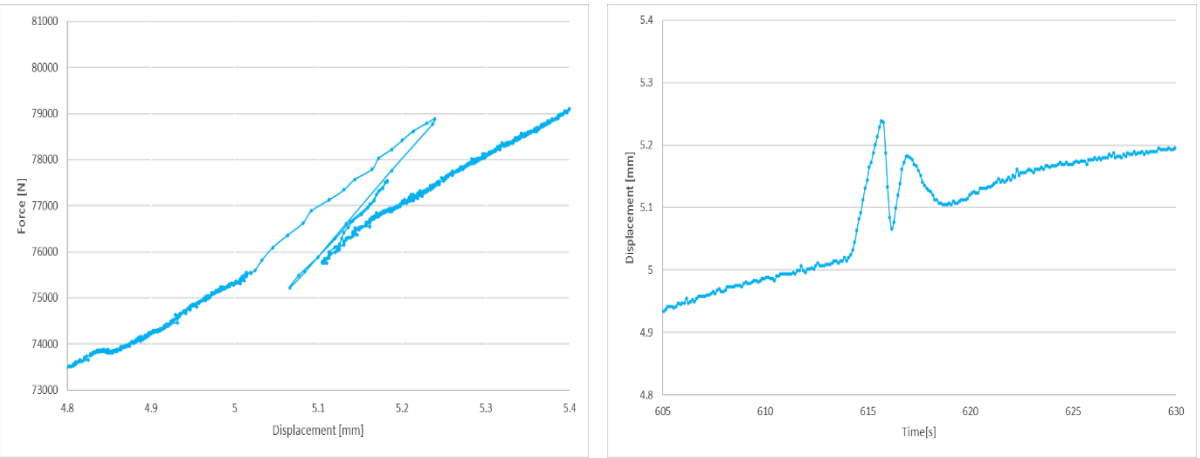

Figure B 1: ISOLPEEK-01, force-displacement graph at loading discontinuity (left) and displacement-time graph at loading discontinuity (right).

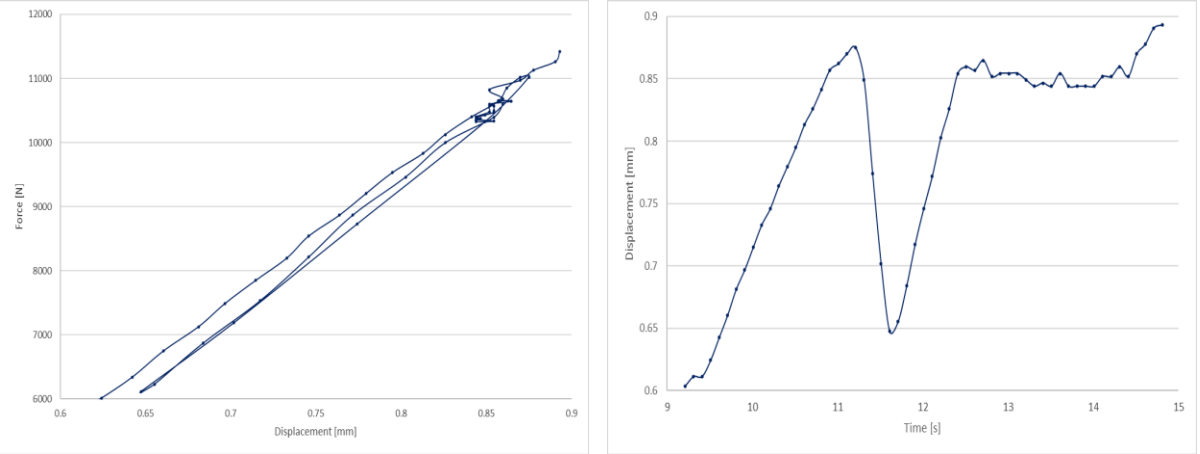

Figure B 2: ISOLPEEK-02-RAMPA20kN, load-displacement graph (left) and displacement-time graph (right) at discontinuity 1 of unloading phase for the second PEEK insulator.

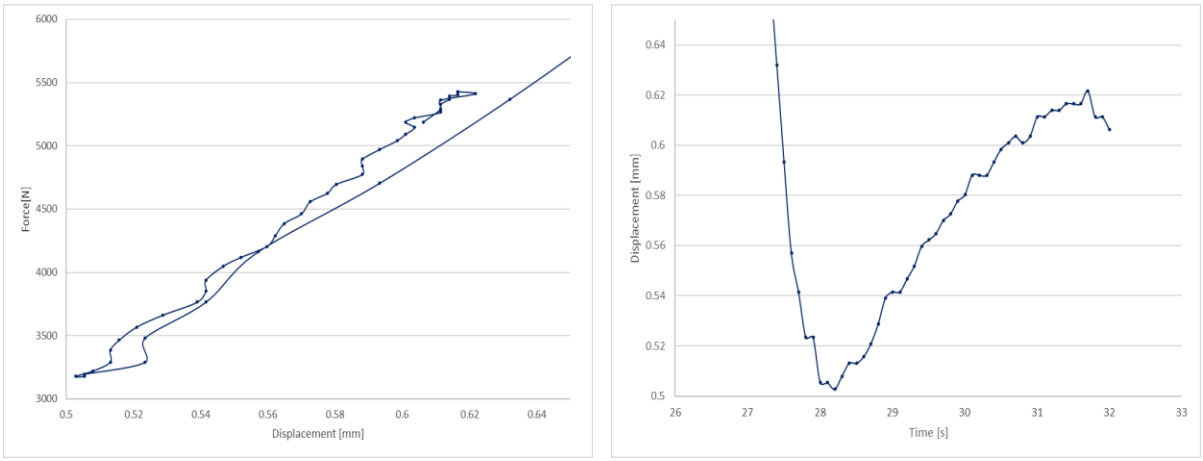

Figure B 3: ISOLPEEK-02-RAMPA20kN, load-displacement graph (left) and displacement-time graph (right) at discontinuity 2 of unloading phase for the second PEEK insulator.

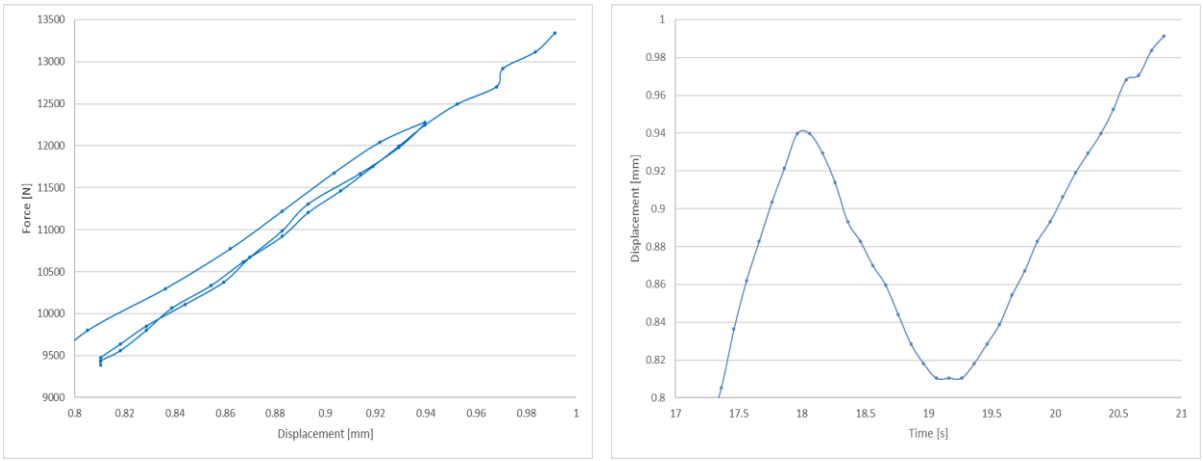

Figure B 4: ISOLPEEK-02-RAMPA40kN, load-displacement graph (left) and displacement-time graph (right) at discontinuity 1 of unloading phase for the second PEEK insulator.

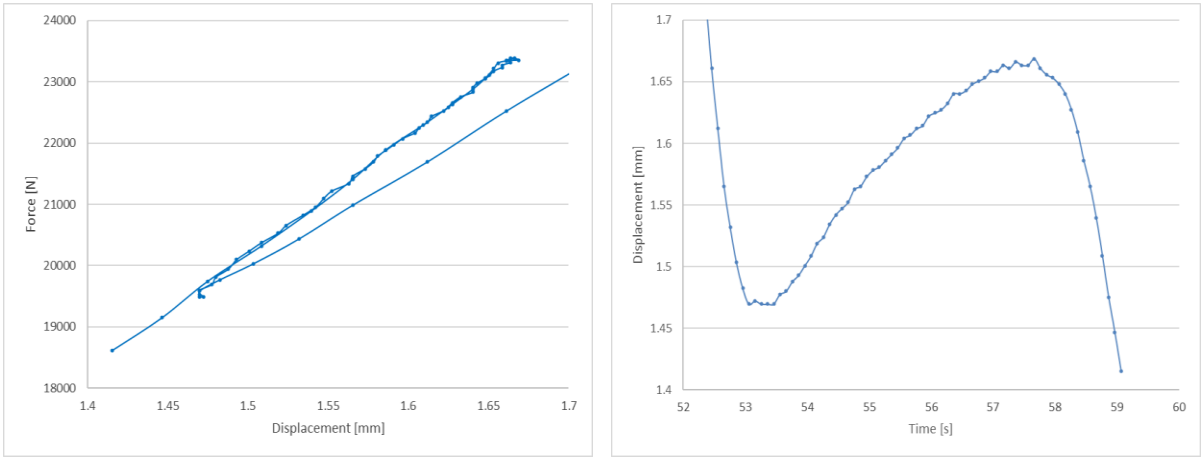

Figure B 5: ISOLPEEK-02-RAMPA40kN, load-displacement graph (left) and displacement-time graph (right) at discontinuity 2 of unloading phase for the second PEEK insulator.

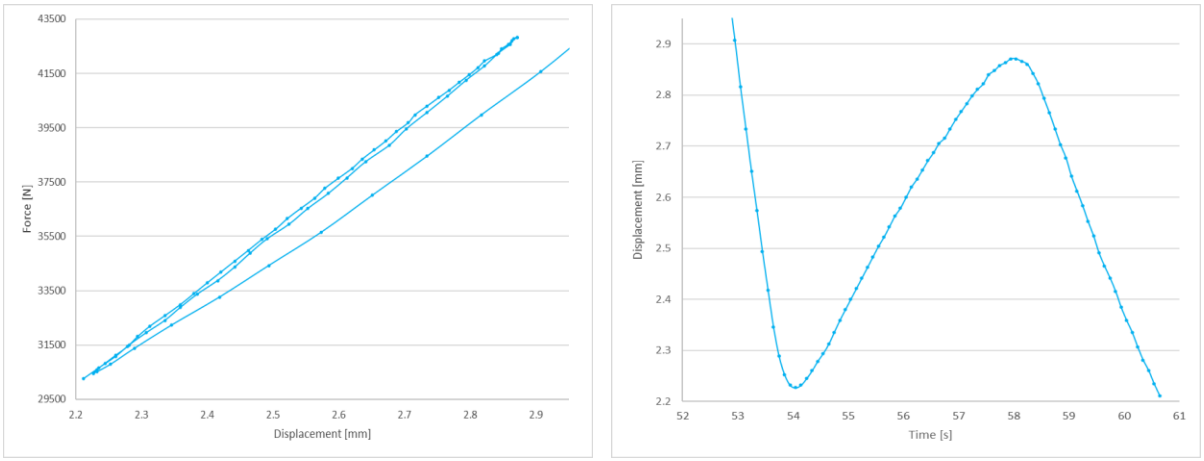

Figure B 6: ISOLPEEK-02-RAMPA50kN, load-displacement graph (left) and displacement-time graph (right) at discontinuity 1 of unloading phase for the second PEEK insulator.

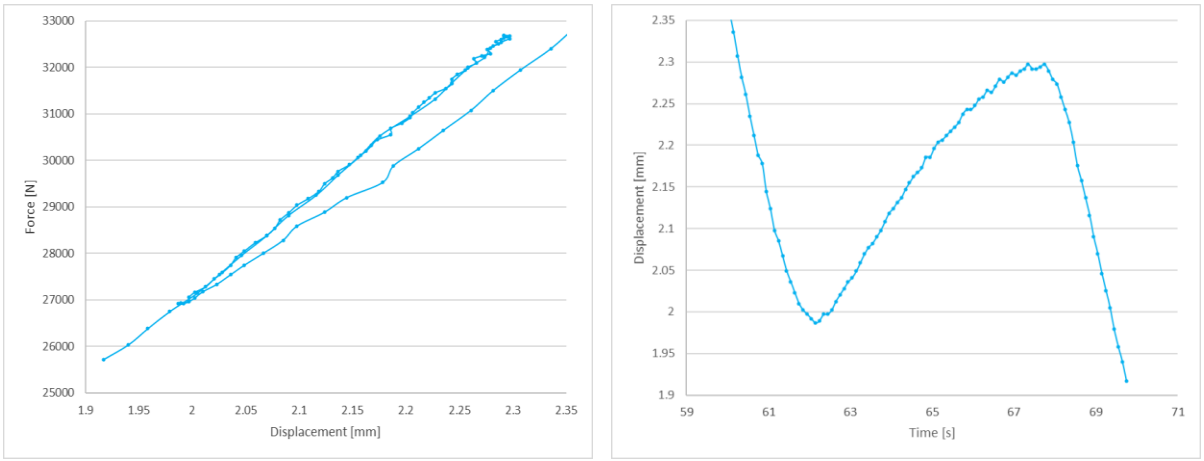

Figure B 7: ISOLPEEK-02-RAMPA50kN, load-displacement graph (left) and displacement-time graph (right) at discontinuity 2 of unloading phase for the second PEEK insulator.

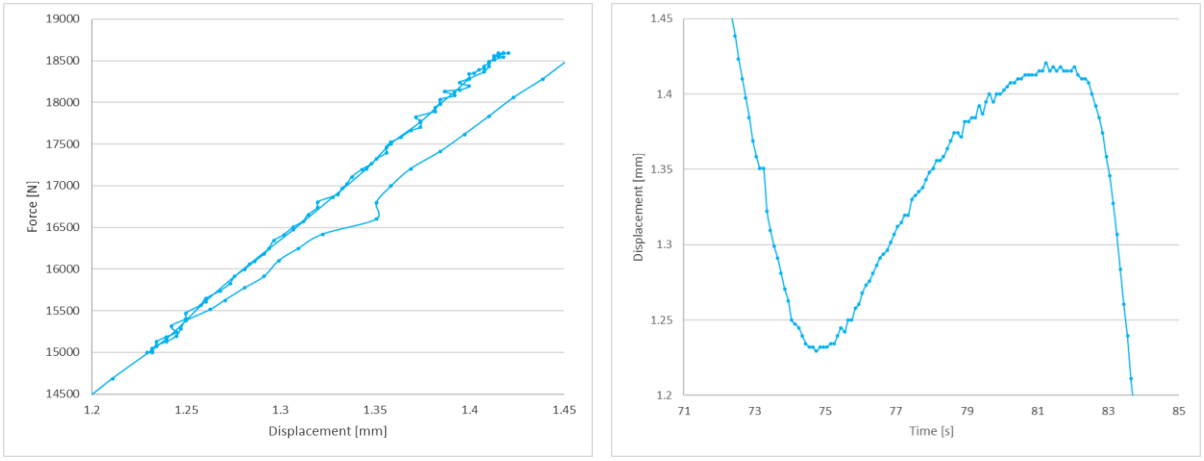

Figure B 8: ISOLPEEK-02-RAMPA50kN, load-displacement graph (left) and displacement-time graph (right) at discontinuity 3 of unloading phase for the second PEEK insulator.

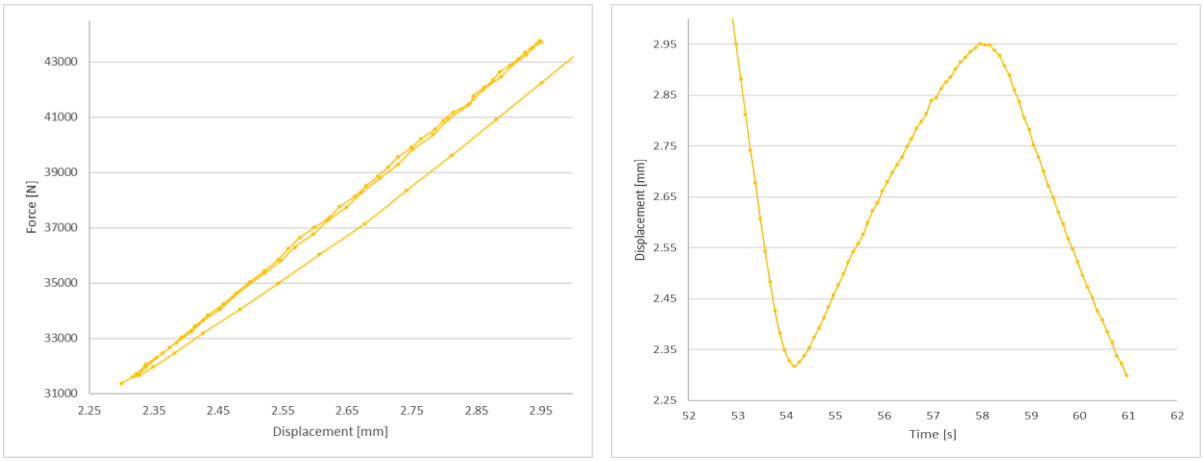

Figure B 9: ISOLPEEK-02-RAMPA50kNbis, load-displacement graph (left) and displacement-time graph (right) at discontinuity 1 of unloading phase for the second PEEK insulator.

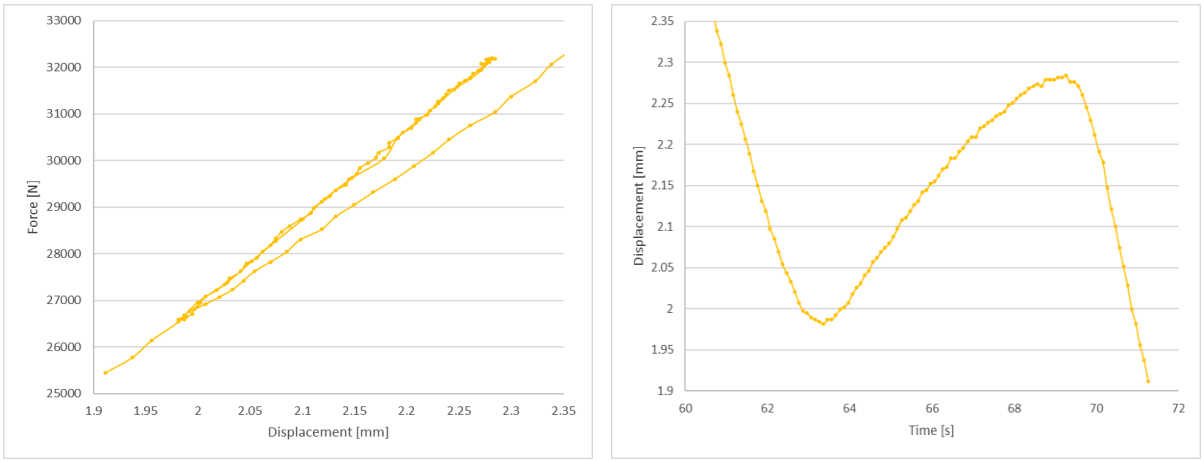

Figure B 10: ISOLPEEK-02-RAMPA50kNbis, load-displacement graph (left) and displacement-time graph (right) at discontinuity 2 of unloading phase for the second PEEK insulator.

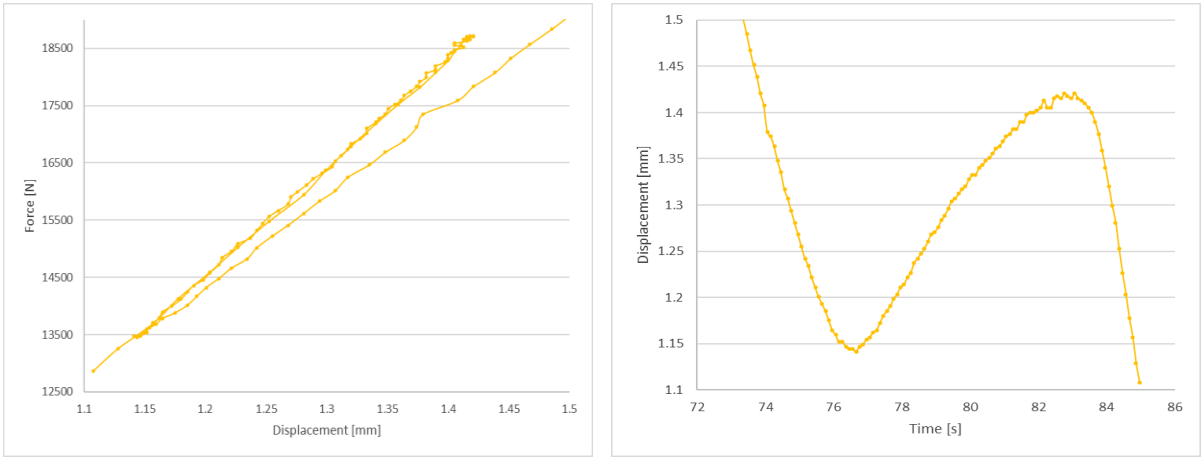

Figure B 11: ISOLPEEK-02-RAMPA50kNbis, load-displacement graph (left) and displacement-time graph (right) at discontinuity 3 of unloading phase for the second PEEK insulator.

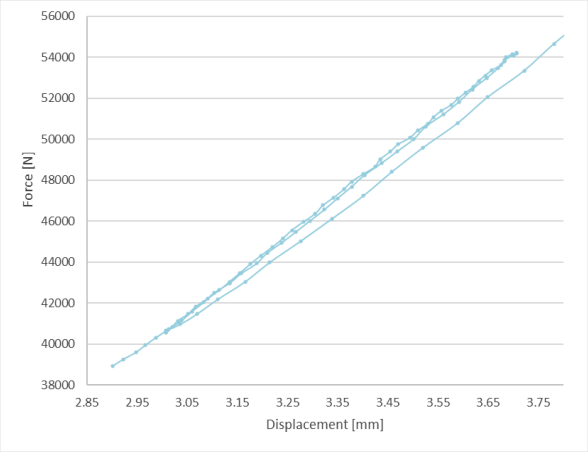

Figure B 12: ISOLPEEK-02-RAMPA60kN, load-displacement graph (left) and displacement-time graph (right) at discontinuity 1 of unloading phase for the second PEEK insulator.

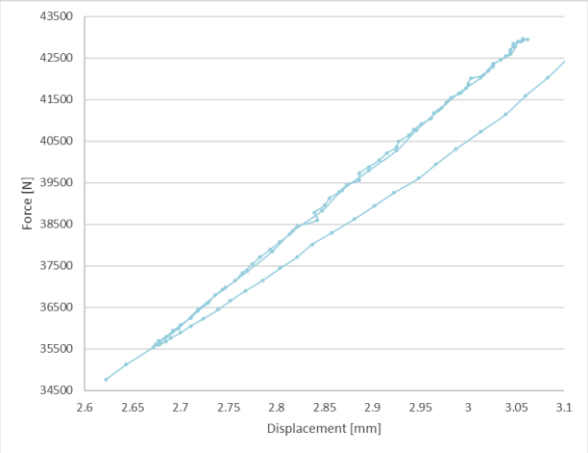

Figure B 13: ISOLPEEK-02-RAMPA60kN, load-displacement graph (left) and displacement-time graph (right) at discontinuity 2 of unloading phase for the second PEEK insulator.

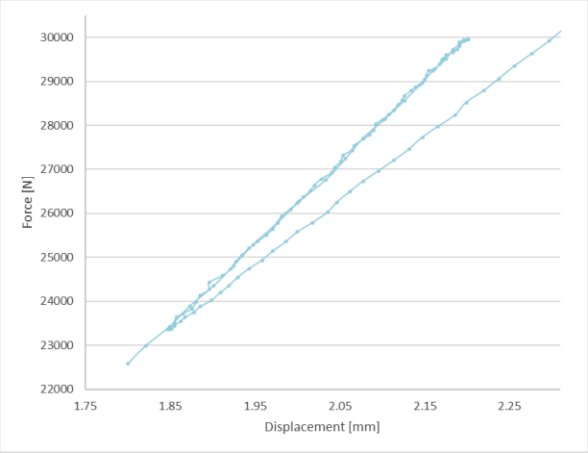

Figure B 14: ISOLPEEK-02-RAMPA60kN, load-displacement graph (left) and displacement-time graph (right) at discontinuity 3 of unloading phase for the second PEEK insulator.

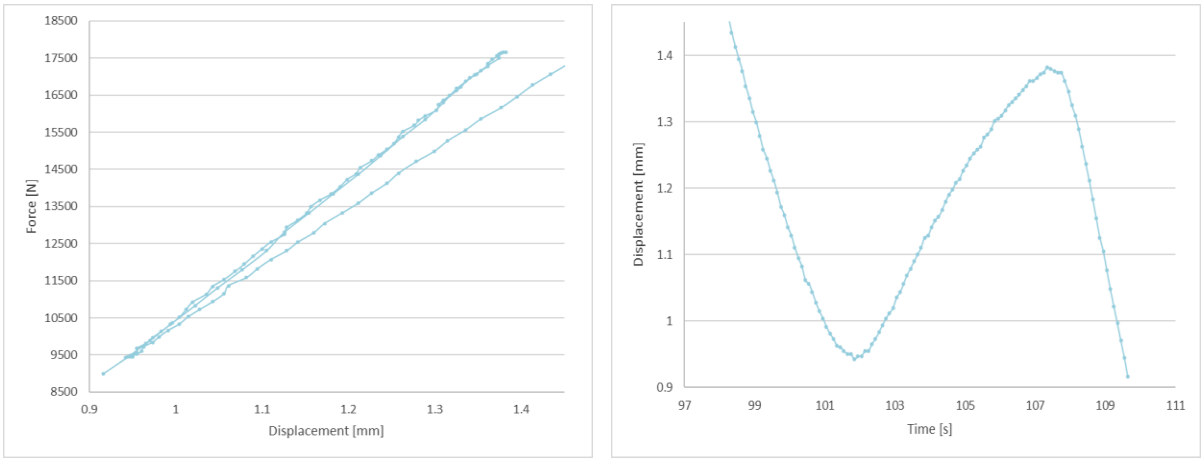

Figure B 15: ISOLPEEK-02-RAMPA60kN, load-displacement graph (left) and displacement-time graph (right) at discontinuity 4 of unloading phase for the second PEEK insulator.

17. Appendix C

Linear interpolation of experimental Force-Displacement curves

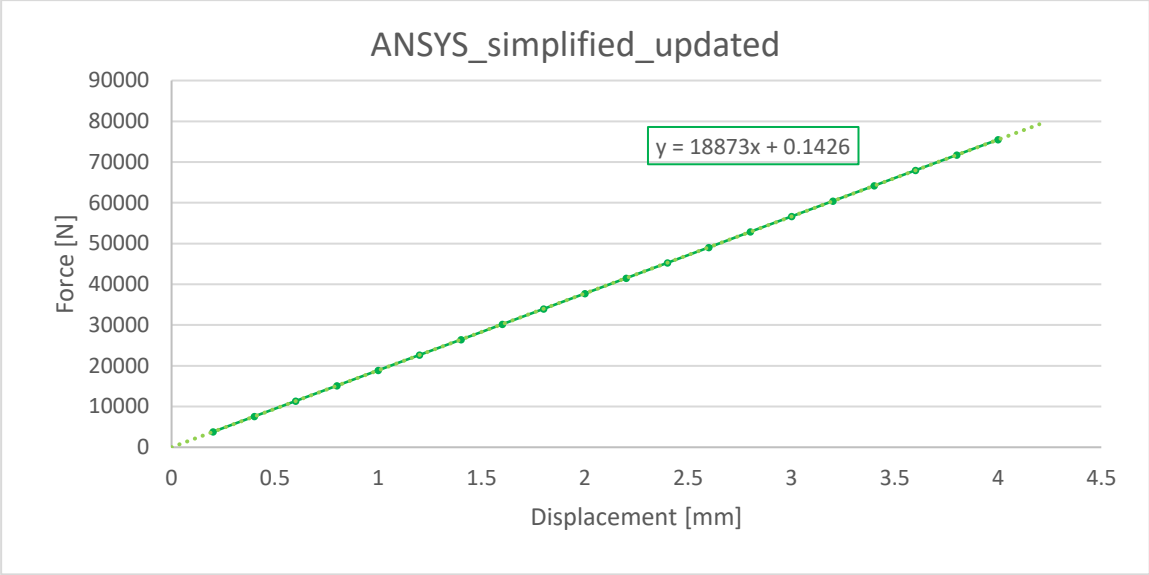

Figure C 1: linear interpolation of updated simplified PEEK insulator model that makes use of equivalent PEEK material.

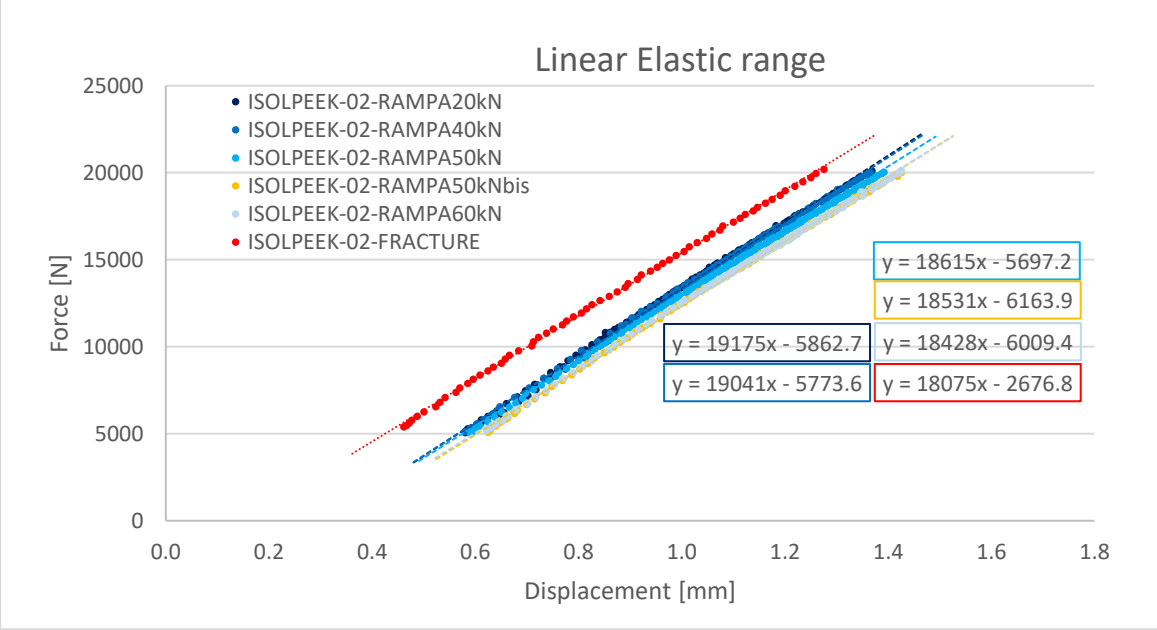

Figure C 2:linear interpolation of ramps up to 60 kN of PEEK insulator sample n°2.

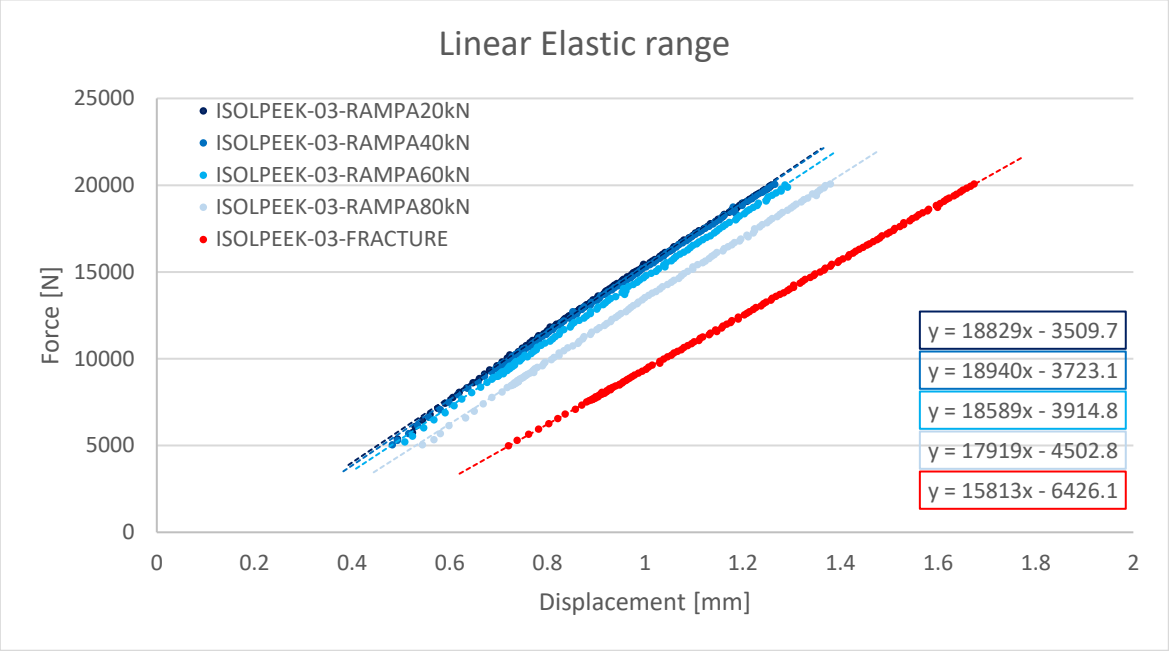

Figure C 3: linear interpolation of ramps up to 80 kN of PEEK insulator sample n°3.

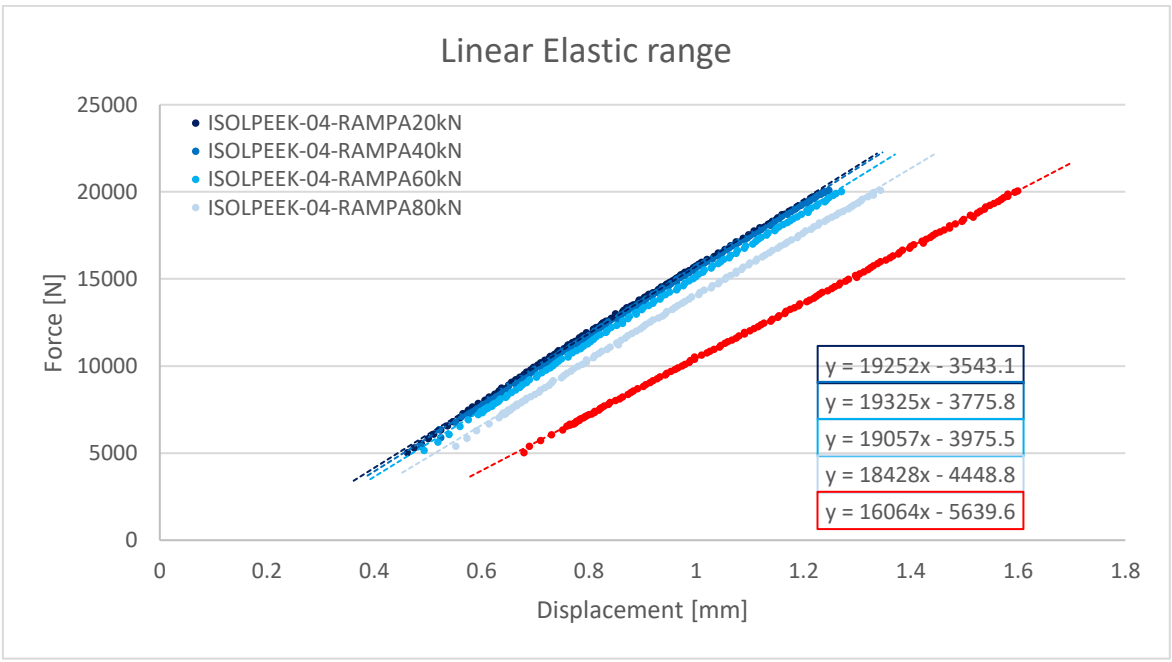

Figure C 4: linear interpolation of ramps up to 80 kN of PEEK insulator sample n°4.

18. Appendix D

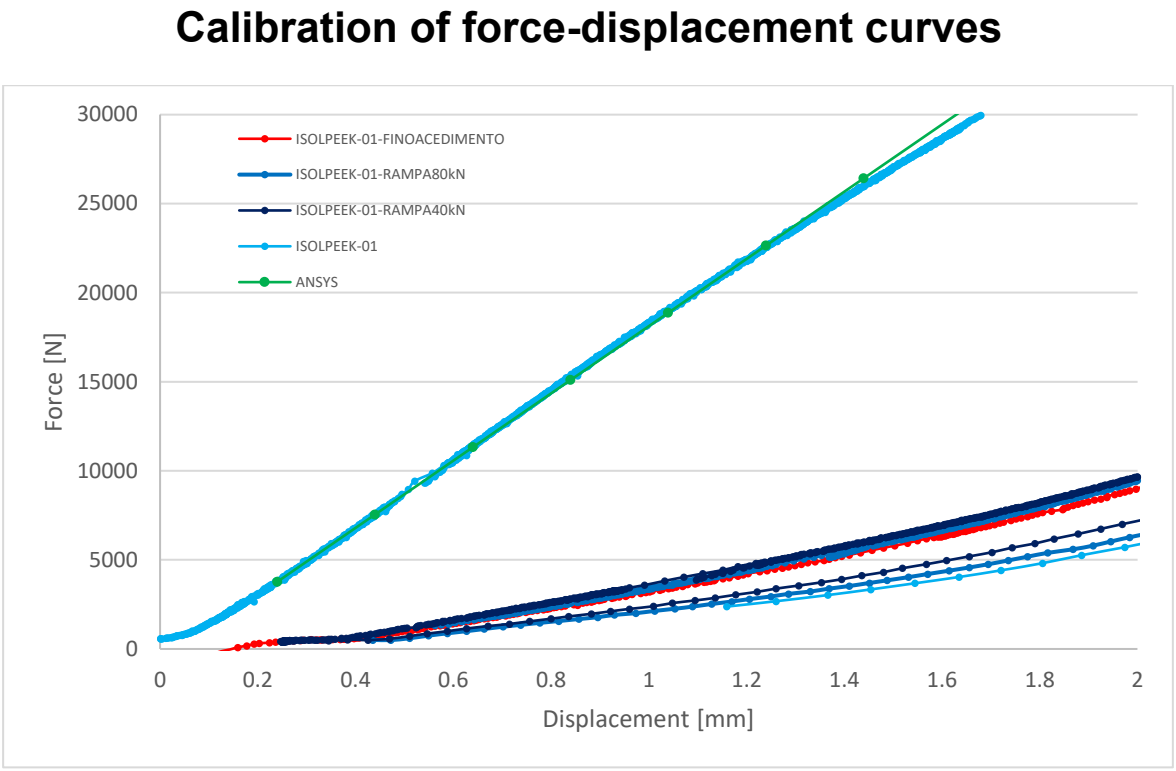

Figure D 1: first PEEK sample calibration of force-displacement curve with final offset of 0.04 mm.

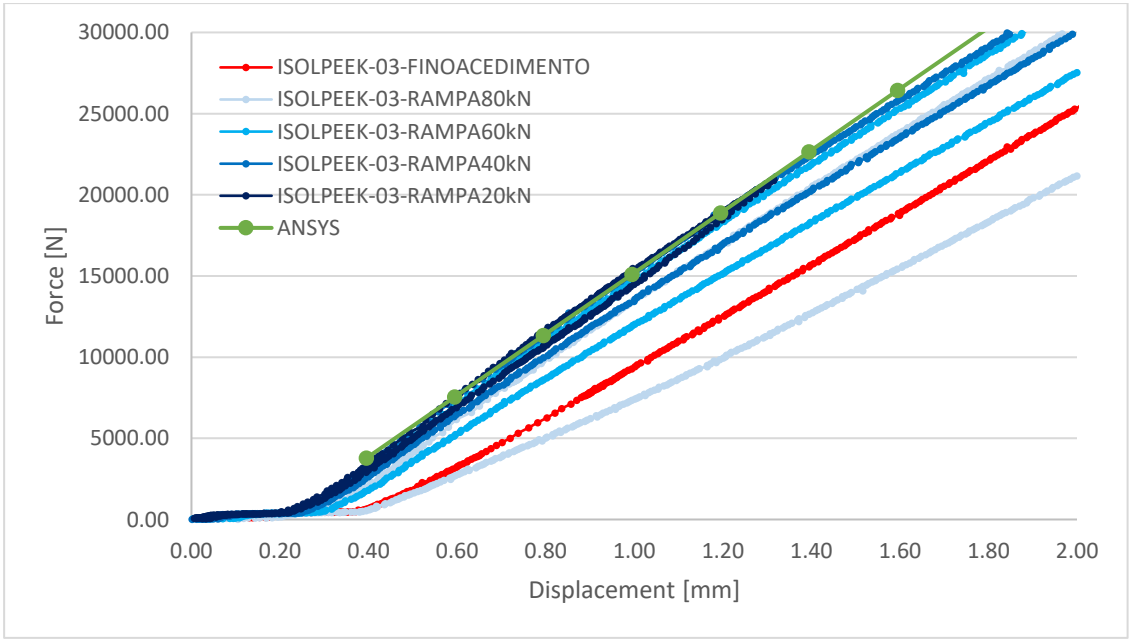

Figure D 2: third PEEK sample calibration of force-displacement curve with final offset of 0.195 mm.

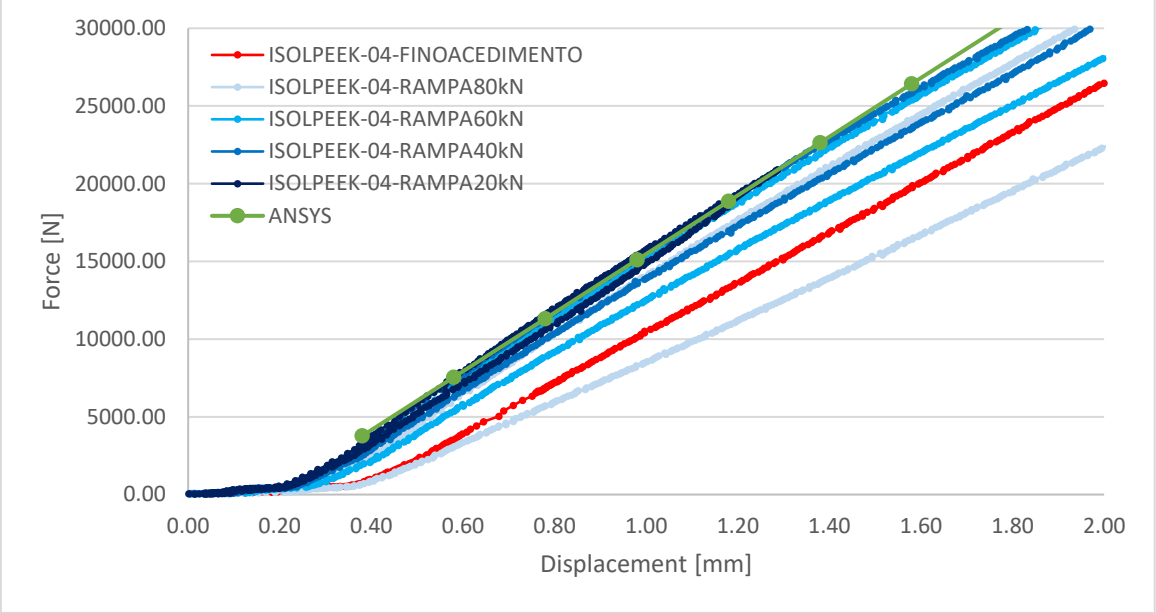

Figure D 3: fourth PEEK sample calibration of force-displacement curve with final offset of 0.18 mm.

19. Appendix E

Example of load limit evaluation of PEEK insulator n°2 for 40 kN ramp

The load limit is chosen as soon as 2 consecutive values of % relative error are greater than 2% at forces higher than 15 kN. In the case of the 20 kN ramp of the second PEEK sample, the value is of 25554 N, highlighted in yellow at time 32.36 s.

This procedure is to be repeated for all PEEK samples.

interpolation equation:		y = 18873x + c
ε %	2	
offset "c"	0.3	

Color:

ISOLPEEK-02-RAMPA40kN

Time Sec	Displacement mm	Force N	Calc. Force N	absolute err. N	relative err. %
3.06	-0.25	-6448.04	-10323	3875	37.5
3.16	-0.25	-6422.18	-10372	3950	38.1
3.26	-0.25	-6413.56	-10323	3910	37.9
3.36	-0.25	-6379.09	-10372	3993	38.5
3.46	-0.24	-6301.52	-10226	3924	38.4
3.56	-0.24	-6189.47	-10128	3939	38.9
3.66	-0.23	-6051.56	-10079	4028	40.0
3.76	-0.22	-5861.94	-9835	3973	40.4
3.86	-0.22	-5646.47	-9738	4091	42.0
3.96	-0.21	-5430.99	-9543	4112	43.1
4.06	-0.19	-5215.51	-9299	4083	43.9
4.16	-0.18	-4982.80	-9103	4121	45.3
4.26	-0.17	-4758.70	-8908	4150	46.6
4.36	-0.17	-4534.60	-8811	4276	48.5
4.46	-0.15	-4319.13	-8567	4248	49.6
4.56	-0.15	-4112.27	-8420	4308	51.2
4.66	-0.13	-3905.41	-8128	4222	51.9
4.76	-0.12	-3698.55	-7884	4185	53.1
4.86	-0.12	-3508.93	-7884	4375	55.5
4.96	-0.11	-3310.69	-7688	4378	56.9
5.06	-0.10	-3103.84	-7493	4389	58.6

5.16	-0.09	-2940.07	-7347	4407	60.0
5.26	-0.08	-2750.45	-7152	4401	61.5
5.36	-0.07	-2586.69	-6957	4370	62.8
5.46	-0.07	-2414.31	-6908	4493	65.0
5.56	-0.06	-2267.78	-6713	4445	66.2
5.66	-0.05	-2129.88	-6517	4387	67.3
5.76	-0.04	-1966.12	-6371	4405	69.1
5.86	-0.03	-1810.97	-6176	4365	70.7
5.96	-0.02	-1673.07	-6127	4454	72.7
6.06	-0.01	-1500.69	-5883	4382	74.5
6.16	-0.01	-1371.40	-5785	4414	76.3
6.26	0.00	-1224.88	-5639	4414	78.3
6.36	0.01	-1112.83	-5444	4331	79.6
6.46	0.01	-1000.78	-5395	4394	81.5
6.56	0.03	-897.35	-5151	4254	82.6
6.66	0.03	-802.54	-5054	4251	84.1
6.76	0.04	-690.49	-4907	4217	85.9
6.86	0.05	-595.68	-4761	4165	87.5
6.96	0.06	-509.49	-4614	4105	89.0
7.06	0.06	-440.54	-4517	4076	90.2
7.16	0.06	-345.73	-4517	4171	92.3
7.26	0.07	-285.40	-4273	3987	93.3
7.36	0.08	-225.06	-4126	3901	94.5
7.46	0.09	-147.49	-3980	3833	96.3
7.56	0.10	-78.54	-3834	3755	98.0
7.66	0.10	16.27	-3687	3704	100.4
7.76	0.10	93.84	-3736	3830	102.5
7.86	0.11	154.18	-3492	3646	104.4
7.96	0.13	240.37	-3297	3537	107.3
8.06	0.13	326.56	-3248	3575	110.1
8.16	0.14	361.04	-3102	3463	111.6
8.26	0.14	378.27	-3004	3382	112.6
8.36	0.15	369.66	-2858	3227	112.9
8.46	0.16	378.27	-2711	3090	114.0
8.56	0.16	395.51	-2565	2961	115.4
8.66	0.17	395.51	-2419	2814	116.4
8.76	0.18	421.37	-2321	2742	118.2
8.86	0.18	395.51	-2223	2619	117.8
8.96	0.19	404.13	-2028	2432	119.9
9.06	0.20	412.75	-1833	2246	122.5
9.16	0.21	404.13	-1736	2140	123.3
9.26	0.21	412.75	-1687	2099	124.5
9.36	0.22	429.99	-1540	1970	127.9
9.46	0.23	429.99	-1394	1824	130.8

9.56	0.24	429.99	-1199	1629	135.9
9.66	0.24	429.99	-1150	1580	137.4
9.76	0.25	438.61	-1004	1442	143.7
9.86	0.25	447.23	-857	1304	152.2
9.96	0.26	455.85	-760	1216	160.0
10.06	0.27	455.85	-613	1069	174.3
10.16	0.27	464.47	-516	980	190.1
10.26	0.28	490.32	-418	908	217.3
10.36	0.28	498.94	-321	819	255.7
10.46	0.29	507.56	-223	730	327.7
10.56	0.30	542.04	-28	570	2053.8
10.66	0.31	585.13	119	466	393.2
10.76	0.31	628.23	265	363	137.0
10.86	0.32	645.47	314	332	105.7
10.96	0.32	679.94	363	317	87.5
11.06	0.33	757.51	509	249	48.8
11.16	0.33	843.71	655	188	28.7
11.26	0.34	938.52	802	137	17.1
11.36	0.35	1033.33	899	134	14.9
11.46	0.36	1136.75	1046	91	8.7
11.56	0.36	1231.56	1192	39	3.3
11.66	0.37	1334.99	1241	94	7.6
11.76	0.37	1412.56	1387	25	1.8
11.86	0.38	1490.14	1485	5	0.4
11.96	0.38	1541.85	1534	8	0.5
12.06	0.39	1628.04	1631	3	0.2
12.16	0.39	1705.61	1778	72	4.1
12.26	0.40	1791.80	1973	181	9.2
12.36	0.41	1869.38	2022	152	7.5
12.46	0.41	1938.33	2070	132	6.4
12.56	0.42	2024.52	2266	241	10.6
12.66	0.42	2110.71	2266	155	6.8
12.76	0.43	2179.66	2412	232	9.6
12.86	0.43	2274.47	2510	235	9.4
12.96	0.44	2352.05	2558	206	8.1
13.06	0.44	2412.38	2705	292	10.8
13.16	0.44	2515.81	2705	189	7.0
13.26	0.45	2602.00	2851	249	8.7
13.36	0.46	2670.95	2949	278	9.4
13.46	0.46	2757.14	2997	240	8.0
13.56	0.46	2843.33	3095	252	8.1
13.66	0.47	2912.29	3144	232	7.4
13.76	0.47	2998.48	3241	243	7.5
13.86	0.48	3076.05	3388	312	9.2

13.96	0.48	3145.00	3388	243	7.2
14.06	0.49	3222.57	3534	312	8.8
14.16	0.49	3291.53	3534	243	6.9
14.26	0.49	3360.48	3632	271	7.5
14.36	0.50	3446.67	3681	234	6.4
14.46	0.50	3524.24	3827	303	7.9
14.56	0.50	3575.96	3778	202	5.4
14.66	0.51	3662.15	3925	262	6.7
14.76	0.51	3739.72	3973	234	5.9
14.86	0.52	3817.29	4071	254	6.2
14.96	0.52	3869.00	4217	348	8.3
15.06	0.53	3963.81	4315	351	8.1
15.16	0.52	3998.29	4169	170	4.1
15.26	0.53	4050.00	4266	216	5.1
15.36	0.53	4093.10	4413	319	7.2
15.46	0.53	4110.34	4364	253	5.8
15.56	0.53	4144.81	4364	219	5.0
15.66	0.54	4205.15	4510	305	6.8
15.76	0.54	4274.10	4461	187	4.2
15.86	0.54	4377.53	4608	230	5.0
15.96	0.55	4549.91	4754	204	4.3
16.06	0.56	4730.91	4949	218	4.4
16.16	0.57	4946.39	5096	149	2.9
16.26	0.58	5136.01	5291	155	2.9
16.36	0.59	5342.87	5535	192	3.5
16.46	0.60	5584.20	5730	146	2.5
16.56	0.62	5860.01	6072	212	3.5
16.66	0.63	6178.92	6315	137	2.2
16.76	0.65	6558.16	6559	1	0.0
16.86	0.68	7101.16	7096	5	0.1
16.96	0.70	7652.78	7633	20	0.3
17.06	0.73	8204.40	8170	35	0.4
17.16	0.76	8756.03	8658	98	1.1
17.26	0.78	9281.79	9146	136	1.5
17.36	0.81	9798.93	9536	263	2.8
17.46	0.84	10298.84	10121	177	1.8
17.56	0.86	10772.89	10609	164	1.5
17.66	0.88	11221.09	11000	221	2.0
17.76	0.90	11677.90	11390	288	2.5
17.86	0.92	12039.90	11732	308	2.6
17.96	0.94	12281.23	12073	208	1.7
18.06	0.94	12263.99	12073	191	1.6
18.16	0.93	11979.56	11878	102	0.9
18.26	0.91	11669.28	11585	84	0.7

18.36	0.89	11307.27	11195	112	1.0
18.46	0.88	10988.37	11000	11	0.1
18.56	0.87	10669.46	10756	86	0.8
18.66	0.86	10376.41	10561	184	1.7
18.76	0.84	10109.22	10268	159	1.5
18.86	0.83	9850.65	9975	124	1.2
18.96	0.82	9635.17	9780	145	1.5
19.06	0.81	9471.41	9633	162	1.7
19.16	0.81	9385.22	9633	248	2.6
19.26	0.81	9436.93	9633	197	2.0
19.36	0.82	9557.60	9780	222	2.3
19.46	0.83	9798.93	9975	176	1.8
19.56	0.84	10066.13	10170	104	1.0
19.66	0.85	10333.32	10463	130	1.2
19.76	0.87	10617.75	10707	89	0.8
19.86	0.88	10919.42	11000	80	0.7
19.96	0.89	11203.85	11195	9	0.1
20.06	0.91	11462.42	11439	24	0.2
20.16	0.92	11755.47	11683	73	0.6
20.26	0.93	11996.80	11878	119	1.0
20.36	0.94	12246.76	12073	174	1.4
20.46	0.95	12496.71	12317	180	1.5
20.56	0.97	12703.57	12610	94	0.7
20.66	0.97	12919.05	12659	260	2.1
20.76	0.98	13117.28	12903	215	1.7
20.86	0.99	13341.38	13049	292	2.2
20.96	1.00	13522.38	13293	229	1.7
21.06	1.01	13703.38	13439	264	2.0
21.16	1.03	13884.38	13683	201	1.5
21.26	1.04	14065.38	13879	187	1.3
21.36	1.05	14237.77	14074	164	1.2
21.46	1.05	14401.53	14220	181	1.3
21.56	1.06	14573.91	14367	207	1.4
21.66	1.07	14729.05	14513	216	1.5
21.76	1.08	14901.43	14708	193	1.3
21.86	1.09	15030.72	14854	176	1.2
21.96	1.09	15194.48	15001	194	1.3
22.06	1.11	15358.25	15196	162	1.1
22.16	1.11	15487.53	15294	194	1.3
22.26	1.12	15634.06	15489	145	0.9
22.36	1.13	15771.96	15586	186	1.2
22.46	1.14	15909.87	15782	128	0.8
22.56	1.14	16047.77	15879	169	1.1
22.66	1.15	16177.06	16026	152	0.9

22.76	1.15	16306.35	16123	183	1.1
22.86	1.16	16427.01	16269	158	1.0
22.96	1.17	16564.92	16416	149	0.9
23.06	1.17	16685.59	16513	172	1.0
23.16	1.18	16806.25	16611	195	1.2
23.26	1.19	16926.92	16757	169	1.0
23.36	1.20	17056.21	17001	55	0.3
23.46	1.21	17159.63	17197	37	0.2
23.56	1.21	17280.30	17245	35	0.2
23.66	1.22	17383.73	17294	90	0.5
23.76	1.22	17513.02	17392	121	0.7
23.86	1.23	17625.06	17489	136	0.8
23.96	1.24	17754.35	17685	70	0.4
24.06	1.24	17831.92	17831	1	0.0
24.16	1.24	17952.59	17831	122	0.7
24.26	1.25	18047.40	17977	70	0.4
24.36	1.26	18159.45	18026	133	0.7
24.46	1.26	18245.64	18124	122	0.7
24.56	1.27	18340.45	18319	22	0.1
24.66	1.28	18443.88	18416	27	0.1
24.76	1.28	18530.07	18514	16	0.1
24.86	1.28	18624.88	18514	111	0.6
24.96	1.29	18711.07	18660	51	0.3
25.06	1.30	18805.88	18807	1	0.0
25.16	1.30	18883.45	18856	28	0.1
25.26	1.30	18978.26	18904	74	0.4
25.36	1.30	19055.83	18904	151	0.8
25.46	1.31	19116.17	19100	17	0.1
25.56	1.32	19185.12	19197	12	0.1
25.66	1.32	19271.31	19246	25	0.1
25.76	1.32	19348.88	19344	5	0.0
25.86	1.33	19426.46	19392	34	0.2
25.96	1.33	19504.03	19490	14	0.1
26.06	1.34	19572.98	19587	15	0.1
26.16	1.34	19650.55	19636	14	0.1
26.26	1.34	19728.12	19685	43	0.2
26.36	1.35	19805.70	19783	23	0.1
26.46	1.36	19874.65	19929	54	0.3
26.56	1.36	19952.22	19978	26	0.1
26.66	1.37	20012.55	20124	112	0.6
26.76	1.37	20081.50	20124	43	0.2
26.86	1.37	20141.84	20222	80	0.4
26.96	1.38	20236.65	20368	132	0.6
27.06	1.38	20296.98	20319	22	0.1

27.16	1.38	20365.93	20466	100	0.5
27.26	1.38	20434.89	20466	31	0.2
27.36	1.39	20495.22	20612	117	0.6
27.46	1.39	20572.79	20612	39	0.2
27.56	1.39	20624.51	20661	36	0.2
27.66	1.40	20702.08	20807	105	0.5
27.76	1.41	20762.41	20856	94	0.4
27.86	1.41	20839.98	20954	114	0.5
27.96	1.41	20917.56	20954	36	0.2
28.06	1.42	20986.51	21051	65	0.3
28.16	1.42	21064.08	21149	85	0.4
28.26	1.43	21133.03	21246	113	0.5
28.36	1.43	21184.75	21295	111	0.5
28.46	1.43	21270.94	21393	122	0.6
28.56	1.44	21322.65	21490	168	0.8
28.66	1.44	21408.84	21539	130	0.6
28.76	1.45	21477.80	21637	159	0.7
28.86	1.45	21546.75	21686	139	0.6
28.96	1.45	21632.94	21783	150	0.7
29.06	1.46	21701.89	21881	179	0.8
29.16	1.46	21762.23	21930	167	0.8
29.26	1.47	21831.18	22027	196	0.9
29.36	1.47	21908.75	22125	216	1.0
29.46	1.48	21986.32	22271	285	1.3
29.56	1.47	22063.90	22125	61	0.3
29.66	1.48	22141.47	22320	178	0.8
29.76	1.49	22219.04	22418	199	0.9
29.86	1.50	22339.71	22564	224	1.0
29.96	1.50	22434.52	22662	227	1.0
30.06	1.50	22537.95	22710	172	0.8
30.16	1.51	22649.99	22808	158	0.7
30.26	1.52	22770.66	23003	232	1.0
30.36	1.53	22874.09	23198	324	1.4
30.46	1.53	23011.99	23247	235	1.0
30.56	1.54	23149.90	23442	292	1.2
30.66	1.55	23279.19	23540	261	1.1
30.76	1.56	23417.09	23735	318	1.3
30.86	1.57	23546.38	23930	384	1.6
30.96	1.58	23701.52	24077	375	1.6
31.06	1.58	23856.66	24223	366	1.5
31.16	1.59	23985.95	24369	383	1.6
31.26	1.60	24123.86	24467	343	1.4
31.36	1.61	24253.14	24662	409	1.7
31.46	1.62	24382.43	24906	524	2.1

31.56	1.62	24520.33	24955	435	1.7
31.66	1.63	24658.24	25150	492	2.0
31.76	1.64	24787.53	25248	460	1.8
31.86	1.65	24925.43	25394	469	1.8
31.96	1.65	25046.10	25540	494	1.9
32.06	1.66	25184.00	25736	552	2.1
32.16	1.67	25296.05	25784	488	1.9
32.26	1.67	25425.34	25931	505	1.9
32.36	1.68	25554.63	26126	571	2.2
32.46	1.69	25692.53	26272	580	2.2
32.56	1.70	25813.20	26419	605	2.3
32.66	1.71	25925.25	26565	640	2.4
32.76	1.71	26045.91	26663	617	2.3
32.86	1.72	26149.34	26809	660	2.5
32.96	1.73	26304.48	26955	651	2.4
33.06	1.74	26407.91	27151	743	2.7
33.16	1.74	26545.82	27199	654	2.4
33.26	1.75	26640.63	27346	705	2.6
33.36	1.76	26761.30	27492	731	2.7
33.46	1.77	26890.58	27736	846	3.0
33.56	1.77	27011.25	27785	774	2.8

The data that follows the 33.56 s is not displayed as it would reach force values up to 40 kN without being of any interest for the identification of the upper load limit for elastic range behavior of the second PEEK insulator.

20. Appendix F

Comparison of modal analysis of MITICA Mock-Up

The percentual relative error between the frequencies determined with real and virtual PEEK material used in the MITICA Mock-Up electrodes model isn't higher than 4.74%, evaluated exactly for the main frequency of the structure.

	Virtual PEEK	Real PEEK		
Mode	Frequency [Hz]	Frequency [Hz]	abs. err. [Hz]	rel. Err. [%]
1	4.1078	4.17591	0.06811	1.63
2	6.9463	7.11665	0.17035	2.39
3	9.1994	9.49797	0.29857	3.14
4	9.6296	9.82194	0.19234	1.96
5	12.79	12.794	0.004	0.03
6	12.816	12.83	0.014	0.11
7	14.235	14.7516	0.5166	3.50
8	14.831	15.2405	0.4095	2.69
9	14.849	15.3525	0.5035	3.28
10	16.357	16.719	0.362	2.17
11	17.169	18.0231	0.8541	4.74
12	18.661	18.9137	0.2527	1.34
13	19.034	19.2957	0.2617	1.36
14	21.681	22.1384	0.4574	2.07
15	21.872	22.8761	1.0041	4.39
16	23.07	23.5983	0.5283	2.24
17	24.124	24.1757	0.0517	0.21
18	25.442	25.7723	0.3303	1.28
19	27.328	27.6663	0.3383	1.22
20	27.979	28.3071	0.3281	1.16

Table 26: comparison natural frequencies found for MITICA Mock-Up using real and equivalent PEEK material.

For completeness the comparison between the participation factors, and effective mass over total mass is shown in Table 27.

	z direction			z direction		
	Virtual PEEK			Real PEEK		
Mode	Partic. Factor	Ratio	Effective Mass / Total Mass	Partic. Factor	Ratio	Effective Mass / Total Mass
1	1.32E-03	0.001584	3.45E-07	-1.27E-03	0.001339	3.19E-07
2	0.71568	0.858365	0.101476	0.67318	0.709826	8.98E-02
3	1.90E-02	0.022815	7.17E-05	-2.58E-02	0.027163	1.31E-04
4	-0.77602	0.930745	0.119311	-0.75346	0.794476	0.112473
5	2.63E-02	0.031512	1.37E-04	2.47E-02	0.026017	1.21E-04
6	-2.39E-03	0.002869	1.13E-06	-1.36E-03	0.001437	3.68E-07
7	-7.02E-03	0.008422	9.77E-06	-1.07E-02	0.011299	2.27E-05
8	-0.63073	0.756489	7.88E-02	-0.57213	0.603275	6.49E-02
9	-0.18828	0.225816	7.02E-03	-2.33E-02	0.024565	1.08E-04
10	-0.21397	0.256627	9.07E-03	4.88E-02	0.051497	4.73E-04
11	0.83377	1	0.137727	0.94837	1	0.178192
12	-9.15E-04	0.001097	1.66E-07	3.87E-03	0.004082	2.97E-06
13	-1.22E-03	0.001468	2.97E-07	3.45E-02	0.036393	2.36E-04
14	1.79E-03	0.002141	6.32E-07	-1.14E-02	0.01197	2.55E-05
15	-1.10E-02	0.013203	2.40E-05	1.04E-02	0.010971	2.14E-05
16	-0.31826	0.381716	2.01E-02	-0.35067	0.369761	2.44E-02
17	-3.94E-02	0.04731	3.08E-04	-0.10005	0.105499	1.98E-03
18	-5.52E-03	0.006617	6.03E-06	-6.21E-03	0.006543	7.63E-06
19	-0.1232	0.147766	3.01E-03	-0.16106	0.169832	5.14E-03
20	1.60E-02	0.019244	5.10E-05	-2.40E-02	0.025319	1.14E-04

Table 27: comparison between real and equivalent PEEK participation factor and effective mass over total mass.

21. References

1. Anonymous. Net Zero by 2050 – Analysis. n.d. Available from: https://www.iea.org/reports/net-zero-by-2050 [Last accessed: 10/4/2023].

2. Agency IAE. IAEA World Fusion Outlook 2023. Text. International Atomic Energy Agency; 2023.

3. George M. United Kingdom's Action Plan for Power Sector Decarbonisation. National Renewable Energy Laboratory (NREL), Golden, CO (United States); 2023.

4. Anonymous. Long-Term Strategies Portal | UNFCCC. n.d. Available from: https://unfccc.int/process/the-paris-agreement/long-term-strategies [Last accessed: 10/25/2023].

5. Anonymous. Two Thirds of Citizens around the World Agree Climate Change Is as Serious a Crisis as Coronavirus. 2020. Available from: https://www.ipsos.com/en/two-thirds-citizens-around-world-agree-climate-change-serious-crisis-coronavirus [Last accessed: 10/4/2023].

6. Mensah J. Sustainable development: Meaning, history, principles, pillars, and implications for human action: Literature review. Ricart Casadevall S. ed. Cogent Soc Sci 2019;5(1):1653531; doi: 10.1080/23311886.2019.1653531.

7. Robert KW, Parris TM, Leiserowitz AA. What is Sustainable Development? Goals, Indicators, Values, and Practice. Environ Sci Policy Sustain Dev 2005;47(3):8–21; doi: 10.1080/00139157.2005.10524444.

8. Agency IAE. Fusion Physics. Text. International Atomic Energy Agency; 2012.

9. Anonymous. Electricity Demand. n.d. Available from: https://ourworldindata.org/grapher/electricity-demand [Last accessed: 10/26/2023].

10. Jackson RB, Ahlström A, Hugelius G, et al. Human well-being and per capita energy use. Ecosphere 2022;13(4):e3978; doi: 10.1002/ecs2.3978.

11. Zollino G, Bustreo C. Corso: INQ0091664 - NUCLEAR FISSION AND FUSION PLANTS 2022-2023. 2023. Available from: https://stem.elearning.unipd.it/course/view.php?id=5196 [Last accessed: 10/4/2023].

12. US Department of Commerce N. Global Monitoring Laboratory - Carbon Cycle Greenhouse Gases. 2023. Available from: https://gml.noaa.gov/ccgg/trends/weekly.html [Last accessed: 10/4/2023].

13. Change NGC. Carbon Dioxide Concentration | NASA Global Climate Change. n.d. Available from: https://climate.nasa.gov/vital-signs/carbon-dioxide [Last accessed: 10/26/2023].

14. Anonymous. Supply – Key World Energy Statistics 2021 – Analysis. n.d. Available from: https://www.iea.org/reports/key-world-energy-statistics-2021/supply [Last accessed: 10/26/2023].

15. Agency IAE. Classification of Radioactive Waste. Text. International Atomic Energy Agency; 2009.

16. Demirel Y. Energy and Energy Types. In: Energy: Production, Conversion, Storage, Conservation, and Coupling. (Demirel Y. ed). Green Energy and Technology Springer: London; 2012; pp. 57–60; doi: 10.1007/978-1-4471-2372-9_2.

17. Anonymous. ENDF-Flexible Database Explorer, V.Zerkin, IAEA-NDS, 2005-2008. n.d. Available from: https://www-nds.iaea.org/exfor/e4explorer.htm [Last accessed: 10/26/2023].

18. Nevins WM, Swain R. The thermonuclear fusion rate coefficient for p-11B reactions. Nucl Fusion 2000;40(4):865; doi: 10.1088/0029-5515/40/4/310.

19. Anonymous. Could Nuclear Fusion Energy Power the Future? – With Melanie Windridge. 2023.

20. Bettini P. Corso: INN1027624 - THERMONUCLEAR FUSION - FUSIONE TERMONUCLEARE 2022-2023. 2023. Available from: https://stem.elearning.unipd.it/course/view.php?id=3472 [Last accessed: 10/4/2023].

21. Anonymous. FusDIS. n.d. Available from: https://nucleus.iaea.org/sites/fusionportal [Last accessed: 10/26/2023].

22. Anonymous. Machine. n.d. Available from: http://www.iter.org/mach [Last accessed: 10/4/2023].

23. Anonymous. Building ITER. n.d. Available from: http://www.iter.org/construction/construction [Last accessed: 10/26/2023].

24. Anonymous. Assembling the Machine. n.d. Available from: http://www.iter.org/construction/assembly [Last accessed: 10/26/2023].

25. Anonymous. 29th IAEA Fusion Energy Conference (FEC 2023). Text. IAEA; 2022. Available from: https://www.iaea.org/events/fec2023 [Last accessed: 10/26/2023].

26. Anonymous. Http://Www.Iter.Org/Album/Media/7 - Technical. n.d. Available from: http://www.iter.org/album/media/7 - technical [Last accessed: 10/26/2023].

27. Zohm H. On the Minimum Size of DEMO. Fusion Sci Technol 2010;58(2):613–624; doi: 10.13182/FST10-06.

28. Zohm H. On the size of tokamak fusion power plants. Philos Trans R Soc Math Phys Eng Sci 2019;377(2141):20170437; doi: 10.1098/rsta.2017.0437.

29. Anonymous. External Heating Systems. n.d. Available from: http://www.iter.org/mach/heating [Last accessed: 10/28/2023].

30. Anonymous. A Test Centre for Neutral Beam Injection. n.d. Available from: http://www.iter.org/construction/nbtf [Last accessed: 10/5/2023].

31. Anonymous. MITICA. n.d. Available from: https://www.igi.cnr.it/ricerca/negative-ion-neutral-beam-injection/mitica/ [Last accessed: 10/5/2023].

32. Agostinetti P, Aprile D, Antoni V, et al. Detailed design optimization of the MITICA negative ion accelerator in view of the ITER NBI. Nucl Fusion 2015;56(1):016015; doi: 10.1088/0029-5515/56/1/016015.

33. Chitarin G, Kojima A, Boldrin M, et al. Strategy for Vacuum Insulation Tests of MITICA 1 MV Electrostatic Accelerator. IEEE Trans Plasma Sci 2022;50(9):2755–2762; doi: 10.1109/TPS.2022.3168341.

34. Pilan N, Marcuzzi D, Rizzolo A, et al. Electrical and structural R&D activities on high voltage dc solid insulator in vacuum. Fusion Eng Des 2015;96–97:563–567; doi: 10.1016/j.fusengdes.2015.05.057.

35. Rizzolo A, Visentin M, Trevisan L, et al. Structural Analyses of the MITICA BS Post-Insulators. Twchnical Note. Consorzio RFX, F4E; 2014.

36. Marcuzzi, D, Pilan N, Gambetta LG, et al. R&D Activities on Ceramic Insulators in Collaboration with Friatec. Technical Note. Consorzio RFX; 2015.

37. Zaccaria P, Agostinetti P, Marcuzzi D, et al. Progress in the MITICA beam source design. Rev Sci Instrum 2012;83(2):02B108; doi: 10.1063/1.3670335.

38. Aprile D. Design of a Mockup of MITICA Beam Source for 1MV Holding Test Campaign. to be published.

39. Denizeau S, Aprile D, Berton G, et al. Structural design of an Electrostatic Shield at -600kV for the MITICA beam source. IEEE Trans PLASMA Sci 2023;X(X):6.

40. Aprile D, Berton G, Chitarin G, et al. Design of Electrodes for High Voltage Tests in MITICA. In: 2023 30th International Symposium on Discharges and Electrical Insulation in Vacuum (ISDEIV) 2023; pp. 521–523; doi: 10.23919/ISDEIV55268.2023.10200412.

41. Denizeau S, Berton G, Marcuzzi D, et al. Mechanical Tests on the PEEK Insulators for the MITICA Mockup. Technical Note. Consorzio RFX, ITER Organization; 2023.

42. Denizeau S. MITICA Beam Source Mockup -600kV Electrostatic Shield Design – Structural Analyses Report. Technical Note. Consorzio RFX, ITER Organization; 2022.

43. Graceffa J. System Load Specifications Load Specification for HNB Beam Source. ITER Organization; 2013.

44. Melton GH, Peters EN, Arisman RK. 2 - Engineering Thermoplastics. In: Applied Plastics Engineering Handbook. (Kutz M. ed). Plastics Design Library William Andrew Publishing: Oxford; 2011; pp. 7–21; doi: 10.1016/B978-1-4377-3514-7.10002-9.

45. Anonymous. PEEK 450G Material Properties Chart. n.d. Available from: https://www.victrex.com/en/downloads/datasheets/victrex-peek-450g [Last accessed: 11/25/2023].

46. Lab R. Mechanical Testing. n.d. Available from: https://rihof.org/orthopedic-research-testing/services/mechanical-testing/ [Last accessed: 10/30/2023].

47. Anonymous. MTS. n.d. Available from: https://www.mts.com/en/products/materials/grips/www.mts.com [Last accessed: 10/30/2023].

48. Madenci E, Guven I. The Finite Element Method and Applications in Engineering Using ANSYS®. Springer US: Boston, MA; 2015.; doi: 10.1007/978-1-4899-7550-8.

49. Spolaore BCA. Valutazione della resistenza e rigidezza di riduttore bistadio mediante Solidworks Simulation. Numerical thesis. Università degli Studi di Padova: Padova; 2021.

50. Anonymous. Ansys 18.1 Explicit Dynamics Analysis Guide. 2017. Available from: https://idoc.pub/documents/ansys-explicit-dynamics-analysis-guide-34wm28508ml7 [Last accessed: 10/6/2023].

51. Anonymous. Mode Participation Factor and Effective Mass | Ansys Courses. n.d. Available from: https://courses.ansys.com/index.php/courses/modal-analysis/lessons/mode-participation-factor-and-effective-mass-lesson-4/ [Last accessed: 11/7/2023].

52. Anonymous. Prestressed Modal Analysis. n.d. Available from: https://courses.ansys.com/index.php/courses/modal-analysis-in-ansys-mechanical/lessons/how-to-perform-prestressed-modal-analysis-lesson-2-2/ [Last accessed: 11/7/2023].

53. Anonymous. How to Designate the Contact. n.d. Available from: https://courses.ansys.com/index.php/courses/fundamental-topics-in-contact/lessons/how-to-designate-the-contact-and-target-sides-properly-lesson-1/ [Last accessed: 11/14/2023].

54. Anonymous. ISO - Search. n.d. Available from: https://www.iso.org/search.html [Last accessed: 11/24/2023].

55. Anonymous. McMaster-Carr. n.d. Available from: https://www.mcmaster.com/ [Last accessed: 11/24/2023].